Clean Combustion Flue Gas Polishing Through Catalytic Combustion in an Integrated Heat Exchanger Reactor System

Hongtian Ge

A Dissertation Submitted to the University of Ottawa
in Partial Fulfillment of the Requirements for the Degree of
Doctor of Philosophy in Chemical Engineering

Department of Chemical and Biological Engineering
Faculty of Engineering
University of Ottawa

Abstract

Combustion flue gas from various sources contains contaminants requiring removal prior to pipeline transport for carbon, capture, utilization and storage. Depending on the combustion method, the main contaminants are often residual fuel such as CH_4, partial combustion product CO, and oxidizer such as O_2. Process intensified heat exchange reactors known as integrated heat exchange reactors (IHXR) can be designed to facilitate contaminant removal while recovering the heat of combustion generated during the removal process. This work describes the formulation and use of a 1-dimensional reduced order reactor model in facilitating the IHXR design for oxy-fuel combustion flue gas where the contaminant of concern is O_2.

The heat exchanger sections of the IHXR can be described by a 2-dimensional reduced order heat exchanger model (2-D ROM), accounting for the cross-flow pattern of the proposed design. A micro-channel cross-flow heat exchanger plate was manufactured as part of a bench-scale experimental set-up, the gas and solid phase temperatures of the experimental set-up were collected and used as the basis for a Nusselt number correlation. The 2-D ROM fitted with the Nusselt number correlation was then used to aid in generating a 3-D OpenFOAM model, in which the heat fluxes between the curved flow channels were calculated to confirm the that the conduction shape factor was near (0.8 to 0.9) unity.

The bench-scale heat transfer experiments were also used to validate the transient modelling capabilities of the 2-D ROM, which was then used along with a reduced order reactor model to create process models of several proposed IHXR designs. The process models were then used to investigate the ability of the IHXR to reject inlet temperature

disturbances through Bode diagrams. The results show that the IHXR designs are generally stable, with their stability increasing as the number of flow channels increases.

Another source of combustion flue gases, pressurized chemical looping combustion (PCLC), was used for IHXR design via process simulation. The contaminants of concern are CH_4 and CO, where the IHXR design features the equilibrium reactor from Aspen HYSYS to determine the effluent species concentration, and plug flow reactor for reactor sizing. A sensitivity analysis was performed on the potential scenario where fuel conversion within the PCLC unit was reduced to 97% from 98.5% to simulate variable combustion efficiency.

Sommaire

Les gaz de combustion de diverses sources contiennent des contaminants devant être éliminés avant leur transport par pipeline pour le captage, la valorisation et le stockage du carbone. Selon le mode de combustion, les principaux contaminants sont souvent des combustibles résiduels tels que le CH_4, le CO (produit de combustion partielle) et des comburants tels que l'O_2. Les réacteurs à échange de chaleur intensifiés, appelés réacteurs à échange de chaleur intégré (RICE), peuvent être conçus pour faciliter l'élimination des contaminants tout en récupérant la chaleur de combustion générée pendant le processus d'élimination. Ce travail décrit la formulation et l'utilisation d'un modèle de réacteur d'ordre réduit unidimensionnel pour faciliter la conception d'un RICE pour les gaz de combustion d'oxy-combustion où le contaminant concerné est l'O_2.

Les sections d'échangeur de chaleur du RICE peuvent être décrites par un modèle d'échangeur de chaleur d'ordre réduit bidimensionnel (MOR-2D), prenant en compte l'écoulement perpendiculaire de la conception proposée. Un échangeur de chaleur à plaques et microcanaux à courants croisés a été fabriqué dans le cadre d'un dispositif expérimental de laboratoire. Les températures des phases gazeuse et solide du dispositif ont été collectées et utilisées comme base pour une corrélation du nombre de Nusselt. Le modèle MOR-2D, équipé de la corrélation de nombres de Nusselt, a ensuite été utilisé pour générer un modèle 3D dans OpenFOAM. Les flux de chaleur entre les canaux d'écoulement ont été calculés afin de confirmer que le facteur de forme de conduction était proche de l'unité (0,8 à 0,9).

Les expériences de transfert de chaleur à l'échelle du laboratoire ont également permis de valider les capacités de modélisation transitoire du modèle MOR-2D, qui a ensuite été

utilisé, avec un modèle de réacteur d'ordre réduit, pour créer des modèles de procédé pour plusieurs conceptions de RICE proposées. Ces modèles de procédé ont ensuite permis d'étudier la capacité de RICE à rejeter les perturbations de température d'entrée grâce à des diagrammes de Bode. Les résultats montrent que les conceptions de RICE sont généralement stables, et que cette stabilité augmente avec le nombre de canaux d'écoulement. Une autre source de gaz de combustion, la combustion en boucle chimique sous pression (PCLC), a été utilisée pour la conception de RICE par simulation de procédé. Les contaminants concernés sont le CH_4 et le CO. La conception de RICE intègre le réacteur d'équilibre d'Aspen HYSYS pour déterminer la concentration des espèces d'effluents, et un réacteur à écoulement piston pour le dimensionnement du réacteur. Une analyse de sensibilité a été réalisée sur le scénario potentiel où la conversion du combustible dans l'unité PCLC serait réduite de 98,5 % à 97 % afin de simuler un rendement de combustion variable.

Statement of contributions

I declare that I am the sole author of this document. I have conducted the experiments, performed the data analysis and prepared the resulting manuscripts for publication. The Python scripts, and OpenFOAM simulations within the main body of the text were also written and prepared by me.

My supervisors, Dr. Jan Haelssig and Dr. Arturo Macchi, and collaborators from CanmetENERGY Ottawa, Scott Champagne and Dr. Robin Hughes, provided continual guidance and contributed with editorial comments and corrections.

The 2-D reduced order model presented in Appendix A and used in chapters 2 and 3 was co-developed with Andrew Furlong from Dalhousie University; he is also co-author to those papers. The experiments and process simulations in chapter 5 were co-performed with Matthew Perry, he is the co-author to the paper in that chapter.

Acknowledgements

I would like to thank my supervisors Dr. Arturo Macchi and Dr. Jan Haelssig for giving me continued support and guidance and the opportunity me to work on this project.

I would also like to thank CanmetENERGY and Natural Resources Canada for funding this project and providing me with financial support.

Lastly I would like to thank all of the collaborators that I have had the pleasure to work with over the years.

Contents

List of Figures

List of Tables

1. Introduction

1.1. Flue gas polishing prior to transport in carbon capture, utilization and storage

Carbon dioxide (CO_2) is one of the major anthropogenic greenhouse gases currently contributing to climate change, with carbon capture, utilization and storage being one of the major methods of reducing its release into the atmosphere. [1, 2] High purity carbon dioxide streams can be directly obtained from point emission sources and transported via pipeline for utilization and storage or used directly on-site for functions such as enhanced oil recovery [1]. In the context of pipeline transport, carbon dioxide streams require prior purification on-site of emission sources due to pipeline requirements on contaminant concentrations. [3, 4] Major contaminants such as NOx and SOx can be removed via further oxidation and conversion into nitric and sulfuric acid respectively, and water vapour can be removed through condensation. [5, 6] Contaminants such as unspent hydrocarbon fuel and oxidizer (O_2), carbon monoxide from incomplete combustion are of major concern in this work. Adverse effects of O_2 content in carbon dioxide stream include acceleration of transport/processing equipment corrosion rate in the presence of water, and the presence non-condensables such as CO and CH_4 negatively affects the behaviour of CO_2 during high pressure transport. [3]

The proposed pathway for removing these major contaminants is through catalytic combustion. Post combustion flue gas will first undergo a series of contaminants and water vapour removal, leaving the stream with only unspent hydrocarbon fuel, O_2 and carbon monoxide. The processed flue gas then undergoes catalytic reaction to remove the remaining contaminants.

Pipeline specifications such as the Dynamis project (O_2 < 100 PPM) and Alberta Carbon Trunk Line (ACTL) (CH_4, CO < 1 mol%) will be used as the guideline for O_2, CH_4 and CO content in the polished flue gas, respectively. [3, 4]

1.2. Process intensified heat exchanger reactors

Catalytic reaction is the proposed method for flue gas polishing. Examples of conventional reactor figurations for facilitating catalytic reaction and heat management (Figure 1-1) include catalyst packed in tube bundles, alternating adiabatic packed beds with cold shot fuel injection, and alternating adiabatic packed beds with heat exchanger.

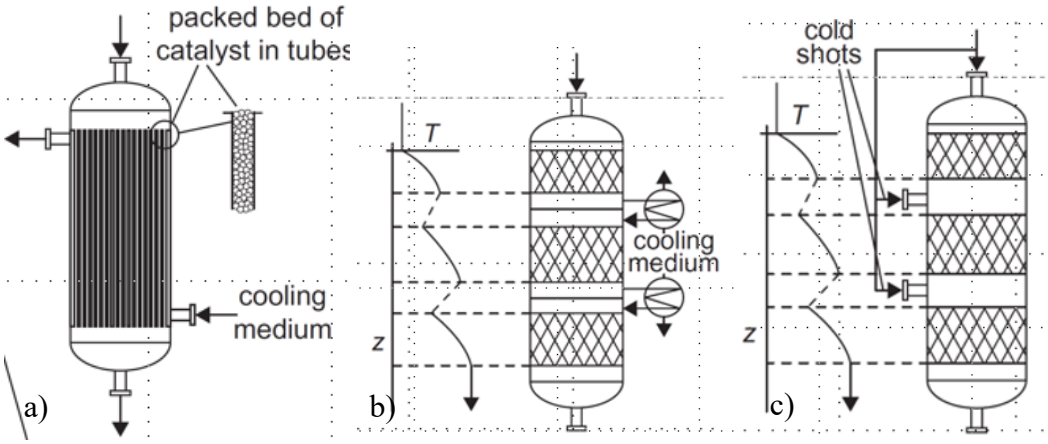

Figure 1-1: a) Packed tubes with cooling jacket, b) multiple adiabatic beds with interstage cooling, c) multiple adiabatic beds with cold shot fuel injection [7]

Convensional reactor configurations such as the packed catalyst bed in tubes demonstrated by the Linde DeOxo reactor at CanmetENERGY is capable of reducing oxygen content to the required levels, however it lacks the precise fuel and coolent temperature and flowrate control required to further improve performance and it is also physically large. [8] Additionally, it is difficult for this configuration to readily react to inlet disturbances as the

inlet fuel and utility fluid conditions are likely controlled via measuing outlet gas conditions, while controlled only at the inlet.

Quasi-isothermal reactors consisted of adiabatic packed bed reactors with insterstage cooling (Figure 1-1b) is a proposed improvement upon the current DeOxo reactor design [9]. However, as fuel enters with the process fluid together at the inlet, this design still lacks fuel control in both flow rate and temperature. Alternating packed beds with cold-shot fuel injection (Figure 1-1c) can offer better fuel control, however temperature control is still limited to only through mixing process fluid with fuel.

Process intensified heat exchanger reactors known as Integrated Heat Exchange Reactors (IHXR) combines both interstage heat exchange and fuel injection to provide improvements to these conventional reactor configurations by offering superior temperature and fuel control simultaneously. An IHXR is the combination of alternating adiabatic packed bed reactors and printed circuit heat exchangers (PCHE). A PCHE is a compact heat exchanger usually consisting of chemically etched micro-channels that is capable of providing large amounts of heat transfer area per unit volume. [10] Designs of IHXRs have been shown capable of facilitating high energy reactions such as steam-methane reforming and Fischer-Tropsch processes, it is possible to similarly extend the concept to catalytic combustion. [11, 12]

The proposed IHXR design features three distinct plate designs, each plate has two distinct sections with one section facilitating heat exchange and fuel control, the other facilitating catalytic reaction. The three plates for one proposed type of IHXR design featuring cross-flow counter-current heat exchange is given in Figure 1-2. The flue gas (process fluid) enters the IHXR via the process plate and is directed into the packed bed reactor section.

The reactor section is only accessible via the process and fuel plates, where fuel flow rate is controlled via the fuel plate to achieve stoichiometric combustion of the remaining contaminants within the process fluid.

Upon reaction, the process fluid leaves the packed bed section to enter a heat exchange section for cross-flow heat exchange with the utility fluid. Utility fluid type and condition depend on the application of the IHXR; boiler feed water as an example can be used for heat recovery applications where saturated steam is the product.

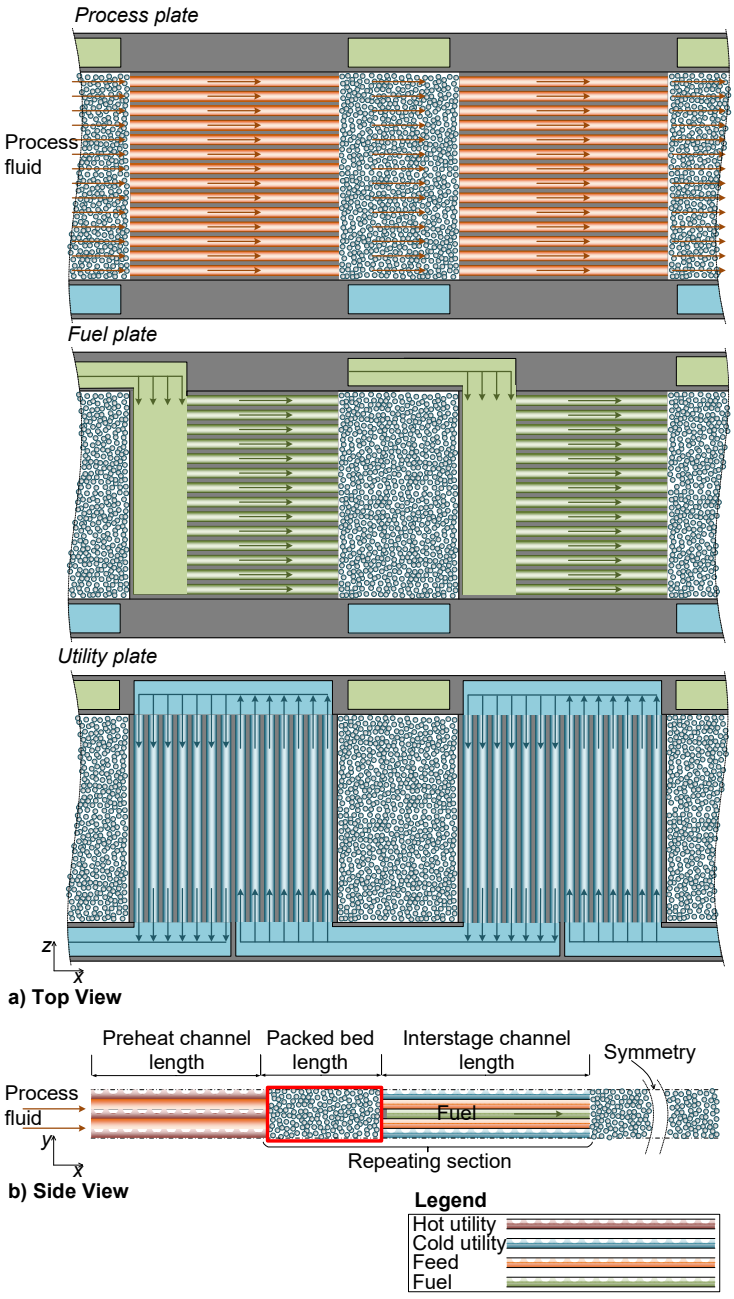

Figure 1-2: a) Top and b) side views of the three distinct plates making up a proposed IHXR design

1.3. Oxy-fuel combustion and pressurized chemical looping combustion for high carbon dioxide content flue gas

Conventional combustion methods using air as oxidizer produces flue gas with a high nitrogen content due to high nitrogen content in air. High nitrogen content is detrimental to CCUS due to large amounts of gas content requiring separation prior to further processing.

However, methods such as oxy-fuel combustion or pressurized chemical looping combustion produces flue gases with much lower nitrogen content due to inherently lower nitrogen content in the oxidizer.

Oxy-fuel combustion uses high purity oxygen (typically > 95 vol%) instead of air as oxidizer, producing a flue gas with vastly reduced nitrogen content [5, 6]. The oxidizer for oxy-fuel combustion is often obtained through cryogenic distillation to reduce the nitrogen content in air. [13]

Pressurized chemical looping combustion (PCLC) uses a metal oxide (MeO) oxygen carrier as the oxidizer to facilitate combustion. The oxygen carrier first reacts with the oxygen in the air reactor to produce heat, the product of the air reactor is an oxidized oxygen carrier and the remaining nitrogen from the inlet air. The oxygen carrier then goes into the fuel reactor for reduction by reacting with a hydrocarbon fuel, the reduction reaction may be an exothermic or endothermic reaction depending on the redox system. The combined heats of reaction from both oxidation and reduction reactions amounts to that of a “normal” combustion, thus net producing heat. [14]

1.4. Reduced order IHXR modelling

Reduced order modelling (ROM) entails a reduction in computational complexity for numerical modelling. ROMs for PCHEs have seen extensive use for performance characterization and their applications in Brayton cycles, which also features CO_2 as a working fluid. [15, 16, 17, 18, 19] However, the extent of use for ROMs have been largely limited to PCHEs.

1-dimensional ROM (1-D ROM) can be made of the reactor sections, reducing the reactor model to only the direction of fluid flow (axial direction, x-direction in Figure 1-2). Whereas the heat exchanger section requires a 2-dimensional ROM (2-D ROM) due to its cross-flow nature, taking into consideration both directions of fluid flow (x-, z-direction in Figure 1-2). A novel application of ROMs can be derived by combining PCHE ROM with a packed bed reactor ROM to create an IHXR ROM, which can be used for sizing and performance characterization for a given desired reaction, providing insight before detailed design and commissioning.

A 2-dimensional transient ROM (2-D ROM) formulated by Furlong et al. is used as the PCHE ROM. [20] As the geometry of the flow channels are semi-circular, there exists the problem of inconsistent thickness of the heat transfer plate between two fluids. To address this issue, a conduction shape factor can be used when calculating the rate of heat transfer. However due to a general lack of data for conduction shape factors pertaining to the specific shapes of the flow channels, the shape factor was assumed to be unity. Through a combination of experimentation to obtain the heat transfer model for the heat exchanger plate and 3-D modelling through the computational fluid dynamics package OpenFOAM, the validity of this assumption will be verified.

1.5. Bench-scale cross-flow micro-channel heat exchanger plate

Figure 1-3 shows the heat exchanger plate manufactured for experiments and characterization. The top and bottom plates function as enclosures and manifolds where the inlet flow is directed through the hole on the top right and leaves through the bottom left section. Each flow is distributed into five equal flows across the flow channels. Five

channels in the z-direction are machined in the obverse side of the centre plate so that the two flows are directed in the x- and z-directions, creating a cross-flow pattern.

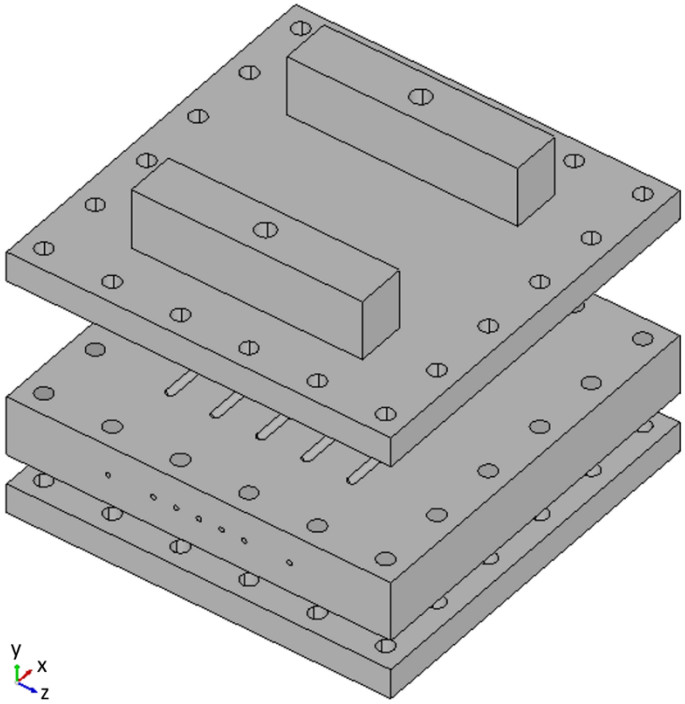

Figure 1-3: Diagram of the manufactured cross-flow micro-channel heat exchanger plate

The design of the manufactured heat exchanger plate slightly differs than that presented in Figure 1-2. The semi-circular parts of the flow channels are in contact for the manufactured plate, whereas the proposed design has the flat part (top) of each flow channel in contact with the semi-circular part of the flow channel that its exchanging heat with. Carbon dioxide is used as the working fluid within this heat exchanger plate. The gas phase temperature is measured through resistance temperature detectors (RTDs) at the inlet and outlet side for both fluids exchanging heat, the solid phase temperature is measured using Fibre Bragg Gratings (FBG) inserted into the holes located in the middle of the plate. [21]

The temperature measuring devices are capable of measuring at frequencies of 5 hz, making it possible for a detailed temperature time-series. The measured temperature data

from experiments can be used to formulate a convective fluid-wall heat transfer correlation. The measured data can also be used to validate simulation results from the 2-D ROM.

1.6. Controllability analysis of IHXR through reduced order modelling

ROMs have seen extensive use in terms of PCHE modelling and performance characterization, however their use does not extend further in literature. It is possible to configure the IHXR ROMs to determine the time constant of individual PCHE and packed bed sections, and subsequently determine the ability of the IHXR as a whole for rejecting inlet disturbances. The 2-D ROM responsible for PCHE modelling can be configured in transient mode to simulate the temperature evolution in both the gas phase and solid phase (heat exchanger bulk temperature) as a function of time, thus to determine the time constant of the system.

The heat transfer coefficient calculated in the form of a Nusselt number in the 2-D ROM is responsible for determining both the solid and gas phase temperatures, it is a geometry dependent equation and thus require careful selection. [22] To ensure the 2-D ROM could correctly predict temperature evolution for a given heat exchanger geometry, a bench-scale cross-flow heat exchanger assembly was manufactured and characterized to determine its heat transfer capabilities, the results were then compiled into a custom Nusselt number correlation. The 2-D ROM can then be equipped with the custom experimentally determined Nusselt number correlation in which the simulated temperature time-series are compared with experimentally measured time-series to confirm the ROM's capability in simulating transient behaviour. Once satisfied with the ROM's transient performance, the Nusselt number correlation can then be changed to a generalized correlation to evaluate for the time constants of proposed PCHE designs. Combining with a reduced order reactor

model, the time constants of proposed IHXR designs can be determined and thus to evaluate the controllability of the proposed designs.

1.7. Practical application of IHXR for flue gas polishing through process simulation

Process simulation can be used to determine the viability of an IHXR design and the relevant reaction kinetics for the desired reaction prior to further design and model development. In situations where the desired reaction kinetics are not readily available, equilibrium reactors can be used as part of a process simulation to determine the practicality of the approach without first performing kinetics characterization.

In the case of PCLC combustion flue gas polishing, where the two major contaminants of interest are CH_4 and CO in an environment of majority CO_2, such conditions are favorable for catalytic reactions such as steam-methane reforming and autothermal reforming to produce hydrogen. [23] As such, the majority of works regarding catalytic reactions with PCLC flue gas species composition are for hydrogen production. The desired reaction pathway in this work is catalytic combustion for CH_4 and CO, where both species are removed via reaction with O_2 to produce heat, CO_2 and water. It is undesirable for any hydrogen gas production in the flue gas polishing process.

Due to this apparent lack of catalytic combustion kinetics regarding catalytic combustion for the species composition in PCLC flue gas, process simulation in Aspen HYSYS through the combination of equilibrium reactor, plug flow reactor, and a set of catalytic combustion kinetics regarding CO combustion in the context of automatic exhaust gas. [24] The major items of interest from process simulation is the gas phase composition of the PCLC flue

gas post polishing, recovery of reaction exotherm and an initial sizing of the packed beds for facilitating catalytic combustion.

1.8. Research objectives

This work sets out to investigate the use of reduced order modelling for designing and characterizing integrated heat exchanger reactors for combustion alternative flue gas polishing in context of pipeline transport prior to CCUS. The main objectives are as listed:

1. Formulation of a 1-D ROM for reactor modelling and its subsequent use for the design and performance characterization of an IHXR for oxy-fuel combustion flue gas polishing.
2. Investigate the impact of shape factor on temperature prediction and heat flux calculation within PCHE reduced order modelling.
3. Determine the controllability of proposed IHXR designs through transient reduced order modelling
4. Design and characterize an IHXR for the purpose of PCLC flue gas polishing

1.9. Overview

This work seeks to model and design an integrated heat exchanger reactor known as an IHXR for removing CH_4, CO, and O_2 from combustion flue gases via reduced order modelling. Criteria for processed flue gas is set based on the allowable contaminant concentration in available pipeline specifications. Two sources of combustion flue gases are used as the basis in this work, one from oxy-fuel combustion with its species concentrations derived from literature, another from PCLC with its species concentrations derived from process modelling based on a currently operating unit. The designed IHXRs are evaluated on their ability to achieve the contaminant concentration requirements set by

pipelines, the amount of heat recovered as part of the flue gas polishing process, and the amount of flue gas treated per unit volume of the IHXR.

Chapter 2 formulates and validates a 1-D ROM for reactor modelling and uses it in the context of oxy-fuel combustion flue gas polishing. The contaminant of interest in this chapter is the residual O_2 and its removal is facilitated through combustion with added CH_4. The heat exchanger section is modelled via a thermal circuit approach to determine the required sizing for combustion heat recovery.

Chapter 3 confirms the assumption of using a conduction shape factor of unity taken in the process of formulating the 2-D ROM for heat exchanger modelling (Appendix A). Heat transfer experiments were conducted on a manufactured micro-channel cross-flow heat exchanger plate, with the resulting heat flux compared against a 3-D model in OpenFOAM to confirm the influence of a conduction shape factor.

Chapter 4 uses the transient modelling capabilities of the 2-D ROM for a controllability study on various IHXR designs. The 2-D ROM's transient capabilities is first validated by comparison against collected temperature time series from the cross-flow heat exchanger plate. Once validated, the 2-D ROM combined with a reduced order reactor model was used to develop process models of different IHXR designs, which are then used to determine the ability of the various designs for rejecting disturbances in the inlet fluid temperature.

Chapter 5 details the process of designing and characterizing an IHXR for PCLC flue gas polishing via process simulation. This approach allows for an initial estimate of the equipment design prior to moving onto more detailed design and modelling work. The

approach also allows for a design estimate without specific reaction kinetics via the use of the equilibrium reactor function in Aspen HYSYS.

Appendix A presents the formulation and verification of the 2-D ROM that was used throughout chapters 2, 3 and 4. The chapter details the equations making up the 2-D ROM as well as the necessary assumptions taken, and presents the model verification through comparison with values presented in literature.

2. Modelling and design of a novel integrated heat exchange reactor for oxy-fuel combustion flue gas deoxygenation[1]

Abstract:

Concentration of residual O_2 in oxy-fuel combustion flue gas needs to be reduced before CO_2 transportation and utilization or storage. Catalytic combustion with natural gas (catalytic deoxygenation) within a integrated heat exchange reactor (IHXR) is chosen to reduce the residual O_2 concentration. The IHXR design features multiple adiabatic packed beds with interstage cooling and fuel injection, allowing precise control of reaction extent and temperature within each reaction stage through manipulation of fuel and utility flow rates. This work describes the design of an IHXR for methane-oxygen catalytic combustion where the catalyst loading is minimized while reducing the O_2 concentration from 3 vol% to 100 ppmv considering a maximum adiabatic temperature rise of 50 °C per stage. Each IHXR design differs by the number of reaction stages and its individual bed lengths. As part of the design process, a one-dimensional transient reduced order reactor model (1-D ROM) was developed and compared to temperature and species concentration axial profiles from 3-D CFD simulations. The final design consists of 5 reaction stages and 4 heat exchanger sections, providing a IHXR length of 1.09 m at a processing rate of 12.3 kg/s flue gas per m^3 IHXR.

2.1. Introduction

Rising climate change and environmental concerns require a reduction in anthropogenic carbon dioxide emissions. One part of the emissions reduction solution is carbon capture utilization and storage (CCUS). Conventional air-fuel combustion flue gases contain 9 to 15 vol% CO_2 with the balance being primarily nitrogen. Separating CO_2 from nitrogen in

1 This chapter has been published in Energies: Ge, H.; Furlong, A.J.; Champagne, S.; Hughes, R.W.; Haelssig, J.B.; Macchi, A. https://doi.org/10.3390/en17061474

flue gas after combustion is an energy intensive process. [25] Oxy-fuel combustion is an attractive alternative as it replaces air with high purity (typically > 95 vol%) oxygen, yielding a flue gas with a dry-basis CO_2 and O_2 content of around 96 and 3 vol%, respectively [5, 6]. The high concentration of CO_2 reduces the steps required to process the CO_2 for transportation and storage. Impurities such as SOx and NOx can be removed through oxidation with the O_2 already present in the flue gas, followed by scrubbing to produce dilute sulfuric and nitric acid respectively [5]. The remaining major impurity is residual O_2, which is limited to very low concentrations (<100 ppmv) in pipelines, sequestration sites, and utilization processes. [3] Oxy-fuel technologies will require an oxygen removal unit in order for the CO_2 product to meet this stringent specification.

Catalytic combustion with natural gas is a promising method to remove residual O_2, which is hereby referred to as catalytic deoxygenation. Commercial catalytic packed bed reactors with integrated cooling typically have coolant flowing through tube bundles embedded in the reactor [26]. Another configuration uses a shell-and-tube heat exchanger where the tubes are packed with catalyst and the coolant flows in the shell. [7] Heat management in both cases can be challenging as a single stream of cooling fluid is used throughout the entire reactor. One method for improving temperature control is to use multiple adiabatic packed beds with distributed fuel injection and interstage cooling [7]. A further improvement in controllability and performance can be had by incorporating the intensified transport rates found in the Marbond^{TM} heat exchanger from Chart Marston and the printed circuit heat exchanger (PCHE) from Heatric [27, 28]. PCHEs have many desirable qualities such as: 1) high operating temperature of up to 980 °C; 2) high pressure capabilities of up to 965 bar; 3) high surface area density at high pressures (1300 m^2/m^3 at 100 bar); 4)

minimum approach temperature as low as 1 °C; 5) high heat exchanger effectiveness of up to 99% [28, 29]. Due to these desirable qualities, PCHEs have been designed for applications such as N_2 and supercritical CO_2 based Brayton cycles, steam generation for small modular reactors, and waste heat recovery from exhaust gas [30, 31, 32, 33]. However, PCHE design as a process intensified reactor unit can be further explored.

The catalytic deoxygenation unit is designed as multiple adiabatic packed bed reactors with interstage printed circuit heat exchange and fuel injection. Similar approaches have been used for steam-methane reforming and Fischer-Tropsch processes [28, 11, 12]. The design utilizes chemically etched plates for the flow of process, fuel, and utility fluids, in between packed bed reactor sections. The entire assembly is diffusion bonded to fuse the plates into an IHXR (see Figure 2-1 [11]).

In the context of using a IHXR for catalytic deoxygenation of oxy-fuel flue gas, interstage cooling can recover high quality heat from the reaction mixture. Variations in flue gas flow can also be better managed where utility fluid flow rate is adjusted to counteract inlet temperature deviations and O_2 composition deviations are countered by adjusting the fuel flow rate. The reactor design can also be adjusted for higher O_2 concentrations by adding extra beds and the reactor can easily be scaled to accommodate higher throughputs.

Rectangular slots in the path of process fluid flow shown in Figure 2-1 represent the space allocated for catalyst packing. Green and blue slots at the top and bottom of the plates are to distribute fuel and utility fluid (connected to the respective headers), respectively. The flue gas, or more generically the process fluid, alternates between reaction in a packed bed reaction stage and cross-flow heat exchange with utility fluid in a heat exchanger section. Fuel is injected directly into the inlet of a packed stage using the fuel distribution plate.

Alternating reactor and heat exchange sections allows the reactor to operate near the maximum applicable temperature of the reaction for fast kinetics and recovery of the highest possible quality heat. A configuration of four plates in the order of process, fuel, process, and utility forms one repeating unit, to be enclosed by another utility fluid plate above the top process fluid plate for the simplest form of a complete PCHE. This plate design allows for freedom in scalability, where the throughput of the PCHE can be increased by stacking more repeating units.

Considering the above, the objective of this work is to design a novel IHXR for catalytic deoxygenation of oxy-fuel combustion flue gas. First, a one-dimensional transient reduced order reactor model (1-D ROM) is developed and compared to three-dimensional computational fluid dynamic simulations to ensure consistency. Afterwards, the 1-D ROM is used to design the reaction stages along with a thermal circuit approach to design the heat exchange sections. The reaction stages and heat exchange sections combine to form the full IHXR design.

The design intent of the reaction stages is to reduce the O_2 content of the flue gas from 3 vol% to $\leq$ 100 ppmv to meet pipeline or other transportation, utilization or storage specifications. The heat of combustion is recovered by super heating saturated steam from 181°C to 231°C and amounts to approximately 275 kJ per kg of treated flue gas. Further heat recovery can be achieved by using the treated flue gas to pre-heat the inlet flue gas in a heat exchange section prior to the first reaction stage (see Figure 1-2b).

2.2. One-dimensional transient reduced order reactor model

Figure 2-1b shows the modelled reaction stage enclosed in red. Symmetry in the y- and z-axis shown in Figure 2-1 allows modelling one single repeating unit with sufficient width

(e.g., two flow channels in the z-axis) to achieve the effect of modelling a complete packed bed.

2.2.1. Governing equations

One-dimensional flow is assumed for the reactor model considering that the inlet gas is evenly distributed into the packed bed by the process flow channels and wall effects are marginal due to a relatively wide packed bed. The chemistry is solved using Cantera (version 2.5.1) [34] where all the gas and solid phase reaction rates as well as enthalpies of reaction are calculated. Only axial heat conduction is included for the packed bed and radiation heat transfer is excluded due to the relatively low reaction temperature (≤ 550 °C) for this IHXR design.

The 1-D ROM is divided into the gas and solid phases for which the species mass and energy conservation equations are solved. The reaction rate calculation in the solid phase can accommodate surface reaction with absorption/desorption steps and a site balance or simplified solid phase reaction kinetics without a site balance. The Ergun equation is used to calculate the gas phase pressure drop across the packed bed assuming incompressible flow due to a maximum design pressure loss of 10%. All governing equations are derived for the net direction of flow (x-axis).

Continuity:

$$\dot{m} = \rho_g u_g A_C \tag{2.1}$$

Momentum conservation:

$$-\frac{dP}{dx} = \left(\frac{150\mu_g}{d_{sv}^2}\frac{(1-\epsilon)^2}{\epsilon^3}u_g + \frac{1.75\rho_g}{d_{sv}}\frac{(1-\epsilon)}{\epsilon^3}u_g^2\right) \tag{2.2}$$

Energy conservation in the gas phase:

$$\frac{\partial(\rho_g H_g)}{\partial t}\epsilon = -\frac{\partial(u_g \rho_g H_g)}{\partial x} + h_g a_c(T_s - T_g) + q_{R,g} \tag{2.3}$$

Energy conservation in the solid phase:

$$\frac{\partial(\rho_s H_s)}{\partial t}(1-\epsilon) = (1-\epsilon)k_s \frac{\partial^2 T_s}{\partial x^2} + h_g a_c(T_g - T_s) + q_{R,s} \tag{2.4}$$

Species mass conservation in the gas phase:

$$\frac{\partial Y_{g,i}}{\partial t} = -\frac{\partial(u_g \rho_g Y_g)}{\epsilon \rho_g \partial x} + D_{eff}\frac{\partial^2(\rho_g Y_{g,i})}{\rho_g \partial x^2} + k_m \frac{a_c}{\epsilon}(Y_{s,i} - Y_{g,i}) + R_{g,i} \tag{2.5}$$

Species mass conservation in the solid phase:

$$\frac{\partial Y_{s,i}}{\partial t} = k_m \frac{a_c}{1-\epsilon}(Y_{g,i} - Y_{s,i}) + R_{s,i} \tag{2.6}$$

The axial dispersion coefficient, D_{eff}, is determined using data provided in Levenspiel et al. [35]. The Gunn analogy [36] for both heat and mass transfer is used to calculate the interphase heat and mass transfer coefficients in Equations 2.7 and 2.8.

$$Nu = (7 - 10\epsilon + 5\epsilon^2) \times \left(1 + 0.7 Re_p^{0.2} Pr^{\frac{1}{3}}\right) + (1.33 - 2.4\epsilon + 1.2\epsilon^2) \times Re_p^{0.7} Pr^{\frac{1}{3}} \tag{2.7}$$

$$Sh = Nu\left(\frac{Sc}{Pr}\right)^{\frac{1}{3}} \tag{2.8}$$

2.2.2. Solution structure

The 1-D ROM was programmed in Python and discretized into *j* equally sized volumes in the axial direction according to Figure 2-1. All governing equations are solved for each discretized volume at each time-step *n*, until the end of the specified solution time span as

per Figure 2-2. The numerical method uses a semi-implicit solution scheme for each time-step, see Equations 2.9 and 2.10 for explicit and semi-implicit time steps.

$$y_{t_{n+1}'} = y_{t_n} + f(y_{t_n}) \times dt \tag{2.9}$$

$$y_{t_{n+1}} = y_{t_n} + \frac{f(y_{t_n}) + f\left(y_{t_{n+1}'}\right)}{2} \times dt \tag{2.10}$$

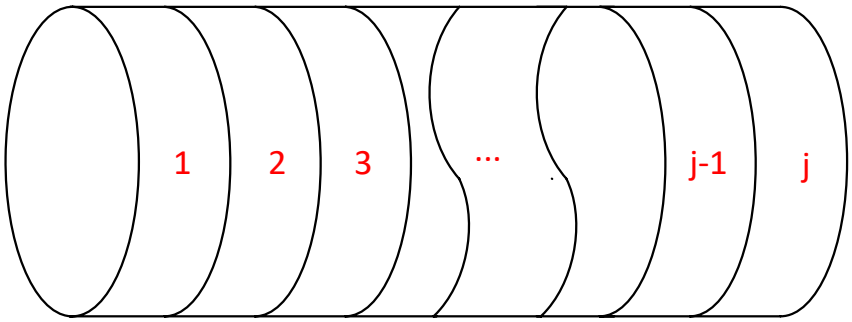

Figure 2-1: Spatial discretization of the 1-D ROM.

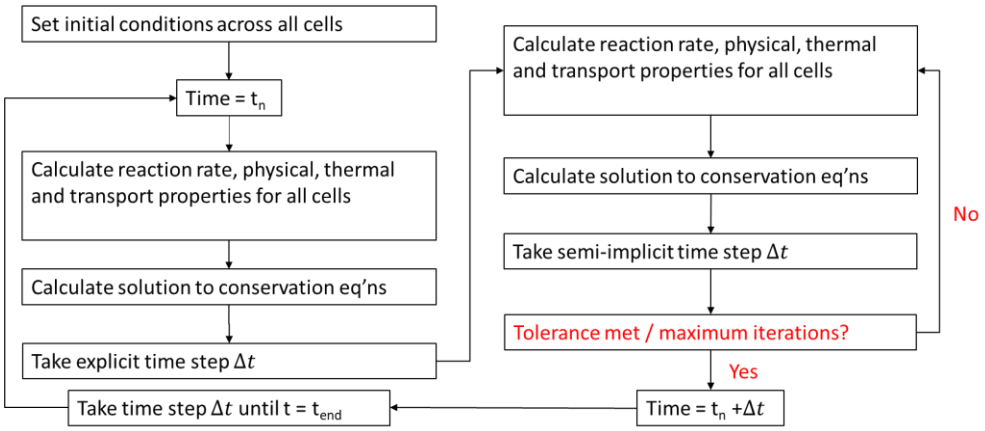

Figure 2-2: Transient solution scheme of the 1-D ROM.

2.2.3. Reaction kinetics

The methane oxidation kinetics on Pd/Co_3O_4 are selected and presented in Table 2-1. The Arrhenius kinetic parameters are applicable from 250 to 550 °C in wet lean environments with a methane concentration of 1000–5000 ppmv and water vapour concentration of 0–5 vol% [37]. Moreover, the reaction kinetics are pseudo first-order with respect to methane and applicable to reaction mixtures with O_2 concentrations as low as 0 vol% over the

temperature range of 400–550 °C due to the oxygen supplying ability of the Co_3O_4 support [38].

Table 2-1: Arrhenius kinetic parameters for methane oxidation on Pd/Co_3O_4 in wet lean environments [37].

Parameter	Pre-exponential factor [L/(g·s)]	Activation energy [J/mol]
Value	46,365	90,738

2.3. Design of the IHXR

2.3.1. Process constraints

The upper operating temperature is 550 °C for the selected reaction kinetic model, and this is also a reasonable temperature limit for stainless steel reactor construction. Furthermore, the temperature rise within a single reaction stage is limited to 50 °C to reduce thermal stress on the material of construction [7], which then results in temperatures between 500 and 550 °C for each reaction stage. The operating pressure is set to a maximum of 1000 kPa to ensure this design could be fabricated using conventional welding techniques, while the total pressure drop is limited to 10% considering compressor duty.

2.3.2. Base case geometry and operating conditions

Process fluid channels and plate dimensions for the IHXR base design are shown in Figure 2-3. The process, utility, and fuel flow channels and plates share the same dimensions, with semi-circular channels 3 mm in diameter, plate thickness of 3.5 mm, and 2 mm separation between the flow channels. Four channels are shown for illustration purposes while the plate can be scaled in the z-direction to accommodate more channels for different total inlet flow rates.

The dimensions of each reaction stage in the y- and z-axis are dictated by dimensions of the heat transfer section as they are interconnected. For a scalable section of the reaction

stage, the resulting height (14 mm) will be in multiples of the combined thickness of the repeating unit formed by four plates. The reaction stage width is in multiples of the width of a single channel and its wall thickness (i.e., 5 mm).

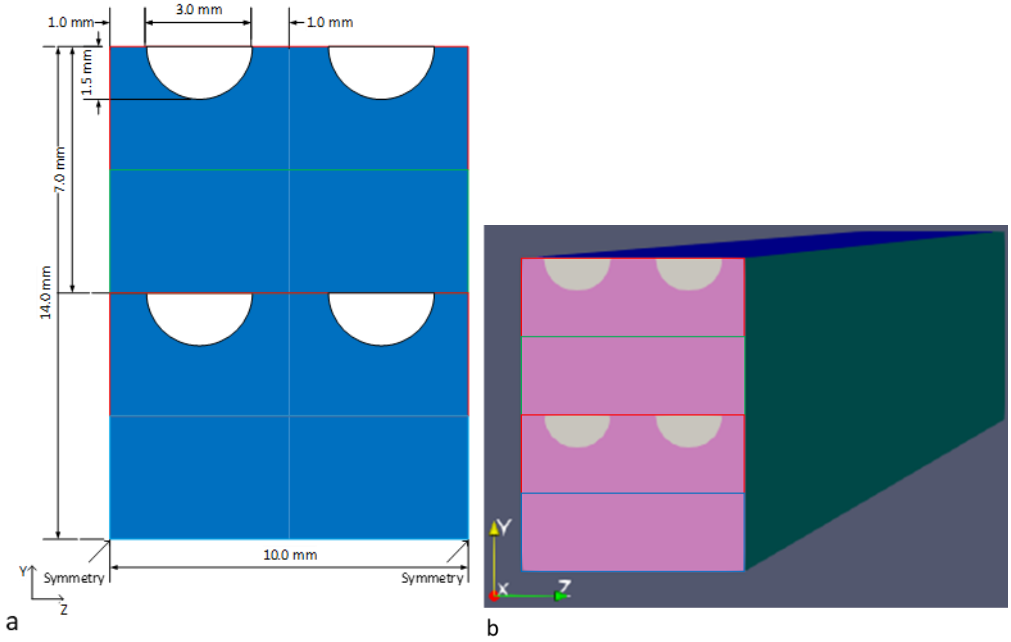

Figure 2-3: Front view of reaction stage modelled geometry consisting of four plates, a) modelled geometry with dimensions, b) 3-D OpenFOAM mesh. The direction of flow is into the page along the x-axis. Process plates are enclosed by red, fuel plate by green and utility plate by blue.

Considering Figure 2-3, the modelled IHXR geometrical parameters and inlet flow conditions (for four channels) are given in Table 2-2. Species concentrations are based on typical oxy-fuel combustion flue gas O_2/CO_2 compositions with other contaminants removed [5]. Stoichiometric amount of fuel to achieve the desired O_2 consumption is used. These operating conditions are selected to achieve a Reynolds number of around 8000 in the process flow channels to generate turbulent flow and enhance post reaction heat recovery.

The reaction stages of the IHXR are divided into two categories: the repeating stages, and the final stage. As the repeating stages have the same dimensions, only the first repeating stage and the last stage are simulated to obtain temperature and species concentration axial profiles. Inlet conditions in Table 2-2 are for the first reaction stage, and subsequent stages inlet conditions are obtained by global mass and energy balances. The bed length of a given repeating stage consumes the methane fuel to below 0.01 wt% while final stage bed length consumes oxygen to below 0.007 wt% (100 ppmv). Note that the modeled stage length of 0.06 m is only chosen to achieve sufficient extent of reaction. The minimum number of reaction stages is five based on the maximum temperature rise of 50 °C per stage; resulting in a per-stage reduction of 22% of the total O_2 for the four repeating stages. As the Peclet number is 48, advection is dominating as compared to diffusion mixing, the system is approaches plug flow.

Table 2-2: Modelled geometry parameters and inlet flow rate for a single reaction stage as per Figure 2-3

	Value	Unit
Height	14	mm
Width	10	mm
Length	60	mm
Particle diameter	2	mm
Catalyst coating thickness	0.4	mm
Catalyst weight	13.3	g
Packed bed porosity	0.45	-
Process fluid inlet flow rate	7.62	kg/h
Fuel inlet flow rate	0.01	kg/h
Process fluid CO_2 mass fraction (1st stage)	0.978	-
Process fluid inlet O_2 mass fraction (1st stage)	0.022	-
Inlet fluid pressure (1st stage)	1000	kPa
Inlet fluid temperature (1st stage)	500	°C
Axial dispersion coefficient	0.005	m^2/s
Peclet number	48	-

Considering Figure 2-3b, the 1-D model uses the entire cross-section of the reaction stage as the inlet for the process fluid, while the 3-D model only uses the semi-circular inlet ports. The 3-D fluid flow field was obtained using OpenFOAM (version 10) [39] with the multiphaseEulerFoam solver, which takes a unity Lewis number assumption. As a result, process and fuel flow into the reaction stage pre-mixed for all OpenFOAM simulations.

The multiphaseEulerFoam simulation uses a max time-step size of 1E-4 s with the adjustTimeStep function turned on, and a maxCo of 2.

The solver and tolerance, algorithm control, and under-relaxation factors dictated by the fvSolution dictionary are as follows (Table 2-3).

Table 2-3: 3-D model simulation parameters listed in the fvSolution dictionary

Attribute	Parameter	Value
Solver and tolerance		
nAlphaCorr	alpha.*	1
nAlphaSubCycles	alpha.*	1
solver	p_rgh/p_rghFinal	GAMG
	U.*/U.*Final	smoothSolver
	(h|e).*/(h|e).*Final	smoothSolver
	(Yi).*	PBiCGStab
smoother	p_rgh/p_rghFinal	DIC
	U.*/U.*Final	symGaussSeidel
	(h|e).*/(h|e).*Final	symGaussSeidel
preconditioner	(Yi).*	DILU
tolerance	p_rgh/p_rghFinal	1e-7
	U.*/U.*Final	1e-7
	(h|e).*/(h|e).*Final	1e-7
	(Yi).*	1e-12
relative tolerance	p_rghFinal	0
	U.*Final	0
	(h|e).*Final	0
	(Yi).*	0

The discretization schemes dictated in the fvSchemes dictionary largely follow default multiphaseEulerFoam settings with the laplacianSchemes and snGradSchemes changed to "Gauss linear corrected" and "corrected", respectively. The OpenFOAM mesh is composed of 295,200 cells, with 400 by 35 by 26 cells in the x-, y-, and z-direction respectively, shared by both the 1-D and 3-D OpenFOAM models. The 1-D ROM mesh is comprised of 120 equal volume cells along the x-direction.

2.3.3. Comparison of 1-D ROM to 3-D simulations using the base geometry design and 5 reaction stages

The results from the 1-D ROM (with D_{eff} = 0) were compared to results from the OpenFOAM simulations reduced to one-dimensional flow (1-D OF) in Figure 2-4a. Temperature and concentration axial profiles are nearly identical with a stage length

difference of 1.7%. The impact of the 3-D flow field is also marginal as shown in Figure 2-4b. Figure 2-5 presents the impact of the dispersion coefficient (D_{eff} = 0 and 0.005 m^2/s) on the axial temperature and concentration profiles in the 1-D ROM. The impact is significant where the predicted stage lengths increased from 0.0285 m to 0.031 m after including axial dispersion. Conversely, the gas phase outlet temperatures decreased from 552 °C to 550 °C with the inclusion of dispersion effects. There were no appreciable differences between gas and solid phase temperatures at steady-state, thus only gas phase temperatures are presented.

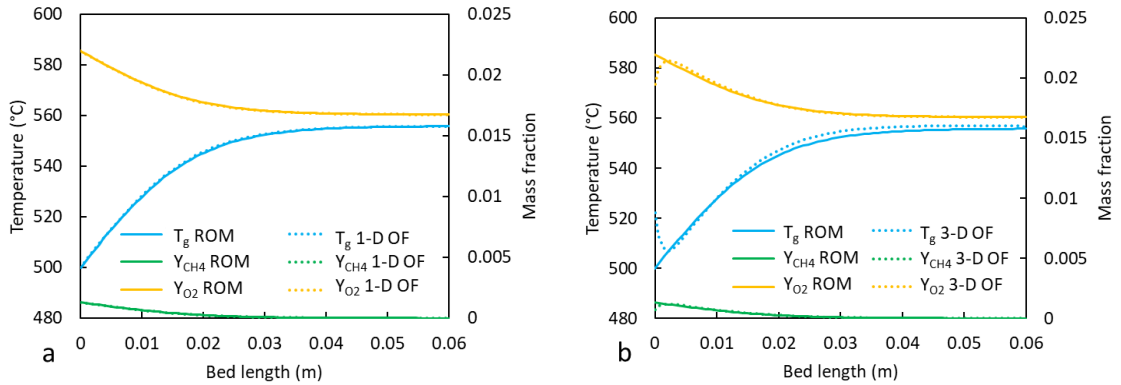

Figure 2-4: Steady-state temperature and species mass fraction profiles for a single reaction stage in five-stage design: a) 1-D ROM without dispersion vs 1-D OpenFOAM (OF), and b) 1-D ROM without dispersion vs 3-D OF.

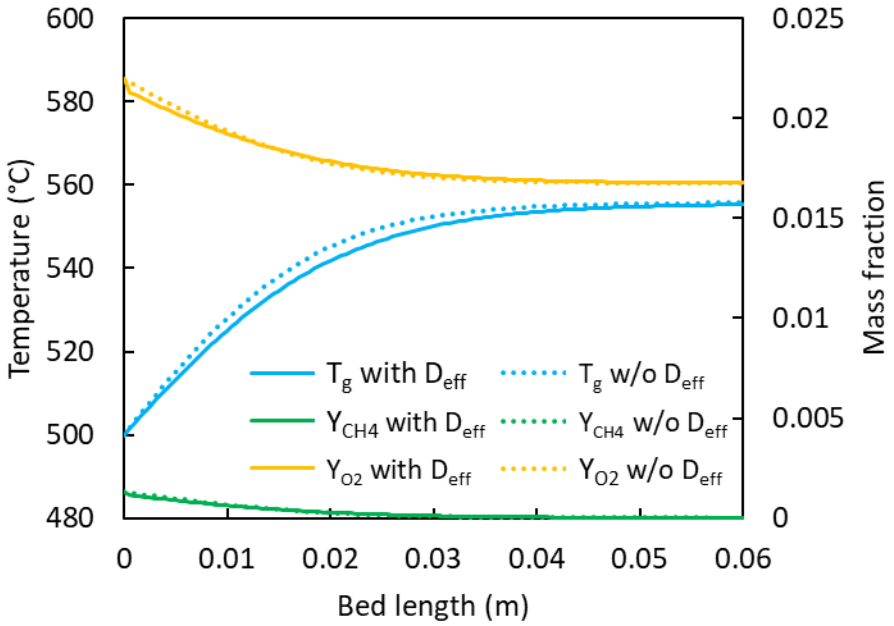

Figure 2-5: Steady-state temperature and species mass fraction profiles for a single reaction stage in five-stage design with D_{eff} = 0.005 m^2/s and without axial dispersion.

2.3.4. Impact of the number of reaction stages on IHXR design

Given that the upper operating temperature is fixed, a lower adiabatic temperature rise (i.e., higher inlet temperature) will lead to a greater intrinsic rate constant. This is achieved by increasing the number of reaction stages and then adjusting the fuel flow rate and the bed length to reach target interstage CH_4 and final stage O_2 outlet concentrations. The repeating bed lengths for IHXR designs with 5 to 11 reaction stages are reported in Table 2-4. Process fluid inlet conditions and model geometry are in Table 2-2. Similarly, the final stage bed length for each case is reported in Table 2-5. Cooling capacity in the heat exchanger section before the final stage is reduced to maintain the highest allowed inlet temperature. The total pressure drops from the reaction stages vary from 30.5 to 35.2 kPa for respectively the 5 to 11 reaction stage designs.

Table 2-4: Simulation results of individual "repeating" stages for IHXR designs with 5 to 11 reaction stages.

Number of reaction stages	Fuel flow rate per stage [kg/h]	Inlet temperature [°C]	Average Temperature [°C]	Stage length [m]	$-\Delta P$ per stage [kPa]
5	0.01	500	532	0.031	6.2
6	0.0081	509	534	0.0275	5.4
7	0.0068	517	537	0.024	4.6
8	0.0058	522	539	0.0215	4.1
9	0.0051	525	539	0.02	3.8
10	0.0046	528	540	0.0185	3.5
11	0.0041	531	542	0.017	3.2

Table 2-5: Simulation results of "final" stage for IHXR designs with 5 to 11 reaction stages.

Number of reaction stages	Fuel flow rate [kg/h]	Inlet temperature [°C]	Average temperature [°C]	Stage length [m]	$-\Delta P$ [kPa]
5	0.00191	540	547	0.0275	5.7
6	0.00153	542	547	0.025	5.1
7	0.00129	543	547	0.023	4.7
8	0.00111	544	547	0.0215	4.4
9	0.00097	545	548	0.02	4.1
10	0.00087	546	548	0.0185	3.8
11	0.00078	546	548	0.017	3.5

Figure 2-6a compares the individual and final stage lengths, while Figure 2-6b compares the combined total length to an ideal isothermal packed bed of the same height and width operated at 550 °C. The final reaction stage to reach a target oxygen concentration of ≤ 100 ppmv does not significantly differ in length from each individual repeating stage and both approach the same length as the number of total stages exceeds 7 for the conditions described.

Although the individual bed length decreases as the number of reaction stage increases, the total bed length increases. This can be attributed to the decreased concentration of CH_4

used to convert a lower amount of oxygen in each stage. As the reaction kinetics are pseudo first-order with respect to CH_4, decreasing its already low concentration reduces the rate of reaction. Although the inlet temperature increases as much as 31 °C as the number of stages increases, the integrated average temperature within the reaction stage rises by only 10 °C. Considering the rate law parameters and process constraints, the optimal multi-packed bed design should thus utilize the least number of reaction stages.

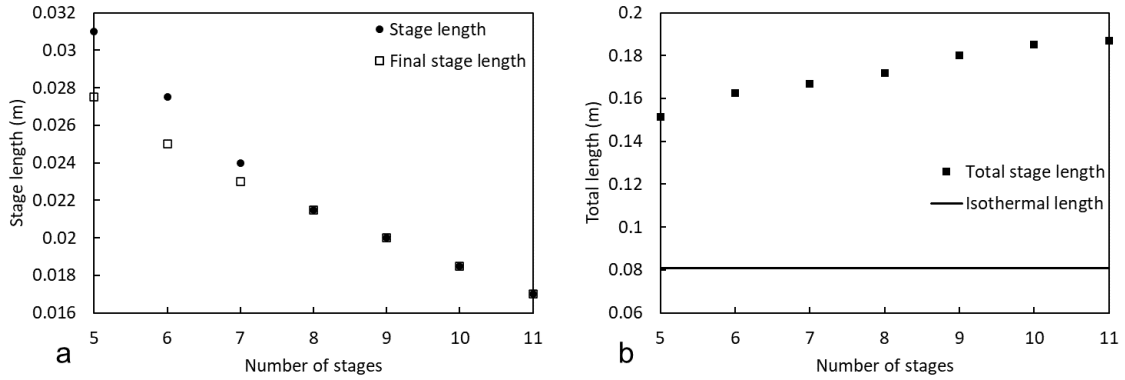

Figure 2-6: a) Length of individual stages and final stage; b) total length of all stages compared to length of the ideal isothermal packed bed.

2.3.5. Heat exchanger design for the multi-stage packed bed designs

The material chosen for the heat exchange section is 316 stainless steel. A 2-pass counter-current cross-flow pattern is selected for the utility plate (see Figure 2-1). Although PCHEs can use other flow channel designs such as zigzag and serpentine to increase heat transfer performance, these patterns generally have higher pressure drop and fabrication costs. Straight channels were ultimately used in this design for its relatively lower frictional pressure drop.

The heat exchange section is modelled using a thermal circuit approach [40], and uses the Gnielinski correlation [41] for a conservative estimate of the convective heat transfer coefficient. Process fluid enters the heat exchange section at Re = 8000, and utility fluid

flow enters at Re = 23,400 – 26,700 depending on the number of reaction stages. Each heat exchange section is modelled as a single complete unit of a IHXR, which consists of 5 plates ordered in the y-axis as utility, process, fuel, process, and utility. Each heat exchange section has a base unit width of 0.3 m, resulting in a utility channel length of 0.3 m and 60 process channels in each section. The utility fluid enters as saturated steam at 10 bar (181 °C) and the superheat rise is again limited to 50 °C to reduce thermal stress on the IHXR plates. The heat exchange sections are separated into repeating sections between reaction stages and a final section before the final reaction stage. The process channel lengths are designed to reach an integer number of utility channels because the number of utility channels governs the resulting length of process channel. Details of the heat exchange section modelling results are given in Table 2-6.

Variation in total length of the heat exchange sections with number of packed beds is minimal as the total energy removed (heat of combustion from deoxygenation) from the gas is the same for all designs. Differences occur due to using an integer number of utility channels (i.e., some designs have more utility channels than required).

Table 2-6: Heat exchange section model results for IHXR designs with 5 to 11 reaction stages.

Number of reaction stages		**5**	**6**	**7**	**8**	**9**	**10**	**11**
Steam flow rate [kg/h]	Repeating section	71.36	55.97	46.22	39.24	33.64	29.47	25.29
	Final section	15.42	9.86	9.78	8.43	5.65	5.65	4.22
Number of utility channels	Repeating section	29	21	17	14	12	11	9
	Final section	6	4	4	3	2	2	2
Length of utility channels [m]					0.3			
Number of process channels					60			
Length of process channels [m]	Repeating section	0.29	0.21	0.17	0.14	0.12	0.11	0.09
	Final section	0.06	0.04	0.04	0.03	0.02	0.02	0.02
Total length of process channels [m]		0.93	0.88	0.89	0.87	0.86	0.9	0.83
Total ΔP from process channels [kPa]		29.6	28.1	28.6	28.1	27.8	29.2	27.0

Considering Table 2-4 to Table 2-6, the IHXR total length and pressure loss are 1.0932 m and 60.1 kPa and 1.0412 m and 62.2 kPa for the 5 and 11 reaction stages designs. The IHXR total length is governed by the heat exchanger sections, whereas the pressure drop through the packed beds are greater than through the heat exchanger sections. The maximum total pressure drop for the IHXR design was 6.4% of the inlet pressure.

2.4. Conclusions

To remove residual oxygen from oxy-fuel combustion flue gases, an integrated heat-exchange reactor for catalytic methane combustion is designed based on a printed circuit heat exchanger embedded with multiple adiabatic packed beds. A transient one-

dimensional flow model of the packed bed reactor was implemented in Python with Cantera as the reaction solver and results were compared to OpenFOAM CFD 3-D modelling. The impact of multi-dimensional effects was marginal on the temperature and concentration axial profiles due to the IHXR geometrical design. However, axial dispersion significantly impacts gas phase mixing and leads to greater bed masses to achieve the required level of deoxygenation.

Design cases for 5 to 11 adiabatic packed bed reaction stages were created using consistent fluid flow and catalyst properties constrained by a maximum adiabatic temperature rise of 50 °C and a 10% pressure loss criteria. Each case was evaluated by determining the repeating reaction stage length to reduce fuel concentration to 0.01 wt% and final stage length for reducing O_2 concentration to 0.007 wt% (100 ppmv). More reaction stages naturally shorten individual stage lengths, but ultimately increase the reactor total bed length due to the impact of reducing methane concentration being greater than the rise in temperature on the reaction rate.

The post-reaction heat exchange sections were designed using a thermal circuit approach, with the results showing similar combined heat exchanger lengths for all cases. The final PCHE design uses five reaction stages at a total length of 1.09 m at a processing rate of 12.3 kg/s flue gas per m^3 IHXR.

3. 2-D reduced order cross-flow heat exchanger modelling using embedded Fiber Bragg Gratings for solid phase temperature acquisition

Abstract

Steady-state gas and solid phase temperatures were measured in a cross-flow heat exchange plate using CO_2 as the working fluid. Fiber optic temperature probes, known as Fiber Bragg Gratings (FBGs), were used to obtain the solid phase temperatures. The measured temperatures were used to develop a convective heat transfer coefficient correlation, which was then used in a two-dimensional reduced-order heat exchanger model to predict gas and solid phases temperatures within 3% and 1.3% of the experimental data. A three-dimensional model was created in OpenFOAM to study the conduction shape factors in the two directions perpendicular to fluid flow. The calculated shape factors are 82.5% and 95.8% of the shape factors without the presence of a flow channel in the through plate and transverse directions, respectively.

3.1. Introduction

Rising concerns for climate change call for a reduction in the emission of anthropogenic greenhouse gases. One avenue of emissions reduction is through the capture and storage of carbon dioxide in emission intensive activities such as fossil fuel combustion for industrial heating. Pressurized chemical looping combustion (PCLC) is an alternative to conventional combustion and offers the advantage of natural gas combustion with intrinsic separation of CO_2 by combusting fuel using an oxygen carrier (e.g., metal oxide) instead of air [42]. The resulting flue gas is primarily composed of carbon dioxide (>90 mol%) with contaminants such as unreacted fuel and carbon monoxide that must be removed before transport and storage [43, 44, 45, 46].

integrated heat-exchanger reactors (IHXRs) can facilitate purification of the flue gas stream through catalytic reaction. IHXRs can be made by combining printed circuit heat exchangers (PCHEs) and mutli-stage catalytic packed bed reactors, and it is a technology previously showcased for highly endothermic processes such as catalytic steam reforming [11, 47]. Similarly, IHXRs can be applied to an exothermic process where contaminants such as unreacted fuel are removed in the catalytic reactors and the reaction exotherm is subsequently removed in the PCHEs for reaction temperature control [48].

The IHXR design process can be divided into the reactor and heat exchanger sections, and the design for each section can be facilitated through reduced order modelling [20, 49]. The internal temperatures of the reactor section can be adequately predicted through a one-dimensional packed bed model. However, the heat exchanger section is more difficult to model due to the range of operating conditions, and the complexity of the geometry and flow pattern [7].

Detailed validation of a heat transfer model requires known solid phase temperatures, which are often difficult to measure due to the challenge of positioning temperature probes inside of a solid piece of heat transfer equipment. Fiber optic temperature probes known as Fiber Bragg Gratings (FBGs) can be positioned at strategic locations in the heat exchanger internals to facilitate temperature monitoring and acquisition [21]. The acquired solid phase temperature profile can then be used to formulate a convective heat transfer model within an overall heat exchanger model.

In this work, a bench-scale cross-flow heat exchanger (CFHE) plate was manufactured and embedded with FBG probes. A set of steady-state heat exchange experiments, using carbon dioxide as the working fluid, were conducted on the bench-scale CFHE to measure and

collect the gas and solid phase temperatures to formulate an empirical convective heat transfer coefficient correlation. The correlation was subsequently used to substitute the Nusselt number correlation in the two-dimensional reduced-order heat exchanger model (ROM) developed by Furlong et. al [20]. The modified 2-D ROM was validated against experimental results and used to produce boundary conditions for the 3-D OpenFOAM model for evaluating the heat conduction shape factors in the two directions perpendicular to the fluid flow.

3.2. Methodology

3.2.1. Experimental setup

The process flow diagram of the experimental system is as shown in Figure 3-1. The gas supply provides CO_2 to both the hot (process fluid) and cold (utility fluid) sides of the CFHE. The CO_2 inlet flow rates are controlled via mass flow controllers (FCV). The flows then go through separate heaters on either side to be brought up to the experimental temperatures. Gas temperatures and pressures of both thermal sides are measured at the inlets and outlets via resistance temperature detectors (RTD) and pressure transducers (PT). The CFHE outlets are with water via heat exchanger before exiting through a vent.

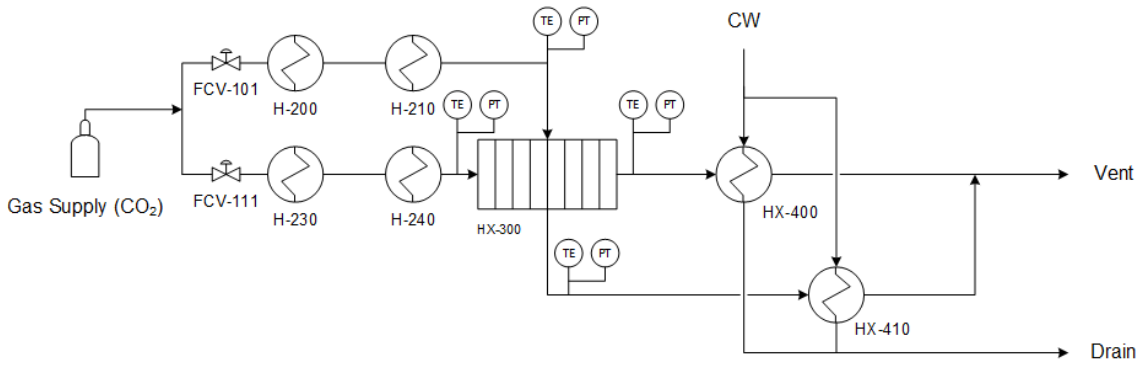

Figure 3-1: Process flow diagram of cross-flow heat exchanger experimental system.

Proline Promass A 100 Coriolis flow meters from Endress+Hauser are used as the mass flow controllers, with a gas mass flow rate accuracy within ±0.35 % of reading [50]. Yokogawa EJA510E absolute pressure transmitters are used as the pressure transducers, with a pressure accuracy of within ±0.055 % of span (0.1 – 2 MPa) [51]. RTDs have an accuracy within ±0.1°C.

The CFHE (HX-300), shown in Figure 3-2, is a 316L stainless steel plate with five semi-circular flow channels of 3 mm in diameter and 75 mm in length (including the rounded ends) machined in cross-flow configuration on opposite sides. Two manifold plates enclose the CFHE on both sides to allow gas flow. Both manifold plates are fastened to the CFHE, and an O-ring is placed around the semi-circular channels on each side for gas sealing. The manifold plates, in their orientation with respect to the CFHE, are shown in Figure 3-3.

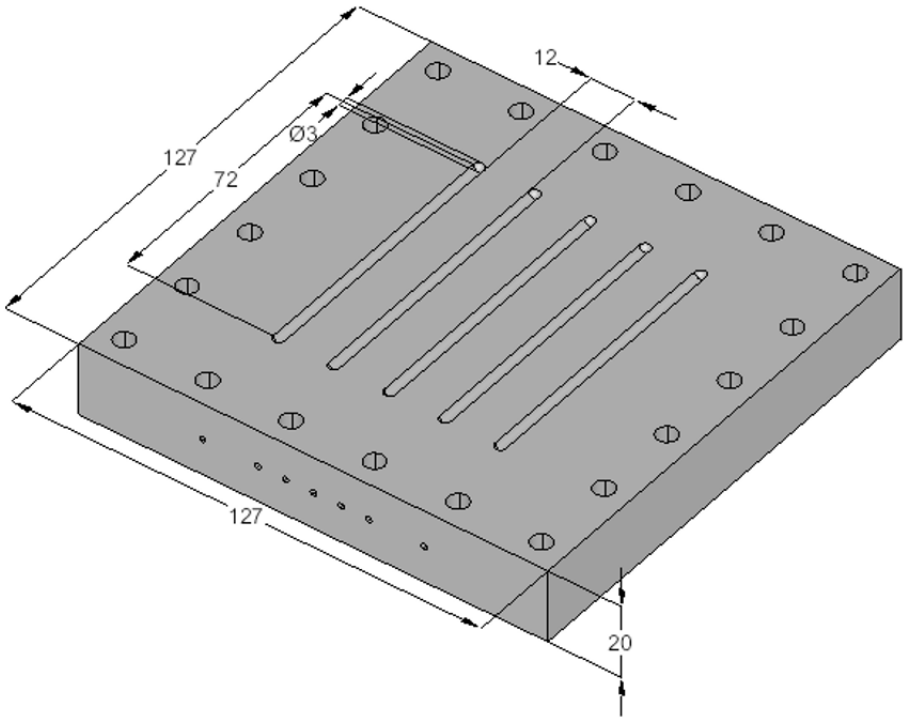

Figure 3-2: Diagram of CHFE with dimensions provided in mm.

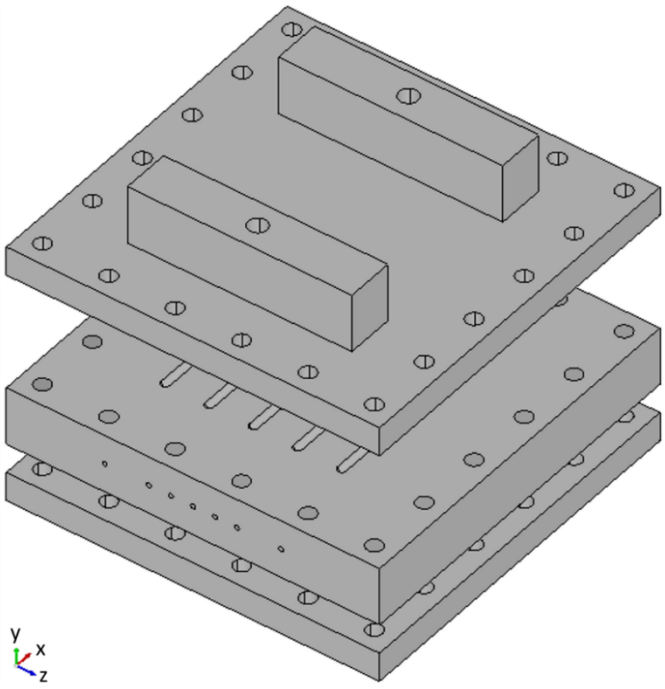

Figure 3-3: Drawing of core CFHE assembly: top, process fluid manifold plate; middle, heat exchanger plate; and bottom, utility fluid manifold plate.

In the orientation shown in Figure 3-3, process (hot) gas flows in the x-direction on the top side of the CFHE, where the gas enters in the lower distributor and exits from the upper distributor. The configuration is rotated 90 degrees for the bottom side, with the utility (cold) gas flow in the z-direction from the right to left, creating a cross-flow pattern.

The seven holes situated in the middle of the CHFE plate shown in Figure 3-2 are placement locations of the fiber optics cables fitted with FBG probes. As shown in Figure 3-4, fifty-seven FBG probes are placed for solid phase temperature measurements. Seven probes are fitted per fiber optic cable on the sides, and the middle cable is fitted with fifteen probes. Twenty-five of the FBGs are directly located at the intersection of two fluid channels.

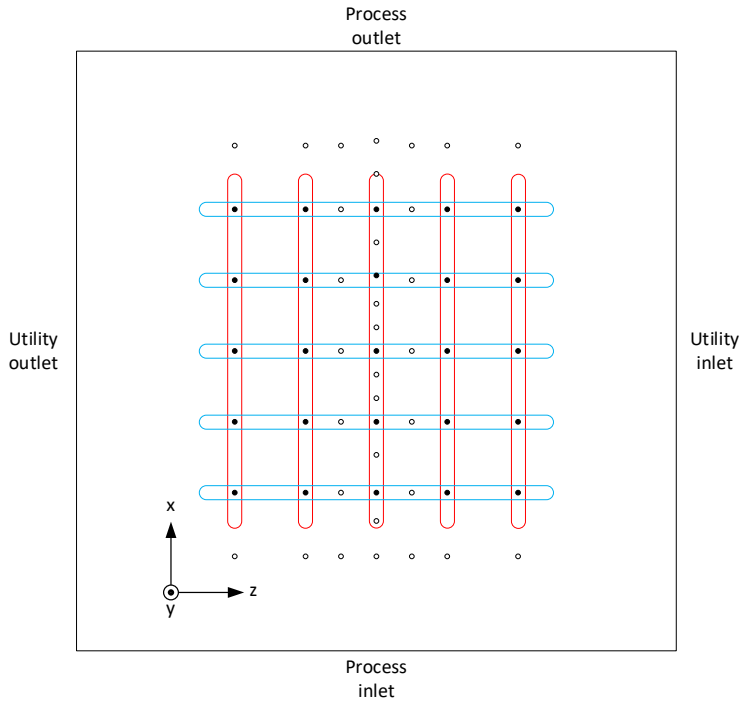

Figure 3-4: Top view of FBG locations within the CFHE plate. Process channels are shown in red and utility channels are shown in blue.

The FBGs function by reflecting a certain wavelength of laser in a fiber optic cable. An interrogator and computer setup collects the wavelength of the reflected laser. Upon experiencing temperature change, the reflected wavelength by the FBG in the fiber optic cable changes from its baseline value due to the thermo-optic effect [21]. The change in wavelength (Eq. 3.1) is converted to temperature via a 6th-order polynomial (Eq. 3.2). The FBGs were calibrated using a programmable oven temperature controlled with an RTD, the measured temperatures are accurate within ±0.1 °C.

$$\Delta\lambda = \frac{|\lambda_{measured} - \lambda_{baseline}|}{\lambda_{baseline}} \tag{3.1}$$

$$T = C_6\Delta\lambda^6 + C_5\Delta\lambda^5 + C_4\Delta\lambda^4 + C_3\Delta\lambda^3 + C_2\Delta\lambda^2 + C_1\Delta\lambda + C_0 \tag{3.2}$$

3.2.2. Experimental design

The experiments used a process fluid temperatures range of 210 – 290 °C at 20 °C intervals and mass flow rates of 5 – 9 kg/h at 1 kg/h intervals. The utility fluid temperature and mass flow rate were fixed at 150 °C and 9 kg/h respectively. The gas inlet pressure for both process and utility fluid was 900 kPa.

The process fluid flow rates were chosen at the upper operating bounds of this equipment to enter turbulent flow. The utility fluid temperature was chosen to ensure it had an adequate difference above room temperature and below process fluid temperature, while its flow rate was fixed at the upper limit of the process fluid flow rate range. The process fluid Re was 5,800–10,000, while the utility fluid Re was fixed to approximately 12,000. The full set of experimental parameters are given in Table 3-1.

Table 3-1: Experimental process fluid inlet conditions with fixed utility fluid inlet conditions of $\dot{m}$ = 9 kg/h, T = 150 °C. Fixed inlet P = 900 kPa for both process and utility fluids.

Trial number	Inlet mass flow rate [kg/h]	Inlet temperature [°C]
1	5	250
2	6	250
3	7	210
4	7	230
5	7	250
6	7	270
7	7	290
8	8	250
9	9	250

3.2.3. Formulating Nusselt number correlation

The collected data, both gas phase and solid phase temperatures, were used to perform a gas phase energy balance (Eq. 3.3) and to calculate an average gas phase convective heat transfer coefficient along the flow channel (Eq. 3.4).

$$q = \dot{m}\bar{c_p}\left(T_{g,out} - T_{g,in}\right) \tag{3.3}$$

$$\bar{h} = \frac{q}{A}\left(\bar{T_g} - \bar{T_s}\right) \tag{3.4}$$

The average heat transfer coefficient was modelled using a correlation in the form of Dittus-Boelter [52], where exponents for Re and Pr remain at 0.8 and 0.4 respectively, and the pre-exponential coefficient was adjusted through least-squares linear regression (Eq. 3.5). The fitted correlation does not differ between hot and cold fluid streams.

$$Nu = \frac{\bar{h}L}{k} = aRe^{b}Pr^{c} \tag{3.5}$$

3.2.4. 2-D ROM modification

An existing 2-D ROM capable of simulating CHFEs has been co-authored and published, the published manuscript is included in Appendix A [20]. However, the Gnielinski correlation currently applied in the 2-D ROM yields Nu that are approxinately 40% of the experimental results from the CFHE, necessitating replacement.

The 2-D ROM models the CFHE using a lumped capacitance approach by calculating heat exchange through means of conduction, convection, and advection between discretized fluid and solid control volumes shown in Figure 3-5

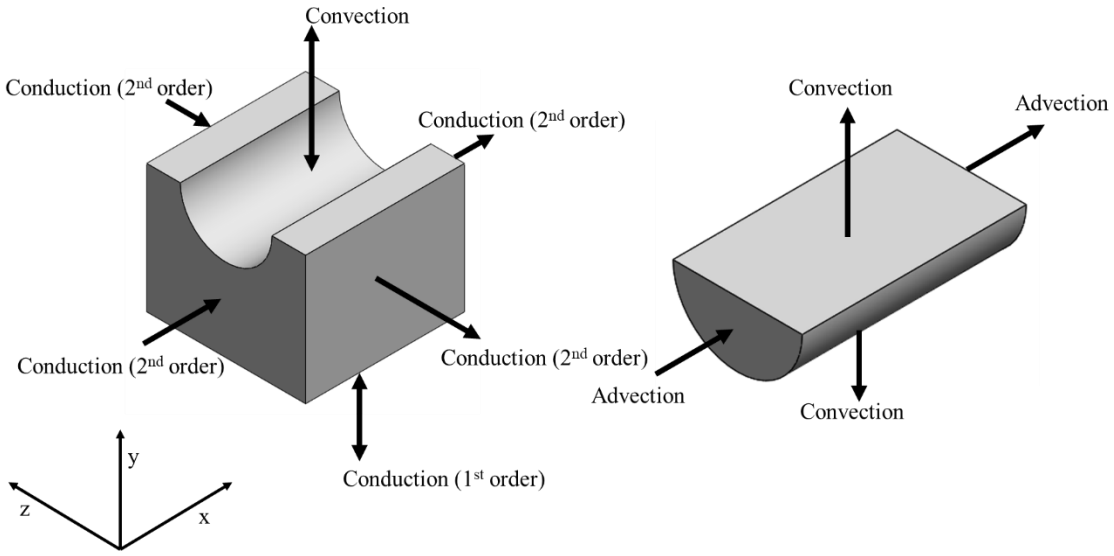

Figure 3-5: Heat transfer terms considered for solid (left) and fluid (right) control volumes. [20]

The discretized volumes are located at each process and utility fluid flow channel intersection, coinciding with the locations of the FBG probes shown in Figure 3-4, where each probe is located between two solid control volumes. A total of 100 control volumes are formed for the 5-channel CFHE, consisting of 50 fluid and 50 solid volumes, of which 25 solid/fluid volumes are used for process fluid flow and 25 for utility fluid flow. The CFHE temperature profile is set as an initial condition and the fluid inlet conditions as boundary conditions.

Furthermore, the 2-D ROM currently uses a conduction shape factor of unity for the intraplate conduction between two discretized solid volumes in the y- and z-directions, assuming a negligible effect from the presence of the flow channel. This assumption will be verified through 3-D modelling via OpenFOAM by calculating for the conduction shape factor in the respective directions.

3.2.5. OpenFOAM mesh construction and simulation setup

The OpenFOAM mesh was constructed using Salome version 9.10.0 [53]. The mesh is almost identical to Figure 3-2 excluding the fastener and FBG placement holes. Figure 3-6 illustrates the OpenFOAM mesh using a simulation of trial #5 at steady-state with the process side facing up. Red indicates the hotter part and blue indicates the cooler part of the temperature gradient.

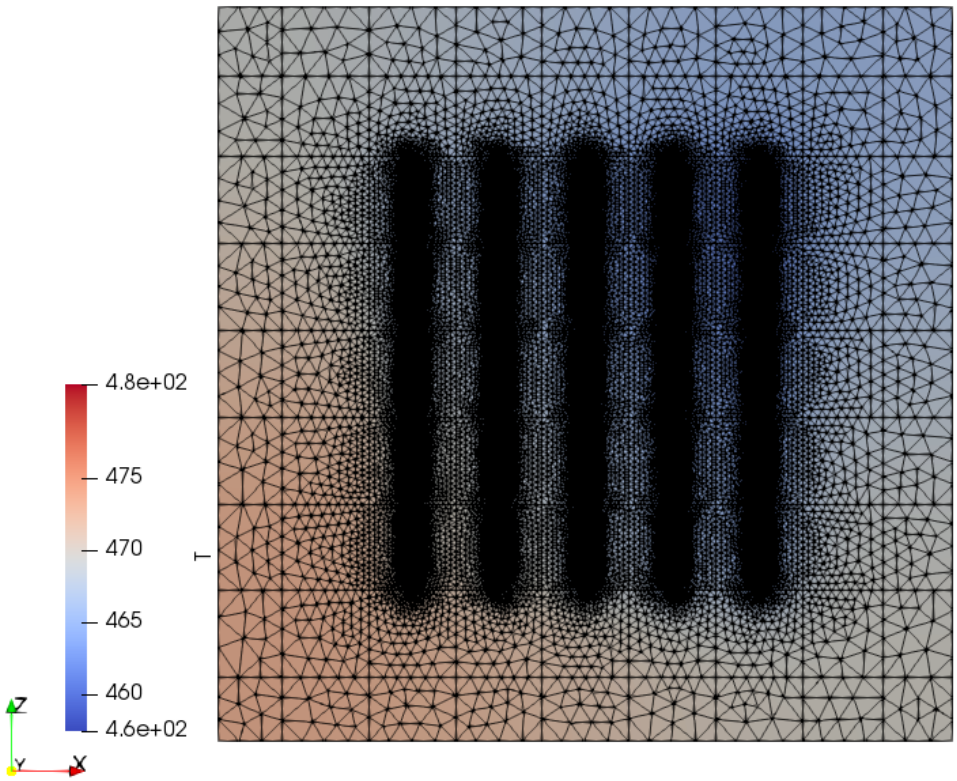

Figure 3-6: OpenFOAM mesh with steady-state temperature profile of trial #5 (temperature units in K).

The mesh consists of three integral sections: the flow channels, the top and bottom surface areas, and the side surface areas. The 3-D simulation is set up by using a fixed uniform temperature boundary condition on the surface of the flow channels to substitute convective heat transfer from the process and utility fluids to reduce modelling complexity,

computational load, and modelling time. The top, bottom, and side surfaces were given adiabatic boundary conditions as they do not participate in heat transfer.

Three meshes were simulated to establish mesh independence. The coarse, medium, and fine meshes contained 124,600, 599,600, and 3,098,900 tetrahedral cells. Mesh independence was established by calculating the percentage errors between temperatures sampled at the FBG locations for each mesh with respect to results from the fine mesh. The results show an average error of 0.012 % and 0.0067 % from the coarse and medium meshes, establishing mesh independence.

OpenFOAM ver. 10 and the chtMultiRegionFOAM solver were used for this simulation. [39] The energy equation was able to converge to a final residual of 9.6e-7 using second order accurate spatial discretization schemes.

3.3. Results and Discussion

3.3.1. Nusselt number correlation fitting and modified 2-D ROM validation

The Nusselt numbers from the collected experimental results are fitted to $Re^{0.8}Pr^{0.4}$ calculated at average fluid properties, and results are shown in Figure 3-7 where the R^2 is 0.998.

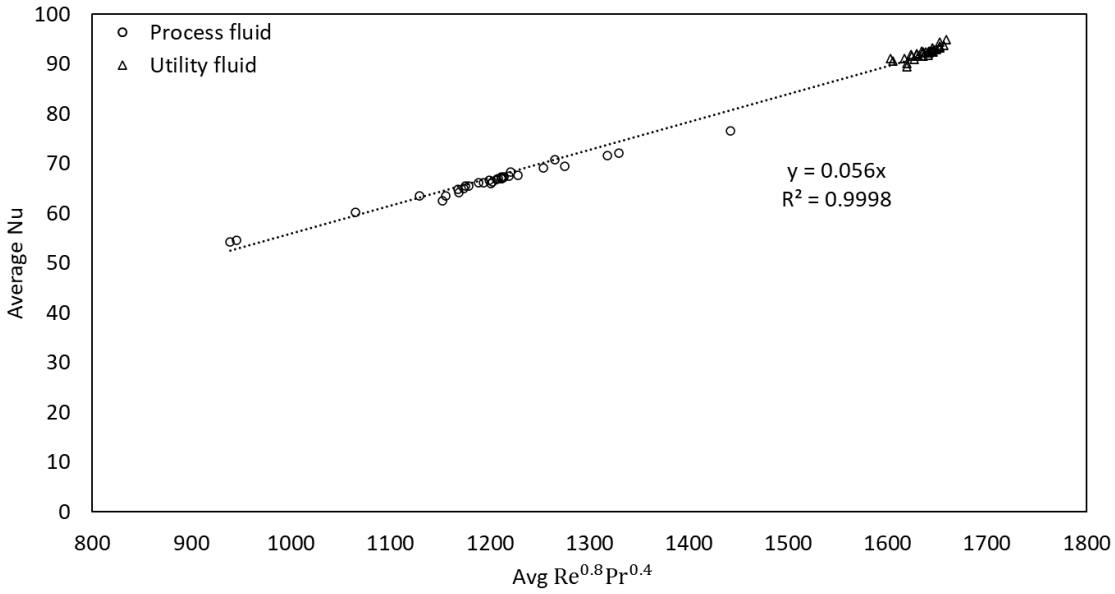

Figure 3-7: Collected experimental results fitted to the Dittus-Boelter correlation.

The fitted Nusselt number correlation is given by Eq. 3.6 and replaces the Gnielinski correlation that was originally used in the 2-D ROM.

$$Nu = \frac{\bar{h}L}{k} = 0.0564Re^{0.8}Pr^{0.4} \tag{3.6}$$

The collected experimental inlet conditions are then used as model input for comparison between model output and experimentally collected data for validation. Two parity plots (Figure 3-8) are created between all experiments performed in the campaign for result visualization. Across all experiments, the relative difference between model prediction and experimental value is 1.17 – 2.95 % and 0.79 – 2.23 % for process and utility sides, respectively. The relative difference between model prediction and experimental value for the solid phase temperature is 0.01 – 1.26 %.

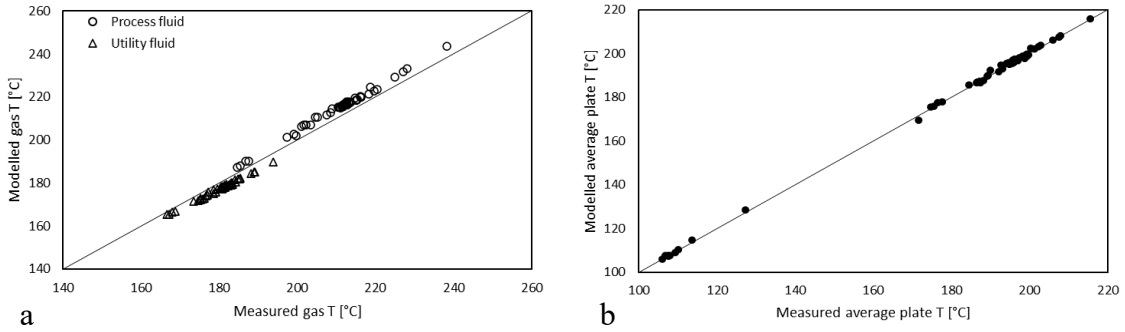

Figure 3-8: Parity plot between experimentally measured and model calculated a) process and utility fluid outlet temperatures, b) average CFHE plate temperatures.

While the model produces consistent results for the gas outlet temperatures, they are consistently above and below the measured results for the process and utility fluid outlet temperatures, respectively. Given that the heat flows from the process fluid to the utility fluid, this suggests that the model is underpredicting the heat transfer rate.

The solid phase temperatures produced by the 2-D ROM are almost identical to the experimentally measured result, confirming that the 2-D ROM fitted with a corrected heat transfer coefficient model can be used to accurately predict solid phase temperatures within a CFHE plate.

3.3.2. Flow channel surface temperature calculation

Due to difficulty in experimentally measuring the flow channel surface temperature, the surface temperature was estimated through modelling. As demonstrated in section 3.3.1, the 2-D ROM was capable of accurately predicting the CHFE plate temperature, and given the relative simple geometry of the CHFE plate, the model output temperature is used as a basis for extrapolating a flow channel surface temperature in the OpenFOAM simulations. Locations of the model output temperature and extrapolated surface temperature are shown in Figure 3-9.

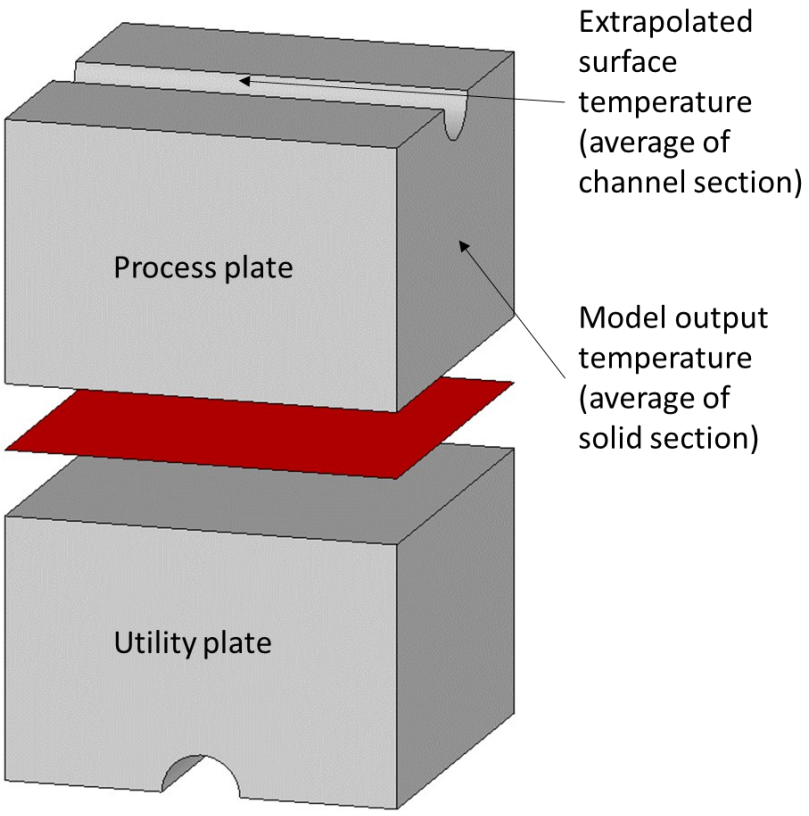

Figure 3-9: Illustration of lumped capacitance volume and heat flux plane (in red).

The 2-D ROM generates average temperatures using a lumped capacitance model for the solid phase, the volumes for a single process and utility channel in contact with each other are illustrated by Figure 3-9. The top represents the process plate and the bottom is the utility plate. Using the process and utility plate temperatures generated by the 2-D ROM, a heat flux going through the plate (see plane coloured in red) can be calculated. Using the calculated heat flux, model predicted plate temperature, and known dimensions of the plate, the surface temperature of the flow channel portion at the lumped volume can be calculated via Eq. 3.7.

$$\dot{Q} = k\frac{\Delta T}{\Delta y} \tag{3.7}$$

The 3-D CFHE plate model is constructed in OpenFOAM using these calculated surface temperatures as a boundary condition.

3.3.3. 3-D OpenFOAM model validation

Temperature sampling points identical to the physical FBG locations were created for the 3-D OpenFOAM model. This allows for validation of the 3-D model and a three-way comparison between the experimentally measured temperatures, 2-D ROM predicted temperatures, and 3-D OpenFOAM model predicted temperatures. 2-D ROM predicted temperatures used here for comparison are interpolated using the lumped capacitance temperatures from the model. They should reflect the temperatures of the CHFE plate at the FBG measurement locations.

Operating conditions from trial #5 in Table 3-1 are used to generate the flow channel surface temperatures and subsequent 3-D model with results shown in Figure 3-10.

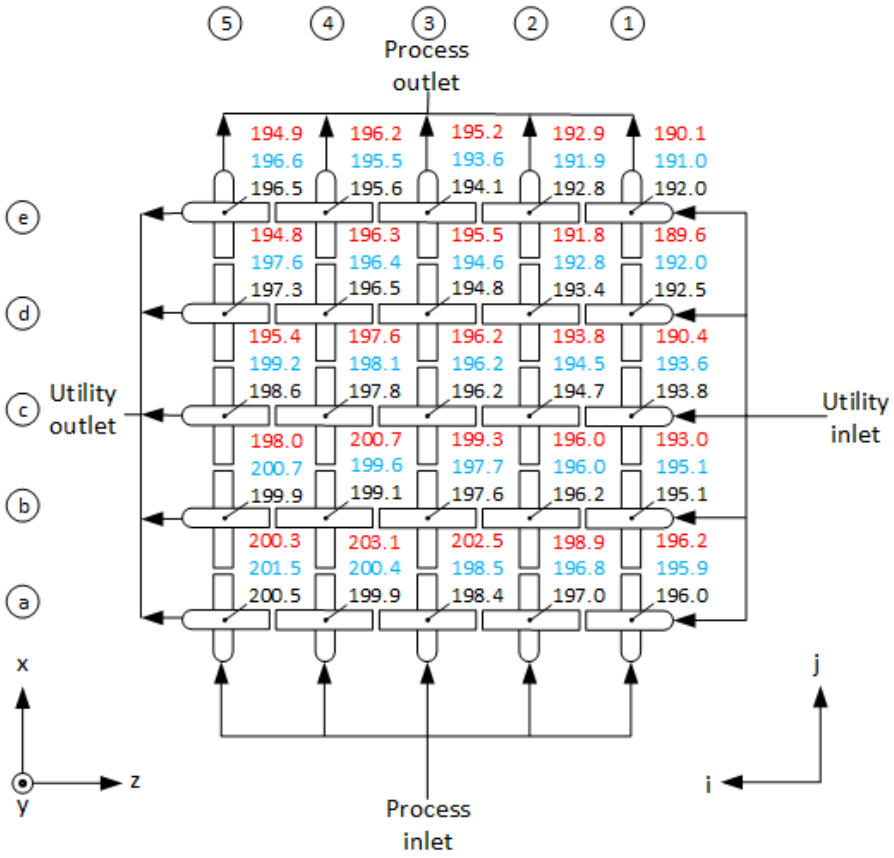

Figure 3-10: Solid temperature comparison for trial #5 between experimentally measured temperatures (red), 2-D ROM predicted temperatures (blue), and 3-D OpenFOAM model predicted temperatures (black).

The generated temperature profiles from the 2-D and 3-D models match the experimentally measured temperatures to a difference of less than 2 %. However, there are nodes with relatively large deviations, namely the nodes a3, e3, c1, c5. This can be explained by the physical experimental setup, where the gas inlet and outlets are located directly atop these nodes, as illustrated by Figure 3-10, causing a non-uniform heat distribution along the channels going in the direction of these nodes (c5 to c1 and a3 to e3). The model calculated results better match the experimentally measured results when moving away from these channels. The numerical models simulate all five flow streams simultaneously and produce a symmetrical temperature profile that is split along a 45° line going from nodes a5 to e1.

3.3.4. Conduction shape factor calculation

The shape of the flow channels changes the area available for heat conduction. This effect is notable for heat transfer in the two directions perpendicular to the flow, specifically the through plate direction and the transverse direction. The conduction shape factor S (Eq. 3.8) can be used to evaluate this effect. [40]

$$S = \frac{Q_{cond}}{k\Delta T} = \frac{\Delta x \Delta z}{\Delta y} \tag{3.8}$$

where $\Delta x \Delta z$ is the area of the heat transfer plane and Δy is the distance between the temperatures used to calculate the heat flux. Diagrams showing the geometries used for calculating shape factor are shown in Figure 3-11. The OpenFOAM solver chtMultiRegionFoam with the same settings as described in section 3.2.5 is used to determine the shape factors. Mesh independence of the new control volume was established through the same method described in section 2.5. The coarse, medium, and fine meshes contained 6912, 55,296, and 442,368 hexahedra cells. The heat flux was used to establish mesh independence. Using the fine mesh as reference, the through plate heat flux percentage error was calculated at 0.58 % and 0.24 % for the coarse and medium meshes, and the transverse heat flux percentage error was calculated at 1.92 % and 0.74 % for the coarse and medium meshes.

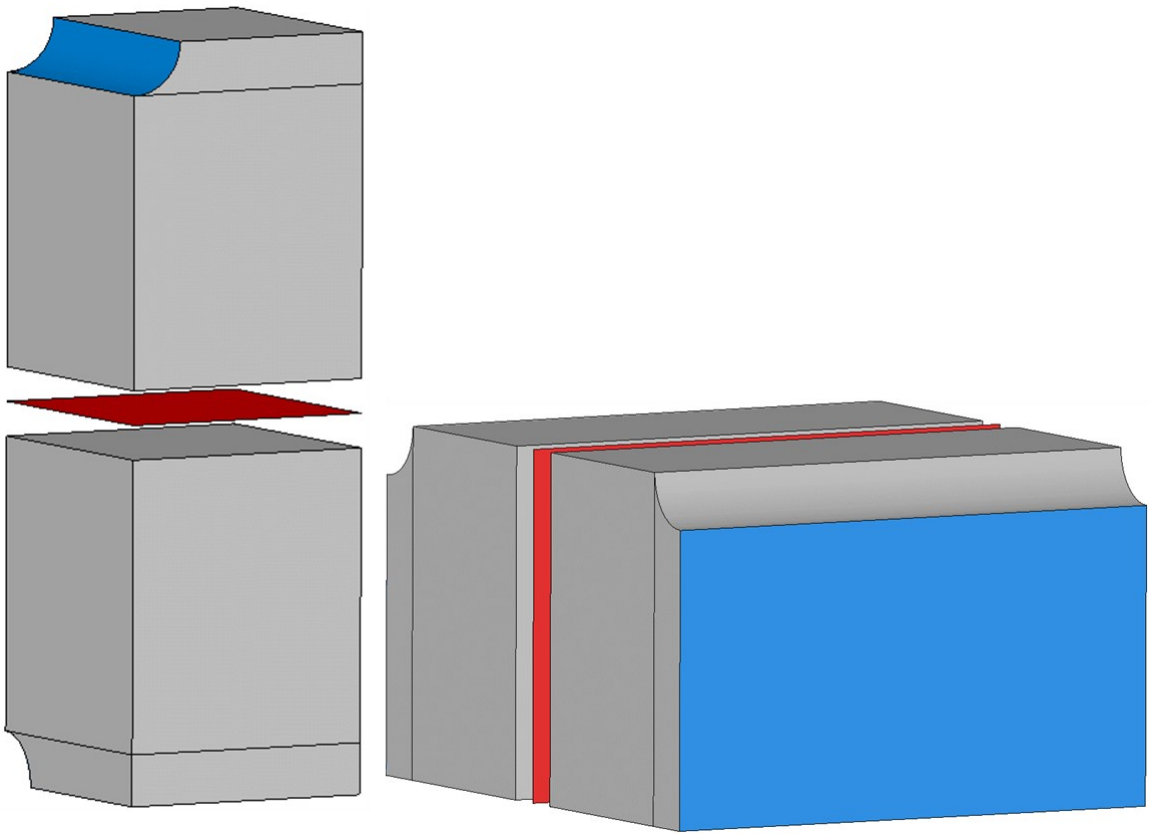

Figure 3-11: Geometries used for shape factor calculation. Left: through plate conduction; Right: transverse conduction. Heat flux is taken at the red plane ($\Delta x \Delta z$), surface temperatures are applied at the blue surfaces (distance is Δy).

The shape factor for through plate heat transfer was calculated for the center channels of the CFHE, represented by node b4 (Figure 3-10), using the heat flux through the center plane (Figure 3-11) taken from the CFD model and the difference between the channel surface temperatures. One quarter of the control volume of node b4 was fully meshed to reduce computational load. The results are then compared to the through plate shape factor of the region without the presence of a flow channel, which was determined to be 0.0028 m, to calculate a relative shape factor given in Table 3-2.

The shape factor for transverse heat transfer was calculated for node b4 on the process fluid half of the CFHE. Surface temperatures on both sides of b4 perpendicular to the direction

of flow were used with the heat flux taken at the plane between two nodes. The transverse heat transfer shape factor used for comparison is 0.01 m.

Table 3-2: Conduction shape factor for node b4

Node name	Shape factor [m]	Relative shape factor
Through plate	0.0024	82.5%
Transverse	0.0096	95.8%

The results are as expected, where the through plate relative shape factor is noticeably less than 100% and the transverse relative shape factor is near 100%. The through plate relative shape factor can be attributed to the much lower channel area, which is approximately 31% of the through plate heat transfer plane area. As the channel density increases for a given cross-flow heat exchanger geometry, the heat transfer plane area should subsequently decrease, and the relative shape factor will then increase with the greater channel density. The transverse relative shape factor was assumed to be 1 in the original 2-D ROM due to the relatively large channel area when compared to the transverse heat transfer plane area. This assumption was validated through 3-D modelling.

3.4. Conclusion

The solid phase temperature profile of a CFHE plate was measured using embedded fiber optic temperature probes known as FBGs in a series of steady-state heat transfer experiments. The solid phase temperature profile together with the fluid phase temperatures measured at the inlets and outlets were used to formulate an empirical heat transfer coefficient correlation based on the Dittus-Boelter correlation used in a 2-D ROM of the CFHE. The 2-D ROM results were subsequently compared against experimentally measured data and achieved high accuracy and consistency.

Using the 2-D ROM results, a 3-D OpenFOAM model of the CFHE was constructed to study the effects of through plate and transverse conduction shape factors. The resulting shape factors are 84.1 % and 96.4 % of the shape factors without the presence of a flow channel in the through plate and transverse directions, respectively.

4. Transient modelling and controllability study of an integrated heat exchanger reactor

Abstract

The closed loop controllability of several integrated heat exchange reactor (IHXR) designs ranging from 5 to 45 cross-flow channels in the heat exchanger section were investigated. An existing transient 2-D reduced-order heat exchanger model was modified and validated for its transient modelling accuracy through a series of bench scale heat transfer experiments. The heat exchanger model was used in combination with a transient reduced order reactor model for the closed loop IHXR process model development and PI controller tuning. The IHXR closed loop performance was investigated over a range of frequencies for inlet temperature and flow rate disturbances. The system was deemed to be generally stable in responding to inlet temperatures disturbances where it was able to provide 30% dampening for all disturbance frequencies except for the 5-channel design, where the time interval between disturbances needs to be less than 43 seconds or greater than 1042 seconds (stable at frequencies < 0.023 and >0.00096). As for changes in inlet flow rate, the system was unable to reject disturbances for all proposed designs, an additional fluid holding unit for flow dampening situated prior to the IHXR is required.

4.1. Introduction

IHXRs can be used in flue gas polishing to produce high purity carbon dioxide streams for carbon capture, utilization and storage [54]. The design of an IHXR features alternating heat exchanger and packed bed reactor sections, where the heat exchanger sections are composed of straight channel cross-flow printed channel heat exchangers (PCHE) and the reactor sections are made up of packed bed reactors. PCHEs are known for efficient heat

transfer within compact geometries, allowing for use in process intensified applications. [10, 49] The proposed IHXR design allows for fuel input directly into the reactor section and utility fluid input into the heat exchanger section, facilitating precisely controlled rates of reaction and heat exchange [11].

Numerical simulation studies for PCHEs have been used to determine their performance in context of Brayton cycles using supercritical CO_2 as the working fluid [15, 16, 17, 18, 19]. Similarly, the intended application of the proposed IHXR for high CO_2 content flue gas polishing also involves using CO_2 as the working fluid. In addition, simulation studies have been used to determine the performance of IHXRs for process intensified applications combining heat exchange and catalytic reaction [49]. There is, however, a lack of studies concerning the controllability of an IHXR through means of numerical modelling. It is capital intensive to manufacture heat transfer equipment for physical experimentation, thus it is advantageous to determine the controllability of a proposed design prior to full scale manufacturing.

Furlong et. al. has developed a 2-D transient reduced order heat exchanger model (2-D ROM) for modelling the dynamic behaviour of PCHEs, the model grants high modularity to the user in providing the ability of modifying the geometry and available fluid-to-wall fluid convective heat transfer correlation for adapting to various PCHE geometries [20]. Alongside the use of a reduced order reactor model, it is possible to develop process models of proposed IHXR geometries to analyze their closed loop controllability.

This work will focus on the closed loop controllability of the IHXR through analyzing the ability of the IHXR to reject inlet temperature and flow rate disturbances via reduced order modelling. Two major components make up this study, the first details the transient

experiments undertaken on a bench-scale cross-flow heat exchanger to derive a geometry specific fluid-to-wall convective heat transfer correlation. This convective heat transfer correlation is then used to validate the transient modelling capability of the 2-D ROM through comparison of the simulated temperature time series against experimentally measured temperature time series. Once validated, the 2-D ROM replaces its geometry specific Nusselt number correlation with a generalized correlation for IHXR process modelling. The second component of this work focuses on using the 2-D ROM alongside a reduced order reactor model for developing process models of potential IHXR designs ranging from 5 to 45 flow channels. The resulting process models are then used for PI controller tuning and to perform closed-loop performance analysis on the IHXR designs. The closed-loop performance is assessed with inlet temperature and flow rate disturbances to determine the resonant peak and frequency ranges of the disturbances for which the IHXR can provide 30% dampening.

4.2. Methodology

4.2.1. Transient heat transfer experiments and modelling for reduced order model validation

A bench scale micro-channel cross-flow heat exchanger was manufactured and fitted with resistance temperature detectors (RTD) for inlet and outlet gas phase temperature measurement, and Fibre Bragg Grating (FBG) temperature probes for solid phase temperature measurement [21]. The FBGs are embedded within the heat exchanger between the flow channels for temperature measurement, as shown in Figure 4-1a as the small holes in the middle of the plate.

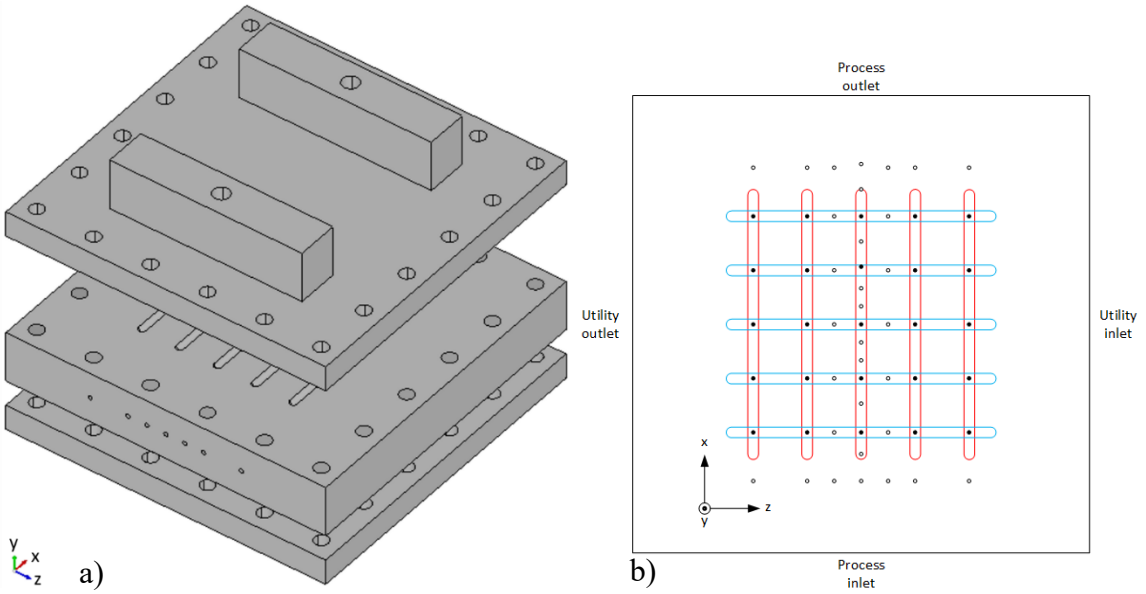

Figure 4-1: a) image of the core cross-flow heat exchanger assembly; b) diagram of the cross-flow heat exchanger plate showing inlet and outlet locations and FBG locations.

The gas phase inlet and outlet temperatures were measured across multiple heat transfer experiments using CO_2 as the working fluid on both sides of the exchanger while varying the inlet gas flow rate and temperatures to develop the fluid-to-wall convective heat transfer coefficient correlation. The hot stream is named the process fluid and the cold stream the utility fluid. Figure 4-1b shows the positioning of the FBG probes as well as the fluid inlet/outlet. The probes located at the intersection of the two fluid channels are denoted using a filled in circle and are responsible for data acquisition directly used in this study. The probes denoted by a hollowed-out circle are to check for data consistency.

The experiments were carried out by first setting the heat exchanger to operate at a base case condition and bringing it to steady-state as measured by a constant solid phase temperature, and then introducing a step-change to measure the temperature evolution with respect to time. The experimental set-up is considered to have reached steady-state conditions once the solid phase temperatures change less than 0.5 °C within five minutes.

The base case condition was held at a process fluid inlet temperature of 250 °C, utility fluid inlet temperature of 150 °C, process fluid inlet flow rate of 7 kg/h, utility fluid inlet flow rate of 9 kg/h, and both sides are held at an inlet pressure of 9 bar. The step-changes were only introduced to the process fluid with the utility fluid conditions held constant across all experiments.

The step-changes to the base case conditions are given in Table 4-1. All the step-changes are averages, and were achieved by changing the heater power and valve opening for respectively the temperature and flow rate changes to avoid the influence from dynamics of the heater and valve controllers. The step-changes here are chosen due to the physical limitations of the system, where the maximum sustainable gas flow rate is 9 kg/h and maximum sustainable gas temperature is approximately 280 °C.

There are two parts for each experiment: the first part where the step-change is applied at the steady-state base case condition, and the second part where the step-change is reversed at the new steady-state condition returning to the previous base case condition, resulting in two sets of data recorded from each transient experiment. At least two repeating trials were conducted in randomized order for each transient experiment to ensure consistency of data.

Table 4-1: Applied transient experiment step-changes with respect to the base case conditions

Experiment #	Process fluid temperature change	Process fluid flow rate change
1	-	+1 kg/h
2	-	+2 kg/h
3	-	−1 kg/h
4	-	− 2 kg/h
5	+ 20 °C	-
6	− 20 °C	-
7	− 40 °C	-

4.2.1.1. Custom heat transfer coefficient correlation

The steady-state gas and solid phase temperature data collected from the experiments were compiled to calculate the average fluid-to-wall fluid convective heat transfer coefficient for each respective experiment. The average heat transfer coefficient (Eq. 4.1) is calculated by performing an energy balance on the inlet and outlet gases to calculate the heat duty, then divided by the difference between the average gas phase and solid phase temperatures.

$$\dot{m}(c_{p,in}T_{g,in} - c_{p,in}T_{g,in}) = Q = hA\left(T_{g,avg} - T_{s,avg}\right) \tag{4.1}$$

The average heat transfer coefficient was then used to calculate the Nusselt number. This procedure was repeated across all experiments to calculate all Nusselt numbers, and then each average Nusselt number was plotted against the average Reynolds number and average Prandtl number to derive Eq. 4.2.

$$Nu = \frac{hD_h}{k} = 0.0564Re^{0.8}Pr^{0.4} \tag{4.2}$$

The equation form, specifically the exponents used for Re and Pr, were based on the Dittus-Boelter equation with the leading coefficient obtained from regression. The experimentally recorded Re and Pr used for fitting ranges from 5800 – 13,700 and 0.737 – 0.783, respectively, achieving an R^2 of 0.9998. Although there are separate Pr exponents for heating and cooling in the Dittus-Boelter equation, the fitted results did not differ significantly, and thus 0.4 was used as the Pr exponent.

Eq. 4.2 was inserted into the 2-D ROM described in Furlong et al. to replace its Nusselt number correlation [20]. The correlation change was then validated by generating time series of average gas and solid phase temperatures and comparing the results against the experimentally measured time-series.

4.2.1.2. Transient heat transfer model validation

Eq. 2 replaces the Nusselt number correlation used by the 2-D ROM described in Furlong et al. to validate its transient modelling capabilities [20].

Transient heat transfer model validation was undertaken by comparing the evolution of the simulated temperatures and the experimentally recorded temperatures. The comparison between recorded and simulated temperatures for experiment 1 (Table 4-1) are shown in Figure 4-2 and Figure 4-3 as an example. The simulated transient temperature profiles closely match the experimentally measured temperature profile. When compared to the measured temperatures, the simulated temperatures show an average relative error of 1.96% and 1.57% for the process and utility fluid temperatures, respectively.

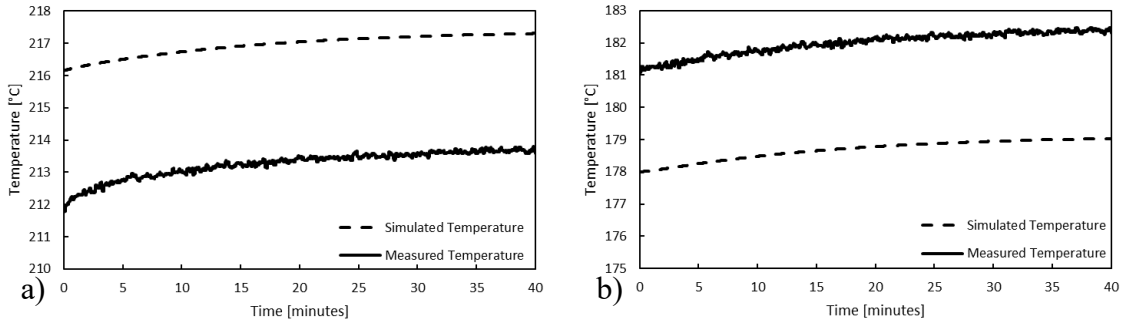

Figure 4-2: Gas phase outlet temperature evolution for experiment 1 (Table 4-1): a) process fluid outlet temperature; and b) utility fluid outlet temperature.

The simulated solid phase temperature closely corresponds to the experimentally measured temperature and predicts the solid phase temperature to a higher degree than the gas phase temperatures at a difference of less than 1 °C, or an average relative error of 0.24%.

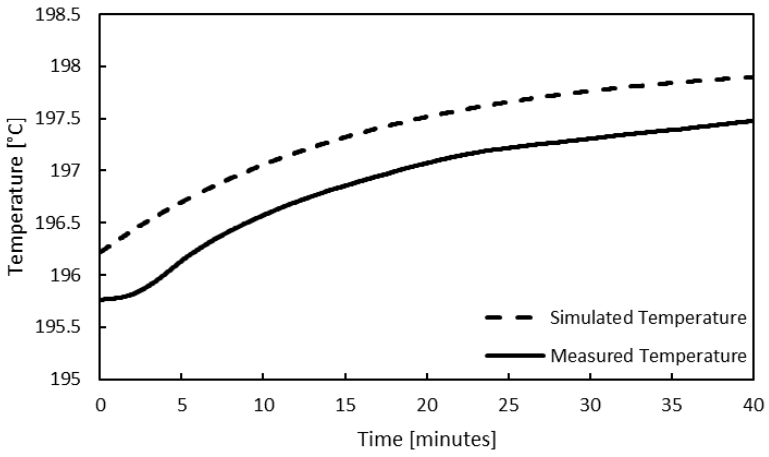

Figure 4-3: Solid phase temperature evolution experiment 1 (Table 4-1).

4.2.2. Transient modelling and time constant determination of general heat exchanger geometry

4.2.2.1. Heat exchanger section time-series

The heat transfer coefficient correlation presented in Eq. 2 is specific to the bench-scale experimental set-up, which includes the entrance effects in the experimental set-up. Thus the custom correlation needs to be changed to a correlation more suited for general heat exchanger geometries to model the proposed heat exchanger designs. The original Dittus-Boelter correlation (Eq. 3) was chosen as the generalized correlation to model the proposed designs [52].

$$Nu = 0.023Re^{0.8}Pr^{0.4} \tag{4.3}$$

The proposed heat exchanger design used for time-series modelling is comprised of five flow plates (in order of utility, process, fuel, process, utility) to make up the simplest IHXR composed of a single repeating unit (combination of process, fuel, process, utility plates) enclosed by a utility plate on top. Each plate consists of repeating semi-circular channels of the exact same dimensions. All plates and channels share the same dimensions, with process and utility channels placed in a cross-flow configuration to increase heat transfer.

The plate designs are shown in Figure 4-4a with the heat exchanger section highlighted in red, the channel dimensions and plate thickness are given in Figure 4-4b. The heat exchanger section's length and width are the product of the number of channels and individual channel dimensions, i.e. a 5-channel plate would have a length and width of 0.025 m. The height of the heat exchanger design used in this study is 0.0175 m, the combined height of five flow plates.

The gas flow rate for both the process and utility fluid is adjusted to per flow channel. The time constant of the IHXR is a function of the number of flow channels per process/utility plate and changes accordingly. It is however not a function of the number of IHXR repeating units, time constants obtained from a single-unit design can be expanded for use in multiple-unit designs as long as the number of flow channels per flow plate does not change. The fuel plate design is simplified to have the same channel length as the process plate channels as the fuel temperature control is not part of study.

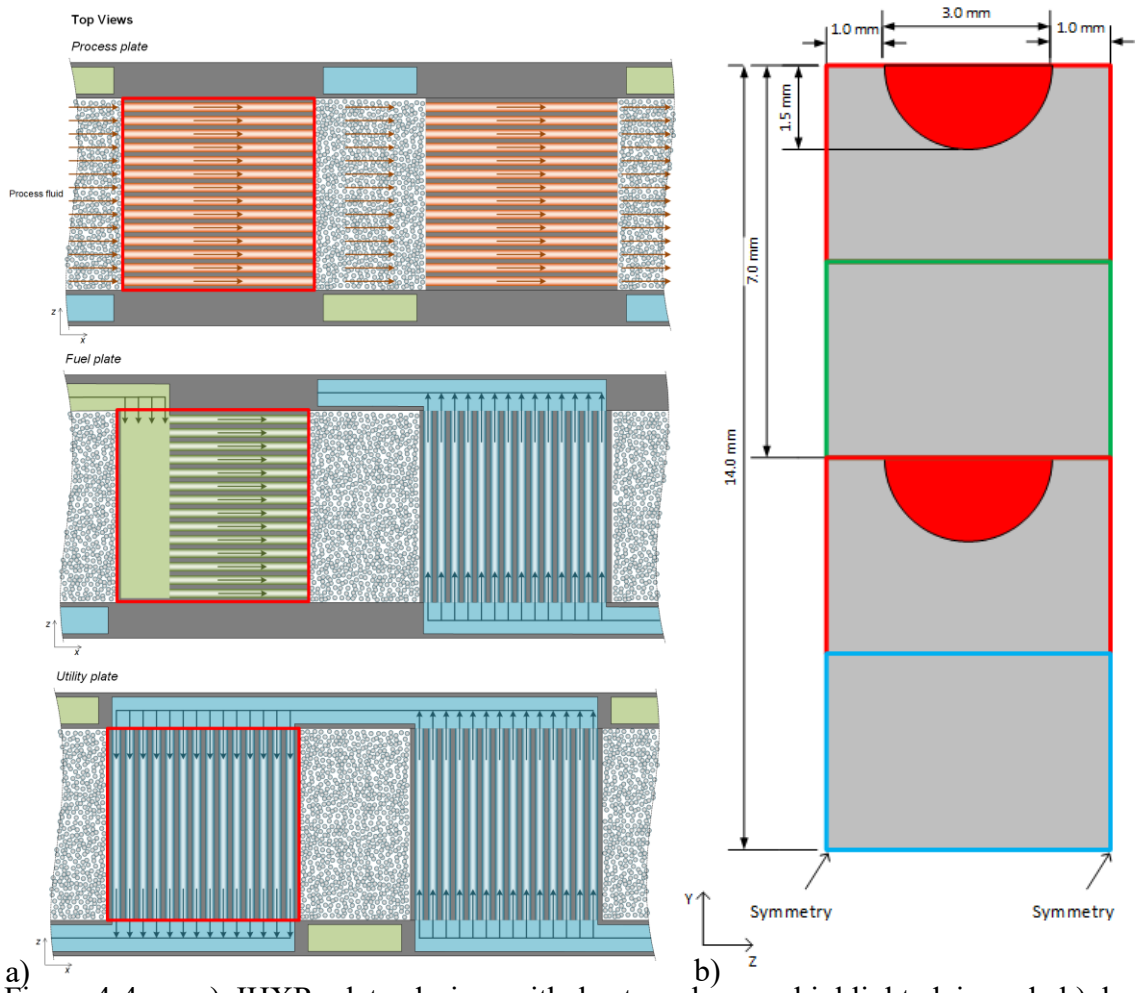

Figure 4-4: a) IHXR plate design with heat exchanger highlighted in red. b) heat exchanger channel and plate dimensions, each plate is colour-coded to match figure a).

Heat exchanger designs ranging from 5 to 45 cross-flow channels using the channel and plate dimensions shown in Figure 4-4b were simulated to determine the time constants for each design. Each design places the same number of cross-flow process, fuel and utility channels according to the configuration given in Figure 4-4a. The resulting geometry is a square heat exchanger for all designs due to the matching number of channels in the process and utility plates.

Each simulation was conducted by applying a temperature step-change to a previously steady-state simulation, the simulated solid phase temperatures are then collected and

averaged to create an overall temperature time-series for time constant calculation. The base case conditions and step-change conditions are given in Table 4-2. The simulation conditions are set to approximately match that of the bench-scale experiments described in section 4.2.1, and without the physical limitations, the step-changes are set to reach approximately that of the maximum allowable temperature and flow rates on the bench-scale experimental set-up.

The time constant was determined as the time taken for 63.2% of the temperature change to occur.

Table 4-2: Base case and step-change conditions for transient heat exchanger simulation.

Base case conditions	**Value**	**Unit**
Flow rate	1.8	kg/h/channel
Process fluid temperature	250	°C
Utility fluid temperature	150	°C
Step-changes		
Process fluid temperature	+ 50	°C

4.2.2.2. Packed bed time series

The packed bed section of the IHXR was modelled via reduced order modelling with advection and convection removed. This approach assumes an infinitely high heat transfer coefficient so that the gas and solid phase has identical temperatures during reaction, as the catalyst particles used for modelling the packed bed section are relatively small (0.003 m in diameter). The reduced order packed bed is described by a set of two equations in which the gas phase equation (Eq. 4.4) accounts for the material balance and the solid phase equation (Eq. 4.5) accounts for the energy balance.

$$\frac{\partial\left(u_g \rho_g Y_g\right)}{\epsilon \rho_g \partial x} = R_g \tag{4.4}$$

$$\frac{\partial(\rho_s H_s)}{\partial t} = q_{R,s} = H_R R_g \tag{4.5}$$

Eq. 4.4 as written equates the gas phase reaction rate R_g to that of the spatial accumulation term discretized across the x-axis, this assumes that all changes in concentration along the x-axis is a result of reaction. Eq. 4.5 then relates the gas phase reaction exotherm to the temporal accumulation term, which assumes that all temperature change over time is due to the gas phase reaction. This is possible because of the assumption that there is an infinitely high heat transfer coefficient, such that all temperature change in the solid phase can be related to the gas phase reaction term. The packed bed time constant is then calculated by solving Eq. 4.4 and Eq. 4.5 simultaneously as a system of ODEs.

The packed bed time constant is not a function of the operating conditions but that of geometry, so that a set of known working operating conditions can be used for simulation. The parameters and operating conditions used for this calculation are taken from Ge et al. [49]

This procedure is repeated until the temperature in the final axial discretization achieves a temperature increase of 50 °C with respect to the initial temperature [49]. The specific packed bed inlet conditions are given in Table 4-3, where the flow rate is given in terms of flow rate per flow channel as shown in Figure 4-4.

Table 4-3: Packed bed inlet conditions

Property	Value	Unit
Inlet mass flow rate per flow channel	1.908	kg/h
Inlet species mass fraction		
CH_4	0.0013	-
O_2	0.022	-
CO_2	0.97	-
Inlet temperature	500	°C
Inlet pressure	1000	kPa

The calculated solid phase temperature in the final axial discretization obtained from Eq. 5.5 is used to create a time-series of the packed bed temperature, which is then used to obtain the packed bed time constant. As the temperature evolution within the packed bed occurs in one direction (axial) and is irreversible, using the final axial discretization to estimate the time constant provides a conservative estimate for the outlet gas T time constant.

4.2.3. Feedback loop controller tuning

An IHXR (Figure 4-5) comprised of 5 packed bed and 4 heat exchanger sections is proposed for a controllability study. The IHXR configuration starts off with a packed bed section and ends in a packed bed section, with flue gas pre-heating taking place in an additional heat exchanger. This design allows for additional external heat exchangers to be integrated into the process for flue gas pre-heating and or post-polishing flue gas cooling.

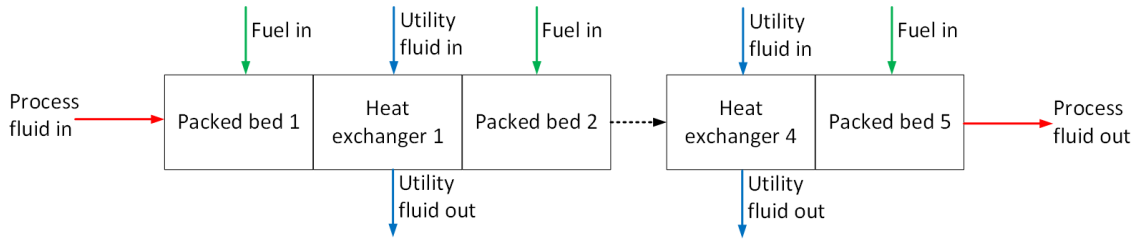

Figure 4-5: Layout of proposed IHXR design, including process, utility fluid and fuel flows

A closed feedback loop can be constructed using the time constants obtained from section 4.2.2 as shown in Figure 4-6. The feedback loop implements a PI controller where the proportional and integral parameters are obtained from the Direct Synthesis Method [55]. The Direct Synthesis Method has the advantage of defining the desired behaviour of the controlled feedback loop using a first order plus dead-time (FOPDT) model, then developing the required tuning parameters to achieve this desired level of control.

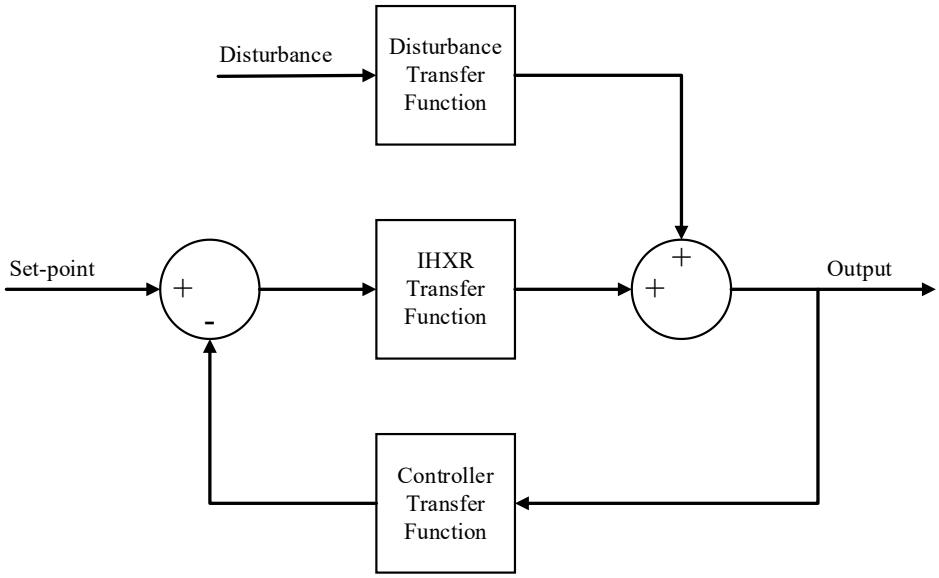

Figure 4-6: Illustration of IHXR within closed control loop

Skogestad's method was used to reduce the process model of the feedback loop into a FOPDT process model. The Direct Synthesis Method (Eq. 4.6 – 4.7) was then used on the FOPDT model to determine the tuning parameters [55].

$$K_C = \frac{1}{K_P}\frac{\tau}{\lambda + \theta} \tag{4.6}$$

$$\tau_I = \tau \tag{4.7}$$

where K_C is the proportional constant, K_P is the steady-state process gain, τ is the time constant of the FOPDT model, θ is the deadtime of the FOPDT model, and λ is the closed-loop response time and is taken as 3θ.

4.2.4. Bode diagram and controllability study

Using the time constants obtained from section 4.2.2, a Bode plot can be constructed for each IHXR design to relate the amplitude ratio of the closed-loop system with a PI controller to the frequency response of the system to the respective disturbance. The resonant peak of the system can then be determined from the Bode diagram as the region of frequency response with the highest amplitude ratio. If the amplitude ratio within the resonant peak exceeds unity, the system becomes unstable.

The process model of the proposed IHXR is composed of the process gain function as well as the controller gain function, as described by Eq. 4.8.

$$\frac{1}{1 + G_C(i\omega)G_P(i\omega)} = \frac{1}{1 + \left(k_C\left(1 + \frac{1}{\tau_I i\omega}\right)\right) \times \frac{1}{(\tau_{bed} i\omega + 1)^5} \times \frac{1}{(\tau_{HE} i\omega + 1)^4}} \tag{4.8}$$

Adding the disturbance gain function described by Eq. 4.9.

$$G_D(i\omega) = \frac{K_D}{\sqrt{(\tau_{bed}\omega)^2 + 1}^5 \times \sqrt{(\tau_{HE}\omega)^2 + 1}^4} \tag{4.9}$$

The relationship between amplitude ratio (AR) and frequency response ω can be written as Eq. 4.10 as the product of the magnitude of Eq. 4.8 and 4.9. The Bode diagram of the IHXR

is then constructed by plotting Eq. 4.10 using a Python script on the closed-loop process illustrated in Figure 4-6.

$$AR = \frac{|G_D(i\omega)|}{|1 + G_C(i\omega)G_P(i\omega)|} \tag{4.10}$$

4.3. Results and discussion

4.3.1. IHXR time constant and PI controller parameters

As described in section 4.2.1.1, heat exchanger designs ranging from 5 to 45 cross-flow channels were simulated and their time constants calculated to build a process model of the proposed IHXR designs. Two separate sets of time constants, one for each experiment described in Table 4-2, were calculated for each design. The results are denoted as case #1 for temperature inlet condition change and case #2 for flow inlet condition change. The heat exchanger time constant is taken as the time constant for the outlet process fluid temperature in order to align with the most likely measured variable in a real process. In addition, all time constants (process fluid outlet, utility fluid outlet, solid phase temperature) collected from the heat exchanger simulations do not differ by more than 8.8% with experimentally measured process outlet temperature time constant.

The heat exchanger time constants along with the packed bed time constant for each respective design is given in Table 4-4. As the flow rate for the packed bed section is a direct function of the number of flow channels, the time constant does not change with regards to increases in the number of flow channels in the heat exchanger section.

The heat exchanger time constants increase as the number of flow channels increase; this is expected. Although the increase in the number of flow channels increases the amount of

available heat transfer area, it is outweighed by the increase in both the amount of thermal mass from heat transfer fluid and heat exchanger itself.

Table 4-4: Time constants for various heat exchanger designs

	Case #1		Case #2	
# of channels	HE τ [s]	PB τ [s]	HE τ [s]	PB τ [s]
5	6.25	4.10	6.60	4.1
10	7.20	4.10	7.10	4.1
15	7.90	4.10	7.70	4.1
20	8.75	4.10	8.25	4.1
25	9.70	4.10	8.85	4.1
30	10.80	4.10	9.55	4.1
35	11.90	4.10	9.80	4.1
40	13.00	4.10	10.55	4.1
45	14.20	4.10	11.30	4.1

Employing the process model for the 5-channel design, the outlet response subject to an inlet set point unit step change is shown in Figure 4-7.

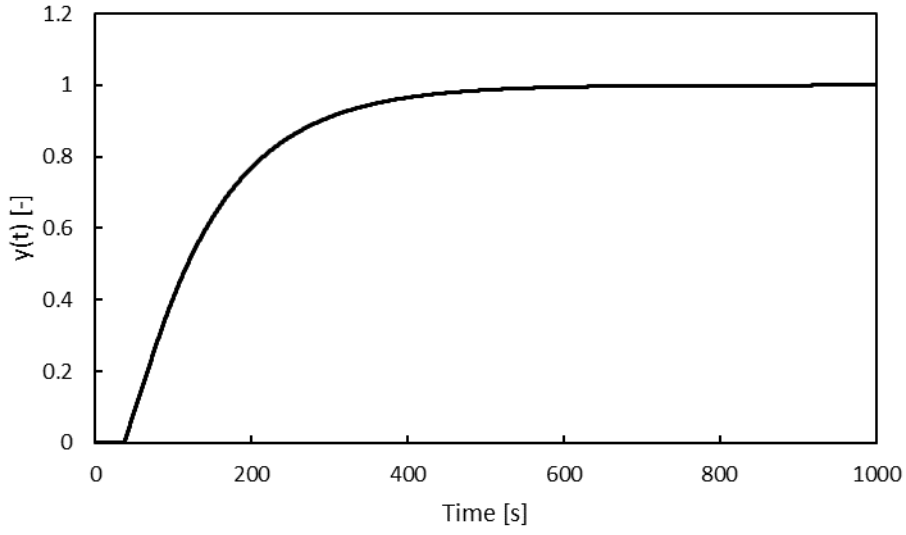

Figure 4-7: Output response for a 5-channel IHXR design given an inlet set point of unity

Then given the time constants, the PI controller parameters calculated using Eq. 6 – 7 are given in Table 4-5.

Table 4-5: IHXR PI controller parameters

# of channels	K_C	τ_I
5	-3.13E-05	9.9
10	-1.75E-05	10.65
15	-1.27E-05	11.55
20	-1.01E-05	12.38
25	-8.49E-06	13.28
30	-7.25E-06	14.33
35	-6.57E-06	14.7
40	-6.04E-06	15.83
45	-3.99E-06	16.95

Employing the controller parameters, the output for a 5-channel IHXR subject to inlet temperature and mass flow rate disturbances are displayed in Figure 4-8. The output shows response to an inlet temperature disturbance of unity and mass flow rate disturbance of 0.001 kg/s.

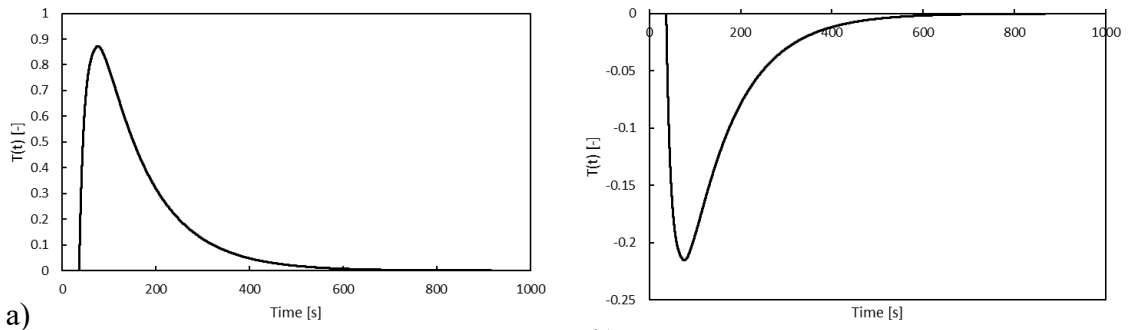

Figure 4-8: a) Inlet temperature disturbance; b) inlet mass flow rate disturbance

From Figure 4-8 it is evident that temperature disturbances can be effectively rejected with a minor overshoot, however flow rate disturbances cannot, as the overshoot is approximately 2000 times the disturbance.

4.3.2. Bode diagram and controllability study

Bode diagrams were constructed for each IHXR design using the time constants obtained from sections 4.3.1 and the procedure outlined in 4.2.4.

Figure 4-9 shows the Bode Plot of the 5- and 45-channel design for temperature and inlet flow rate set-point disturbance in log-log scale. The amplitude ratio does not exceed unity for almost all frequencies when responding to inlet temperature disturbances and that all frequencies of disturbances can be rejected for this IHXR design. Deeming the system stable in response to most inlet temperature disturbances. As for inlet flow rate disturbances, the system is only stable at extremely low and high frequencies, with most frequencies exhibiting amplitude ratios much higher than unity. Deeming the system unstable in response to all inlet flow rate disturbances.

It is also evident that the resonant peak decreases as the number of channels increases for the heat exchanger section when facing temperature disturbances, leading to increased stability as the IHXR increases in heat transfer capacity. Conversely, the resonant peak increases as the number of flow channels increases in the heat exchanger section when facing flow rate disturbances.

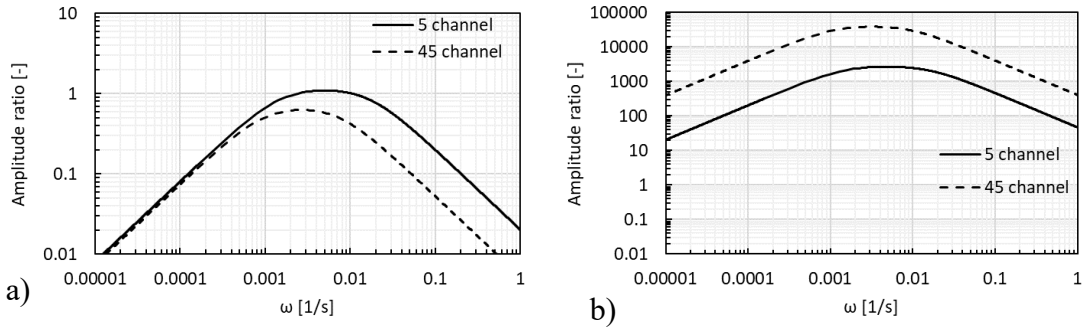

Figure 4-9: Log-log plot of amplitude ratio vs frequency for 5- and 45-channel IHXR designs in response to a) inlet process fluid temperature disturbances; b) inlet flow rate disturbances.

The range of instability for all designs in response to inlet temperature disturbances are given in Table 4-6, with the resonant peaks expressed in terms of amplitude ratio. The range of instability is defined as the range of frequencies for which the amplitude ratio is above 0.7 for a 30% dampening on the incoming disturbance. The individual range of instability and resonant peak data from each heat exchanger design in response to inlet temperature disturbances decreases as the number of flow channels increases, with the IHXR becoming more stable.

The IHXR can provide 30% dampening for all designs for disturbances occurring at time intervals less than 43 seconds or greater than 1042 seconds. Conversely, the IHXR at its current design cannot effectively control for inlet flow rate disturbances, and so the relevant values are not included in Table 4-6.

Table 4-6: Range of instability, resonant peak and related frequency at resonant peak for the IHXR in response to inlet temperature disturbances

# of flow channels	Range of instability (Hz)	Resonant peak	Frequency at resonant peak (Hz)
5	$0.00096<\omega<0.023$	1.09	0.0049
10	$0.0013<\omega<0.017$	0.99	0.0045
15	$0.0014<\omega<0.013$	0.90	0.0041
20	$0.0016<\omega<0.010$	0.83	0.0038
25	$0.0018<\omega<0.0073$	0.77	0.0037
30	$0.0021<\omega<0.0049$	0.72	0.0033
35	stable	0.69	0.0030
40	stable	0.66	0.0029
45	stable	0.63	0.0027

The IHXR is downstream of other processing units such as a direct contact cooler for water vapour removal. In cases with inlet flow rate disturbances coming from upstream processing units that are unable to be rejected by the IHXR, a fluid holding unit may be able to provide the required dampening.

4.4. Conclusion

In this work, the closed loop controllability of an IHXR was studied via reduced order modelling. Transient heat transfer experiments were undertaken on a bench-scale cross-flow heat exchanger, in which the results were compiled and used to formulate a geometry dependent Nu correlation. The Nu correlation was then used to validate the transient modelling capability of the 2-D ROM through comparison with experimental results.

Several IHXR designs ranging from 5 – 45 flow channels were then created for the closed loop controllability study. The validated 2-D ROM, now fitted with a general Nu correlation along with a reduced order packed bed reactor model was used to derive time constants and the subsequent IHXR process models. Then each IHXR design was subjected

to an inlet temperature and flow rate disturbance to determine its stability defined by the ability to provide 30% dampening for each type of disturbance.

The results showed that the IHXR is generally stable in response to inlet temperature disturbances for all designs evaluated with the exception of the 5-channel design, where the IHXR is stable only if the time interval for disturbances is less than 43 seconds or is greater than 1042 seconds. However, the IHXR is unable to effectively reject inlet flow rate disturbances regardless of the IHXR design. Additional equipment such as a fluid holding unit is required upstream of the IHXR to address inlet flow rate disturbances.

5. Pressurized Chemical Looping Flue Gas Polishing via Novel Integrated Heat Exchanger Reactor

Abstract

Pressurized chemical looping combustion (PCLC) provides the benefit of simplifying the carbon capture process by generating a flue gas stream with high CO_2 concentration. However, flue gas polishing is required to remove the residual impurities for pipeline transport. The integrated heat exchanger reactor (IHXR) is a promising method for flue gas polishing while maximizing useful heat recovery that incorporates alternating catalytic packed beds with interstage cooling via printed circuit heat exchangers (PCHE). This work offers a design process for an IHXR capable of polishing a flue gas stream from a 100 MW_{th} natural gas fired PCLC unit while recovering 1.6 MW of useful heat in the form of saturated steam at 180 °C. Simulation work performed in Aspen HYSYS was used to determine the polished flue gas outlet species concentrations as well as the required number and size of the packed bed sections. The PCHEs for interstage cooling were sized via a thermal circuit approach. The final IHXR consists of six packed beds at 0.06 m in length and five PCHEs at 0.265 m in length combing to a total IHXR length of 1.685 m. The height and width of the IHXR is shared between the packed beds and PCHEs at 0.91 m and 0.45 m respectively. The resulting IHXR is capable of recovering heat at a rate of approximately 2.3 MW/m^3.

5.1. Introduction

Carbon capture, utilization, and storage (CCUS) is a proposed framework to reduce the carbon footprint of industrial processes in Canada. [56] One CCUS technology is pressurized chemical looping applied to combustion (PCLC). PCLC generates heat by

using a dual fluidized bed configuration of air reactor (AR) and fuel reactor (FR), where a metal oxide (MeO) oxygen carrier reacts with fuel in the fuel reactor before being cycled into the air reactor for oxidation. [57] The FR uses hydrocarbon fuels, typically natural gas, to react with the oxygen provided by the oxygen carrier to produce a flue gas stream that mainly consists of unconverted fuel, CO_2, H_2O, and trace impurities such as CO. [57] This promising alternative for natural gas combustion thus produces flue gas with low N_2 content without using energy intensive cryogenic air separation for its oxidizer, such as in oxy-fuel combustion. [49]

The flue gas exiting the PCLC unit still requires polishing prior to transportation due to strict pipeline specifications for the composition of CO_2 streams. This work adheres to the Alberta Carbon Trunk Line (ACTL) pipeline specification, limiting CH_4 and CO content to below 1 mol% each. [4] The integrated heat exchanger reactor (IHXR) is the proposed technology for flue gas polishing which removes unconverted fuel from PCLC flue gas through catalytic combustion via alternating adiabatic packed beds while providing interstage cooling and heat recovery through compact printed circuit heat exchangers (PCHEs). PCHEs are currently deployed in high intensity heat transfer operations such as supercritical-CO_2 Brayton cycles with numerous works detailing its performance analysis through both numerical and experimental means, making it an excellent unit operation for interstage cooling between adiabatic packed beds. [16, 19] The intensified compact design offered by the IHXR was previously used in an energy intense operation for the catalytic deoxygenation of oxy-fuel combustion flue gas, making it a promising method for PCLC flue gas polishing. [49, 54]

Figure 5-1 depicts the top view of the process, reactant, and utility plates that make up a single repeating IHXR unit. [54] Each repeating unit consists of four plates total in the order of process, reactant, process, and utility, and it is enclosed at the top by a final utility plate for the complete layout of the IHXR. [54] The process fluid is the PCLC flue gas following water vapour removal and this stream enters the packed bed section through the process plate. The reactant fluid is the O_2 stream injected into each packed bed section to enable combustion. Although this implies that there is still a requirement for an O_2 stream, it is significantly lower than for oxy-fuel fired combustion units. The utility fluid is used to cool the process gas after a desired extent of reaction is reached in each packed bed section. The packed bed and heat exchanger sections will share the same height and width as a function of the number of repeating PCHE units and flow channels respectively, and the length of the two different section types will be sized separately.

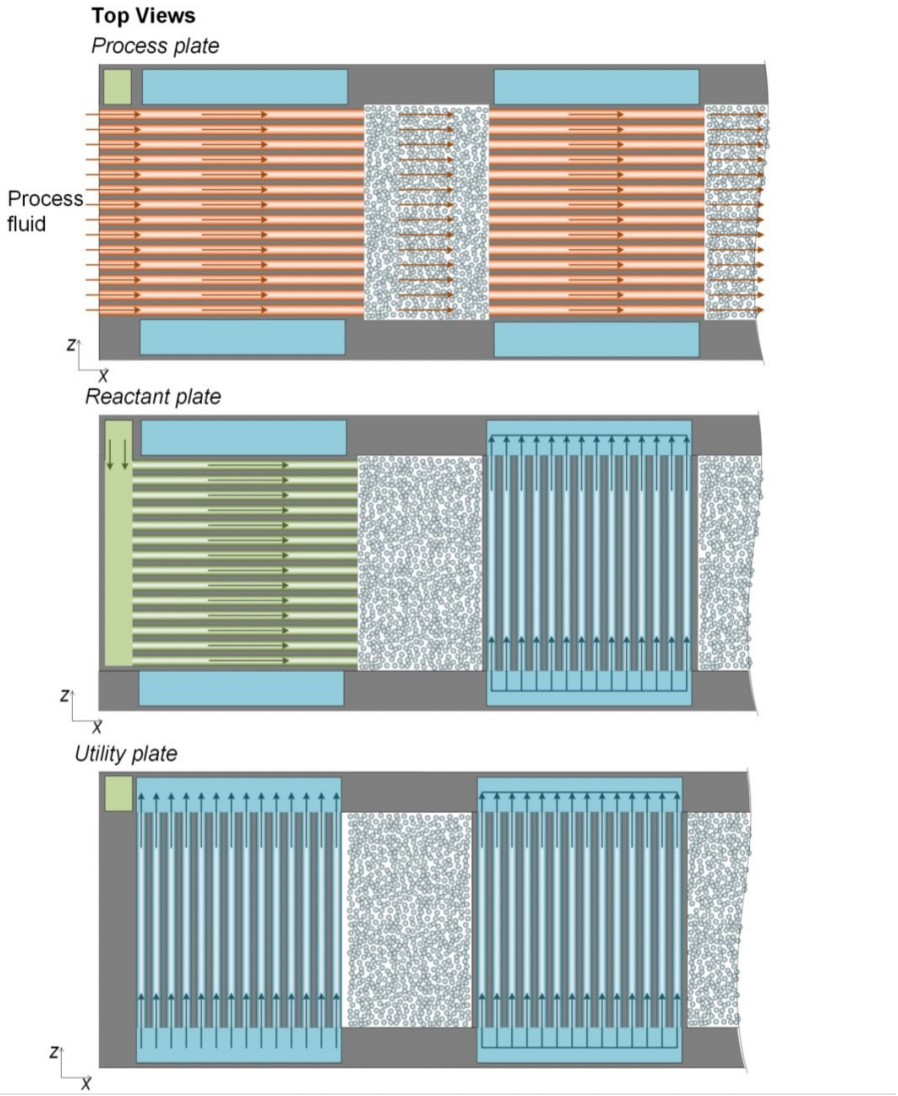

Figure 5-1: Top view of IHXR unit, where plates from top to bottom are (1) process fluid, (2) reactant fluid, and (3) utility fluid. [49]

The objective of the work is to determine the number and length of packed bed sections in the IHXR to maximize useful heat recovery while meeting the required CO_2 transportation pipeline specifications for PCLC flue gas. and to determine the subsequent PCHE heat exchanger lengths to facilitate useful heat recovery.

5.2. Process description

Flue gas exiting the PCLC unit first enters a direct contact cooler (DCC) where the flue gas is cooled to condense most of the water vapour content. Figure 5-2 shows the location of the IHXR relative to the PCLC unit.

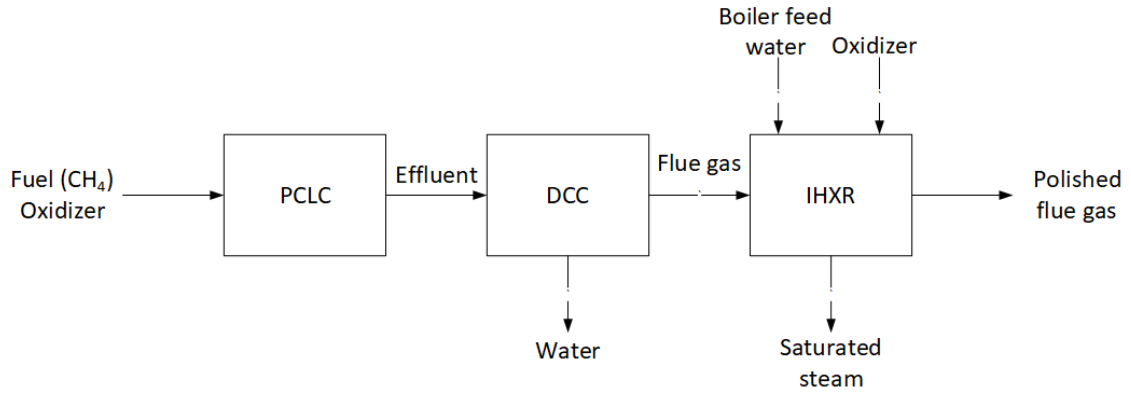

Figure 5-2: Block flow diagram of PCLC process and pathway to downstream CCUS

Following the DCC, flue gas first enters a pre-heating heat exchanger to be brought up to reaction conditions of T = 350 °C and P = 665 kPa. Figure 5-3 shows the layout of the IHXR without the pre-heating heat exchanger, where the process fluid is the PCLC flue gas ready for polishing, and the utility fluid is boiler feed water entering at T = 76 °C and leaving as saturated steam at T = 180 °C and P = 1000 kPa. The pre-heating heat exchanger is not part of this design study as its configuration may change depending on how the recovered heat from this process is allocated. Equal amounts of O_2 are injected into each packed bed section at the same conditions of the inlet process fluid.

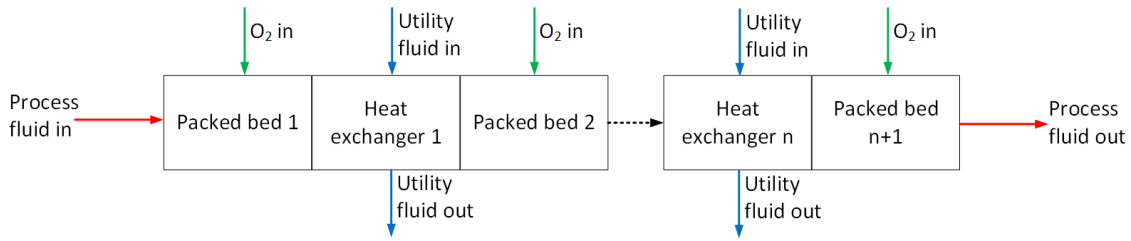

Figure 5-3: Simplified IHXR layout

The complete ACTL CO_2 pipeline specifications used as the guideline for the polished flue gas composition in this study a given in Table 5-1.

Table 5-1: ACTL pipeline specifications for CO_2 transportation. [4]

Species	Requirement (mol%)
Minimum CO_2	95
Maximum CH_4	1
Maximum CO	1
Maximum H_2	1
Maximum O_2	0.1
Maximum N_2	1
Maximum Hydrocarbons	2
Maximum Inert (N_2, Ar, CH_4)	4

5.3. Methodology

5.3.1. PCLC flue gas composition

The stream composition used for this study is for a 100 MW_{th} natural gas fired commercial-scale PCLC unit, amounting to a flue gas flow rate of 22,955 kg/h. The expected stream composition from the PCLC unit is given in Table 5-2 and denoted as the base case. The base case was then expanded into an "upper limit" case in which the CH_4 conversion in the PCLC unit is reduced from 98.5% to 97%, which raises the CH_4 removal requirement in the IHXR unit.

Table 5-2: Base case stream composition, 98.5% CH_4 conversion in PCLC (left); Upper limit stream composition, 97% CH_4 conversion in PCLC (right).

Species	Inlet Feed (kmol/h)
CH_4	6.16
CO_2	503.64
CO	7.29
H_2O	17.19
H_2	0.00
O_2	0.00
N_2	6.33

Species	Inlet Feed (kmol/h)
CH_4	12.32
CO_2	497.48
CO	7.29
H_2O	17.19
H_2	0.00
O_2	0.00
N_2	6.33

5.3.2. Gibbs equilibrium study

The desired pathway for flue gas polishing via the IHXR is through catalytic combustion, where the reaction exotherm is recovered as useful heat. As such, it is desired to combust as much CH_4 and CO as possible to maximize useful heat recovery. However, catalytic reaction mechanisms with similar species as the PCLC flue gas mainly concern hydrogen production via steam reforming or automotive exhaust emission control. For reforming reactions, both the hydrogen production and the associated endotherm are undesirable for the IHXR. For automotive exhaust control, it is atypical for reaction conditions with such high CO_2 concentration as well as elevated reaction pressure.

No adequate reaction kinetic systems were found for the desired scope after a thorough search, thus the analysis of the catalytic combustion process was divided into two parts. The first involves using the Gibbs equilibrium reactor from Aspen HYSYS to determine the number of packed bed sections required to bring the flue gas to the recommended pipeline specifications while maximizing useful heat recovery, the second involves using CO combustion kinetics in a plug flow reactor model to size the packed bed sections. Given that CO has a higher autoignition temperature than CH_4, it is reasonable to assume that CH_4 reacts with O_2 more readily than CO. [58] Therefore, final sizing of the packed bed sections in the IHXR is based on the length required to remove the CO content from the flue gas.

The Gibbs reactor model in Aspen HYSYS was used to determine the equilibrium conversion of the reacting system at each packed bed section, with the outlet of the final packed bed section to have removed as much CH_4 and CO as possible to maximize useful heat recovery. Reactors with multiple adiabatic packed beds typically operate at the highest

allowable temperatures to facilitate fast reaction rates, and the number of packed bed sections was determined based on a design constraint recommending limiting the temperature rise per adiabatic packed bed to 50 °C. [7] The maximum temperature rise was increased to 75°C per packed bed for the upper limit case to retain the same number of packed beds as the base case. The upper limit case is expected to be a temporary increase in CH_4 concentration caused by a process upset. Therefore, the IHXR will not undergo a complete redesign to accommodate the short period with increased operating temperature since the CH_4 concentration is expected to return to baseline afterwards.

Stagewise adiabatic combustion of CH_4 and CO enables precise temperature control to allow the reaction to occur at thermodynamically favourable conditions, and to mitigate catalyst deactivation [59]. Stoichiometric amounts of O_2 required for near complete removal of CH_4 and CO were evenly distributed and injected into each packed bed.

HYSYS heat exchangers were selected to simulate the interstage PCHEs where boiler feedwater was used as the utility fluid. Heat duty and the relevant properties of both process and utility fluid were obtained from the simulated unit operation.

5.3.3. Kinetic modelling study

Each bed in the multi-stage reactor was assumed to have the same length. The bed length was determined using the final packed bed inlet concentration derived from the equilibrium study because the last state has lowest concentration driving force. It is therefore reasonable to expect this stage to require the longest bed length. Consequently, the length estimate from the upper limit case was used to provide a conservative estimate, and this result was used across all packed bed sections for both cases. It is important to note that although the operating conditions are selected to provide a conservative estimate of the packed bed

length, the fast CO combustion kinetics may still underestimate its length as it does not take into account interactions of CO with other species in reactions such as water-gas shift and reverse steam reforming. Stoichiometric amounts of O_2 to remove the remaining CO in the final packed bed section was used. CO combustion kinetics for a 0.154 wt% Pd catalyst supported on 20% CeO_2 and 80% Al_2O_3 obtained from Yao et al. was used [24]. The rate equation (Eq. 5.1) is written as follows:

$$R = kP_{O_2}^{m}P_{CO}^{n} \tag{5.1}$$

where k represents the reaction rate constant, P_{O_2} and P_{CO} are the partial pressures of O_2 and CO, and superscripts m and n are the reaction orders of O_2 and CO. The reaction rate constant is of Arrhenius type and can be calculated by Eq. 5.2.

$$k = A' \cdot e^{\frac{-E_a}{RT}} \tag{5.2}$$

The kinetics were modified to a 50 μm thick active catalytic wash coat diluted to 0.01% of the original catalyst concentration to create a catalyst pellet 3 mm in diameter to both reduce the diffusion distance and to adjust to the increased reaction pressure and CO concentration in the IHXR. The pre-exponential factor was thus adjusted to reflect the presence of a wash coat using Eq. 5.3, and Table 5-3 lists the relevant packed bed plug flow simulation parameters.

$$A' = \frac{V_{coat}}{V_{particle}} \cdot A \tag{5.3}$$

Table 5-3: Process simulation parameters and kinetic parameters for packed bed sizing. [24]

Flue gas flow rate	22,955 kg/h
Reaction temperature/pressure	350°C/665 kPa
Pressure loss in reactors	5 kPa
Reactor hydraulic diameter	0.72 m
Properties of $Pd/CeO_2/Al_2O_3$ catalyst	
Particle density	4643 kg_{cat}/m^3_{cat}
Particle diameter	0.003 m
Bed void fraction	0.55
Activation energy	62,760 kJ/kmol
Pre-exponential factor	3.14E07 kmol CO_2/m^3_{cat} • s • bar^2
m	0.6
n	0.7

5.3.4. PCHE design study

This section provides the approach to determine the required heat exchanger lengths for both the base and upper limit case studies. Each exchanger section follows the same structure as shown in Figure 5-1. Equal distribution of O_2 in the packed bed sections ensures low heat duty variance across all heat exchangers, therefore, it is sufficient to size one exchanger section and apply that sizing for all sections of the IHXR.

5.3.4.1. Determination of convective heat transfer coefficients

The thermal circuit method was used to size the heat exchanger sections. All gas streams are composed of at least 95 mol% CO_2 and thus the thermodynamic properties of pure CO_2 at the desired conditions were used as an estimate of the properties of the overall gas stream. Gnielinski's correlation (Eq. 5.4) for forced internal turbulent flow was used to calculate the gas-side Nusselt number:

$$Nu_D = \frac{\left(\frac{f}{8}\right) \cdot (Re_D - 1000) \cdot Pr}{1 + 12.7\left(\frac{f}{8}\right)^{\frac{1}{2}} \cdot \left(Pr^{\frac{2}{3}} - 1\right)} \tag{5.4}$$

where f is the Darcy friction factor calculated by Eq. 5.5.

$$f = (0.79\, ln(Re_D) - 1.64)^{-2} \tag{5.5}$$

The gas-side convective heat transfer coefficient (h) was then calculated from the Nusselt number (Eq. 5.6).

$$Nu_D = \frac{h \cdot D_h}{k} \tag{5.6}$$

The boiling-side convective heat transfer was estimated to be magnitudes greater than that of the gas side, and thus the boiling side heat transfer resistance is considered negligible. Therefore, the heat exchanger design only considered conduction through the walls and gas-side convection in the calculation of the overall heat transfer coefficient of the thermal circuit. [60]

5.3.4.2. Thermal circuit design

Figure 5-4 shows the make up of one repeating PCHE unit with one flow channel and the relevant dimensions. The dimensions are based on calculations regarding the mechanical design of PCHEs presented in a white paper from the PCHE manufacturer Heatric. [61] For this study, both the dimensions of the complete PCHE in the y-direction and z-direction were fixed, in which their values were dependent on the number of repeating units, number of process channels, channel diameter, and channel thickness

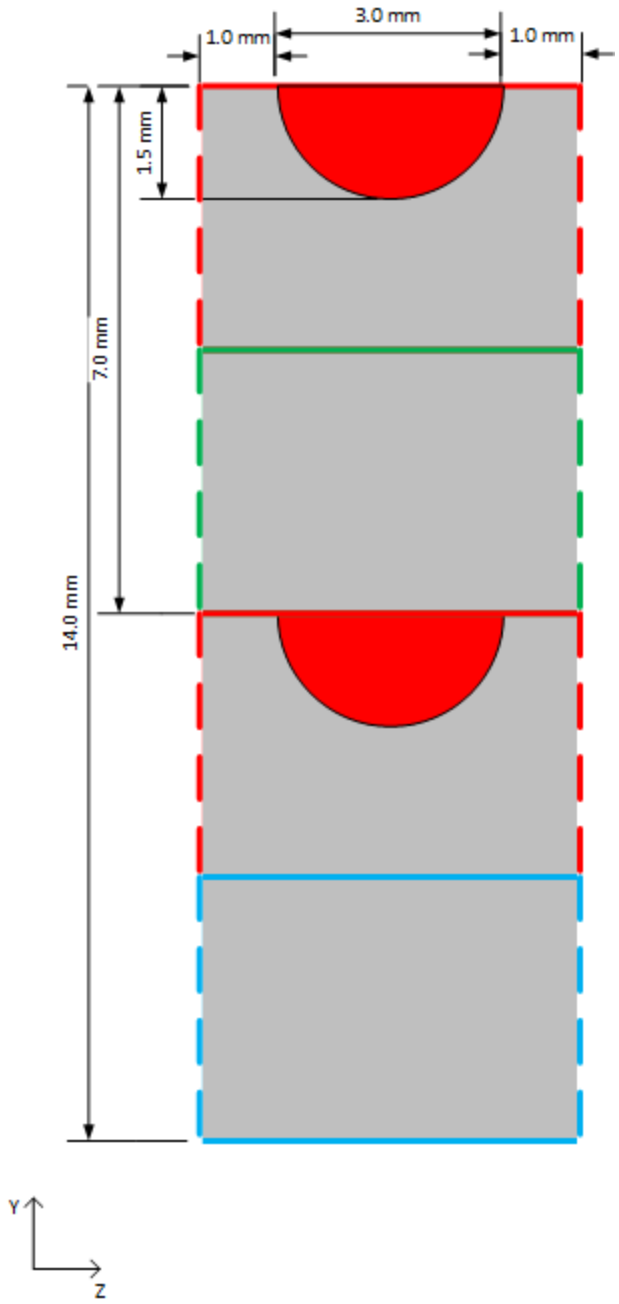

Figure 5-4: Front view of the repeating PCHE unit: red, process plate; green, reactant plate; and blue, utility plate. [49]

This study uses a PCHE design consisting of 52 repeating units and 90 side-by-side process channels corresponding to a height and width of 0.91 m and 0.45 m, respectively. To determine each of the interstage PCHE lengths in the x-direction after each reaction section,

the convective resistance (Eq. 5.7–5.8) from the process fluid and conduction resistance at the process plate interface was calculated:

$$R_{conv,1} = \frac{1}{h \cdot \left(\frac{\pi D}{2} \cdot L\right) \cdot \#\ channels} \tag{5.7}$$

$$R_{conv,2} = \frac{1}{h \cdot (D \cdot L) \cdot \#\ channels} \tag{5.8}$$

Eq. 5.7 is used to account for the semi-circular channel contact area, whilst Eq. 5.8 accounts for the flat region below the base of the plate as the contact area. Eq. 5.9 describes the conduction resistance (R_{cond}) calculation.

$$R_{cond} = \frac{t}{k \cdot \left(\frac{\frac{\pi D}{2} \cdot L + D \cdot L}{2}\right) \cdot \#\ channels} \tag{5.9}$$

where k is the thermal conductivity taken at $16.3\ W/m \cdot k$ for 316 stainless steel at around 340 °C [62]. With both resistances calculated, the product of the overall heat transfer coefficient and required heat transfer surface area was then calculated via Eq. 5.10.

$$UA = \frac{1}{2 \times R_{cond} + R_{conv,1} + R_{conv,2}} \tag{5.10}$$

The log-mean temperature difference (LMTD) was then calculated by Eq. 5.11:

$$\Delta T_{lm} = \frac{(T_{hot,in} - T_{cold,out}) - (T_{hot,out} - T_{cold,in})}{ln\left(\frac{T_{hot,in} - T_{cold,out}}{T_{hot,out} - T_{cold,in}}\right)} \tag{5.11}$$

The LMTD correction factor for cross-flow was estimated using Figure 5-5, where R is the temperature ratio between the process and utility fluid, and P is the effectiveness parameter. For this study, the correction factor F is 0.97–0.99.

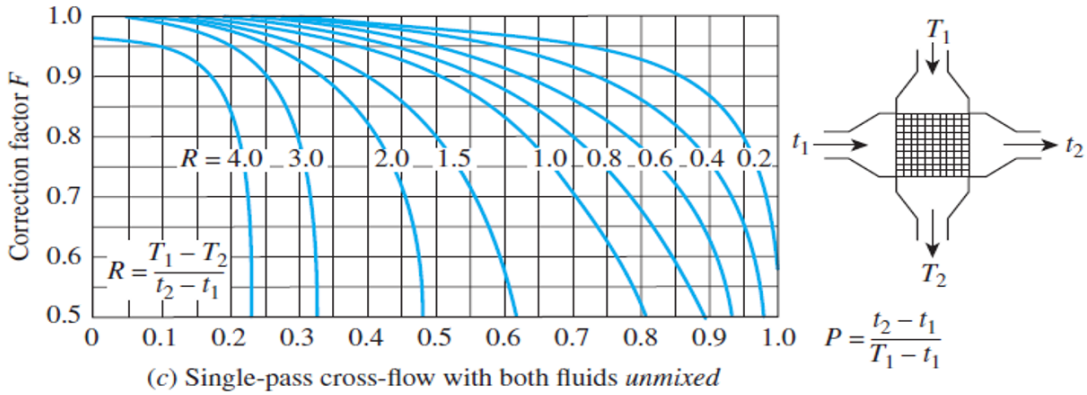

Figure 5-5: LMTD correction factor for unmixed cross-flow flow pattern. [63]

Lastly, the heat transfer rate is calculated using Eq. 5.12:

$$Q = UAF\Delta T_{lm} \tag{5.12}$$

The heat exchanger length L, which is embedded in the UA calculation, was varied until the calculated heat duty Q matches the simulation by Aspen HYSYS in the Gibbs equilibrium study.

5.4. Results and discussion

5.4.1. Outlet composition and number of packed beds

Carrying out the equilibrium modelling study described in section 5.3.2, it was determined that six bed sections are required for the base and upper limit cases to combust nearly all CH_4 and CO whilst adhering to their respective 50°C and 75°C temperature rise constraint. Table 5-4 shows the equilibrium outlet conditions for each reactor from the base case stream composition. Equal amount of O_2 is supplied to all packed beds to simplify the process control strategy. The sum of all injected O_2 results in stoichiometric combustion of both CH_4 and CO. It is noteworthy that the CH_4 and CO content reaches acceptable levels for pipeline transport after the first reactor, but further removal was carried out for maximum useful heat recovery culminating in the final six bed design.

Table 5-4: Species equilibrium concentrations at each reactor outlet in base case study.

Composition Dry Basis (%)	Reactor 1	Reactor 2	Reactor 3	Reactor 4	Reactor 5	Reactor 6
CH_4	0.95	0.74	0.51	0.29	0.09	0.00
CO_2	96.52	96.80	97.08	97.39	97.89	98.79
CO	0.86	0.72	0.61	0.51	0.37	0.00
H_2	0.39	0.38	0.37	0.34	0.27	0.00
O_2	0.00	0.00	0.00	0.00	0.00	0.00
N_2	1.20	1.20	1.20	1.20	1.20	1.21
Additional Info						
O_2 injection rate (kmol/h)	2.66	2.66	2.66	2.66	2.66	2.66
Outlet T (°C)	397.1	394.1	393.3	393.3	394.0	399.7

Table 5-5 shows the equilibrium outlet conditions for each reactor from the upper limit case stream composition. The upper limit case reaches pipeline specifications after four packed bed sections, and like the base case, effectively all CH_4 and CO is removed by the sixth reactor outlet.

Table 5-5: Species equilibrium concentrations at each reactor outlet in upper limit case study.

Composition - Dry Basis (%)	Reactor 1	Reactor 2	Reactor 3	Reactor 4	Reactor 5	Reactor 6
CH_4	1.72	1.27	0.87	0.48	0.14	0.00
CO_2	95.09	95.53	96.09	96.71	97.45	98.80
CO	1.39	1.34	1.18	0.98	0.70	0.00
H_2	0.61	0.67	0.68	0.64	0.51	0.00
O_2	0.00	0.00	0.00	0.00	0.00	0.00
N_2	1.19	1.19	1.19	1.19	1.19	1.20
Additional Info						
O_2 injection rate (kmol/h)	4.71	4.71	4.71	4.71	4.71	4.71
Outlet T (°C)	417.0	422.9	424.7	425.4	426.9	437.0

The outlet N_2 content was found to be above the 1 mol% recommended from the ACTL pipeline specifications, which is due to air slippage within the PCLC unit. However, as other inert gases such as CH_4 are removed, the total inert content is well below the recommended concentration of 4 mol%. Note that small amounts of hydrogen gas is created within the reactor from the water-gas shift reaction, which is then consumed by before the exit.

5.4.2. Required packed bed section length

A packed bed section length of 0.06 m was calculated to produce the desired extent of reaction for both the base and upper limit cases. This length ensures nearly complete CH_4 and CO oxidation by estimating the required length for complete CO combustion, matching equilibrium species fractions predicted by the Gibbs reactors. Table 5-6 shows the inlet and outlet CO concentrations and the required amount of O_2 for its stoichiometric combustion for the final packed bed section in the base and upper limit cases, as well as the simulated pressure drop per packed bed..

Table 5-6: PFR model kinetic study results for the last packed bed section.

Gibbs reactor inlet conditions	**Length (m)**	**O_2 injection (kmol/h)**	**Inlet CO (kmol/h)**	**Outlet CO (kmol/h)**	**Pressure drop (kPa)**
Base case	0.06	0.98	1.96	0.00	7.11
Upper limit case	0.06	1.87	3.73	0.00	7.62

5.4.3. Required heat exchanger section length

The designed PCHE lengths and temperature conditions for both the base and upper limit case stream compositions are given in Table 5-7. The required PCHE section lengths to reduce temperature by approximately 50°C for the base case and 75°C for the upper limit

case were 0.19 m and 0.265 m, respectively. Furthermore, the hydrodynamic entrance length for both exchanger sections was determined to be 0.025 m, or approximately 13% of the base case exchanger length and 10% of the upper limit case exchanger length. This value implies that in both scenarios the gas flow field fully develops early in the exchanger, which is an important factor as the applied convective heat transfer correlation assumes fully developed flow.

Table 5-7: PCHE results for base case and upper limit HEX case studies.

CH_4 Conversion	Exchanger Length (m)	Entrance Length(m)	Inlet Gas Temperature (℃)	Outlet Gas Temperature (℃)
98.5	0.19	0.025	397	350.0
97	0.265	0.025	427	350.0

The heat exchanger designs are to accommodate for the largest temperature change within the IHXR and will be adopted for all heat exchanger sections to account for any potential increase in reaction exotherm due to a change in CH_4/CO concentration.

5.4.4. Final IHXR design

Combining the results from sections 5.4.2 and 5.4.3, the final IHXR design is illustrated by Figure 5-6. The dimensions from the upper limit case are ultimately adopted for a conservative design estimate of the required heat exchanger lengths. As gas phase heat transfer is rate limiting, the additional heat transfer area from the longer heat exchanger sections can help accommodate for process changes resulting in abnormally high amounts of CH_4 and CO. Different exotherms produced from different flue gas inlet compositions can be addressed by changing the inlet pressure of the boiler feed water to adjust the heat exchange capacity.

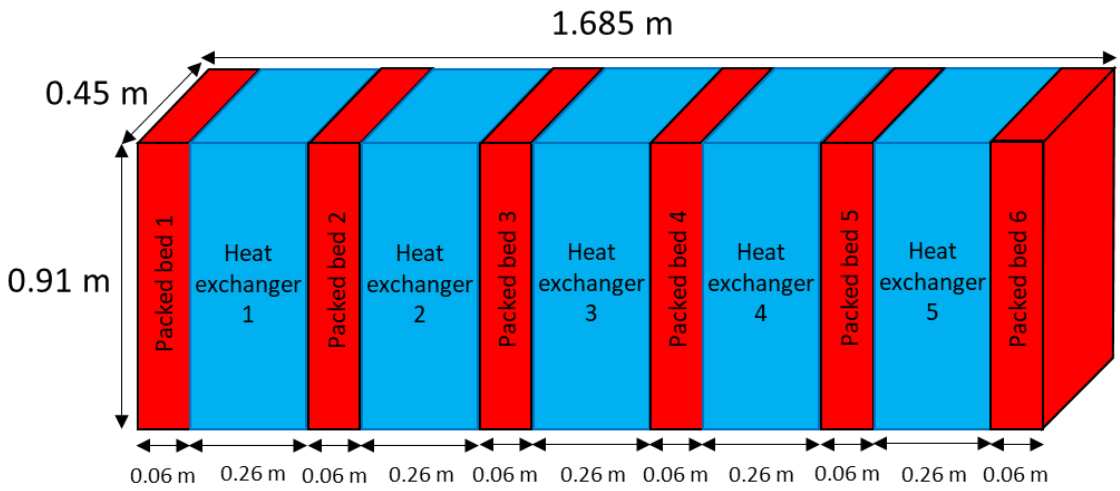

Figure 5-6: Final design configuration and dimensions of the IHXR unit.

Operating at base compositions with flue gas flow rate of 22,955 kg/h, approximately 1.6 MW of heat can be recovered as saturated steam at 180 °C and 1001 kPa at a flow rate of approximately 3835 kg/h. This saturated steam is of the same quality and condition as generated from the PCLC process, which could be combined to serve as additional industrial heating or can be utilized for pre-heating the initial packed bed section or the various O_2 fuel streams. Although the recovered heat is small compared to the 100 MW PCLC, purification of the flue gas is required, and this technology can improve efficiency while purifying the flue gas stream.

5.5. Conclusion

A preliminary design of an IHXR for polishing PCLC flue gas prior to CCUS was developed. Process simulations via Aspen HYSYS were used to first determine the gas phase composition exiting each packed bed section of the IHXR and then to size both the packed bed and heat exchanger sections. The equilibrium, kinetic, and thermal analyses provide a scalable framework for designing PCLC flue gas polishing systems.

The final IHXR is made up of six packed bed sections and five heat exchanger sections. Each packed bed section is 0.06 m in length and each heat exchanger section 0.265 m in length. The overall dimensions of the IHXR are 1.66 m × 0.91 m × 0.45 m in length, height, and width. The resulting IHXR design was able to recover approximately 1.6 MW of heat (approximately 2.3 MW/m³ IHXR) in the form of saturated steam at 180°C and 1001 kPa at a flow rate of approximately 3835 kg/h. The recovered heat amounts to approximately 1.6% of the fuel input of the PCLC process. These dimensions correspond to the upper limit case, with a higher-than-expected inlet CH_4 concentration coming from the PCLC unit, to allow for a conservative heat exchanger design for removing potential unexpected exotherms.

The limiting factor regarding the applicability of the study is the choice of reaction kinetics. The packed bed design relies on using a CO combustion reaction kinetic meant for automotive exhaust, which does not have the same operating condition nor the CO concentration as PCLC flue gas. Specific catalysts fit for CH_4 and CO removal from PCLC flue gas need to be developed to ensure that the design is accurate and the polished flue gas can meet the ACTL pipeline specifications.

6. Conclusions and future work

6.1. Conclusions

This work explores the use of process intensified heat exchanger reactors known as IHXRs for combustion flue gas polishing. The IHXRs are designed and characterized with the aid of reduced order modelling. Two types of flue gases were discussed, one from oxy-fuel combustion where the contaminant of interest for removal is the residual O_2 and the other from PCLC where the contaminant of interest is residual CH_4 and CO from partial combustion. To aid with the design and characterization of the proposed IHXRs, a 1-D ROM for reactor modelling was formulated and validated, and a 2-D ROM for heat exchanger modelling was validated against both 3-D modelling results for its conduction shape factor assumption as well as experimental results for its transient modelling capabilities.

The 1-D ROM was formulated for use in modelling oxy-fuel combustion flue gas polishing, with its validation through comparison against an OpenFOAM reaction solver package. The results corroborated well between that of the 1-D ROM and OpenFOAM, validating the capabilities of the ROM. Through a combination of the 1-D ROM for reactor section modelling and a thermal circuit approach for modelling the heat exchanger sections of the IHXR, several proposed designs of IHXRs varying the number of reactor sections were characterized in which the design with the best efficiency defined as having the least volume was chosen. The final design was an IHXR consisting of 5 reactor sections where the reaction temperature rise within each section was held at the maximum allowable temperature of 50°C. The final design was capable of processing flue gas at a rate of 12.3 kg/s m^3 IHXR with the final O_2 concentration reduced to within 0.007 wt% (100 PPMv).

One of the assumptions taken during the process of formulating the 2-D ROM for heat exchanger modelling was to use a conduction shape factor of unity for conduction in the through plate and transverse directions. The assumption was tested through a combination of physical experiments and 3-D modelling within OpenFOAM for heat flux calculation to confirm its validity. A micro-channel cross-flow heat exchanger plate was manufactured with the 2-D ROM configured to match the physical layout and properties of the manufactured plate. Results from the experiments were collected and formulated into a Nusselt number correlation for use in the 2-D ROM, in which the generated temperature profiles were compared with those collected during experiments to validate implementation. The shape factor assumption was then validated through a 3-D OpenFOAM model, in which the surface temperatures were generated from 2-D ROM using the experimentally obtained Nusselt number correlation. Heat fluxes between the curved flow channels of the heat exchanger plate were calculated from the 3-D model and then compared to the values without the presence of flow channels. The result yielded shape factors 84.1% and 96.4% of unity in the through plate and transverse directions, where a shape factor unity indicates a lack of flow channels.

The 2-D ROM was validated for its transient modelling capabilities through comparison with the temperature time series data collected from the experiments. Various IHXR designs ranging from 5 – 45 cross-flow channels were proposed and simulated using the 2-D ROM fitted with the Dittus-Boelter convective fluid-wall heat transfer correlation along with a reduced order reactor model for the time constants in the heat exchanger and reactor sections. The process model of each design can then be formulated with the time constants of each section. The ability of each IHXR to reject disturbances in the inlet fluid

temperature can then be determined through a Bode plot based on the process models of each design. The results showed that the IHXR designs are generally stable, with stability increasing along with the number of flow channels. This approach can be made more accurate by fitting in more specific convective heat transfer correlations for the relevant geometry, extending its application.

The use of the IHXR was extended for PCLC flue gas polishing through process simulation in Aspen HYSYS to fit ACTL pipeline transport specifications. The flue gas compositions were taken from an existing PCLC facility generating industrial heat, with the desired pathway for eliminating the contaminants of concern being through catalytic combustion. Boiler feed water was used as utility fluid for cooling effluents from the reactor sections, where it exits as saturated steam at 180 °C for heat recovery. Due to a specific lack of resources on catalytic combustion kinetics for CH_4 and CO with O_2 as oxidizer in a primarily CO_2 environment, equilibrium reactors were used in junction with plug flow reactors to determine the species make up of the outlet gases. An assumption was made to use CO combustion kinetics for sizing the reactor sections based on CH_4 having a lower autoignition temperature than CO for a conservative estimate of the reactor sizing. The heat exchanger section was subsequently sized via a thermal circuit approach with the required heat exchanger duty obtained from HYSYS. The IHXR designed via process simulation was found capable of processing flue gas at a rate of 22,955 kg/h (33,768 kg/h/m^3 IHXR) while recovering heat at a rate of 1.6 MW (2.35 MW/m^3 IHXR). However, a more appropriate set of catalytic reaction kinetics should be obtained and applied for a more accurate design and heat recovery calculation.

6.2. Future work

One of the major shortcomings in the IHXR design through process simulation was the lack of relevant reaction kinetics, resulting in approximations made using a combination of the HYSYS equilibrium reactor for species concentration, and CO combustion kinetics in the context of automotive exhaust control for sizing. The natural next step would be to characterize combustion catalysts capable of reacting CH_4 and CO with O_2 in a largely CO_2 environment. A more accurate IHXR can be designed given a more appropriate set of reaction kinetics.

The current sensitivity analysis for PCLC flue gas polishing only involves an increase in CH_4 due to unexpected reduction in combustion within the PCLC unit, the potential scenario of a reduction in oxidizer resulting in increased partial combustion and a higher CO concentration in the flue gas is not considered. Given a more appropriate catalyst for CH_4 and CO combustion, it is worthwhile to investigate an increase in CO concentration and the implications on both IHXR design as well as catalyst activity.

This work was only able to investigate the ability of the IHXR designs to reject disturbances in inlet temperature. The current proposed designs were unable for the controllers to properly reject disturbances in inlet flow rate during simulation. A proposed design change introducing a buffer vessel before the IHXR should allow the proper flow rate disturbance rejection.

Nomenclature

Symbols

A	Heat transfer area [m^2]
A_c	Cross-section area of flow channel [m^2]
a_c	Specific surface area of the particle [m^2/m^3]
c_p	Specific heat [J/kg·K]
C	Polynomial coefficient to convert FBG wavelength to temperature [-]
D	Mass diffusivity [m^2/s] / Flow channel diameter [m]
D_{eff}	Axial dispersion coefficient [m^2/s]
D_h	Hydraulic diameter [m]
d_{sv}	Sauter mean diameter of the particle [m]
f	Friction factor (-)
G	Mass flux [kg/m^2]
H	Enthalpy [kJ/kg]
h	Convective heat transfer coefficient [$W/m^2 \cdot K$]
i	Imaginary number
K_C	Proportional constant
K_P	Steady-state process gain
k	Thermal conductivity [W/m·K]
k_m	Mass transfer coefficient [m/s]
L	Characteristic length [m] / Characteristic length [m]
$\dot{m}$	Mass flow rate [kg/s]
Nu	Nusselt number [-]
P	Pressure [Pa]
Pr	Prandtl number [-]
$\dot{Q}$	Heat transfer rate [W]
q_R	Heat of reaction [W/m^3]
R	Rate of reaction [kg/m^3s] / Thermal resistance [K/W]
Re	Reynolds number [-]
Re_D	Reynolds number in the flow channel [-]
Re_p	Reynolds number in the packed bed [-]
S	Shape factor (m)
Sc	Schmidt number [-]
Sh	Sherwood number in packed bed [-]
t	Time [s] / IHXR plate thickness [m]
u	Velocity [m/s]
x	Direction [-]
Y	Mass fraction [-]
y	Direction (-)
z	Direction (-)

Greek Letters

Δ	Difference (-)

ϵ	Bed void fraction [-]
λ	Wavelength [m] / Closed-loop response time [s]
θ	Dead time [s]
μ	Dynamic viscosity [Pa·s]
ρ	Density (kg/m^3)
τ	Time constant (s)
ω	Frequency

Subscripts

bed	Packed bed section
baseline	Reference
C	Controller
cond	Conduction heat transfer
D	Disturbance
g	Gas
HE	Heat exchanger section
I	Integral
in	Inlet
measured	Experimentally measured
out	Outlet
P	Process
s	Solid

Abbreviations

CFD	Computational fluid dynamics
FBG	Fibre Bragg Grating
FOAM	Field operation and manipulation
IHXR	Integrated heat exchange reactor
PID	Proportional-integral-derivative
PCHE	Printed circuit heat exchanger
ROM	Reduced order model
RTD	Resistance temperature detector

References

[1] D. Y. Leung, G. Caramanna and M. M. Maroto-Valer, "An overview of current status of carbon dioxide capture and storage technologies," *Renewable and sustainable energy reviews,* vol. 39, pp. 426-443, 2014.

[2] H. Yang, Z. Xu, M. Fan, R. Gupta, R. B. Slimane, A. E. Bland and I. Wright, "Progress in carbon dioxide separation and capture: A review," *Journal of Environmental Sciences,* vol. 20, pp. 14-27, 2008.

[3] E. de Visser and C. Hendriks, "DYNAMIS CO2 quality recommendations," DYNAMIS Consortium, 2007.

[4] Enhance Energy Inc. and North West Redwater Partnership, "Alberta Carbon Trunk line Summary report for 2014," Government of Alberta, 2014, 2014.

[5] L. Zheng, Oxy-fuel combustion for power generation and carbon dioxide (CO2) capture, Philadelphia, PA: Woodhead Pub., 2011.

[6] J. Hetland, "Flue gas processing: Strategies for water management. Water removal and moisture control via dew point modelling," in *ieaghg*, Ponferrada, Spain, 2013.

[7] C. Huang, W. Cai, Y. Wang, Y. Liu, Q. Li and B. Li, "Review on the characteristics of flow and heat transfer in printed circuit heat exchangers," *Applied Thermal Engineering,* vol. 153, pp. 190-205, 2019.

[8] M. Fitzsimmons, D. M. Heim, W. W. Follett IV, S. Jovanovic, M. Byron, R. W. Hughes, D. J. McCalden and S. Champagne, "Final Report Project: Advanced Oxy-Combustion Technology Development and Scale Up for New and Existing Coal-Fired Power Plants (Phanse II)," GTI, Des Plaines, Illinois, 2018.

[9] M. Fitzsimmons, D. M. Heim, W. W. Follet IV, S. Jovanovic, M. Byron, R. W. Hughes, D. J. McCalden and S. Champagne, "Enabling Technologies for Oxy-fired Pressurized Fluidized Bed Combustor Systems," 2019.

[10] B. S. Haynes and A. M. Johnston, "Process design and performance of a microstructured convective steam-methane reformer," *Catal. Today,* pp. 34-41, 2011.

[11] J. A. Banister and S. O. Rumbold, "A compact gas-to-methanol process and its application to improved oil recovery," in *Gas processors Association Europe Annual Conference*, Warsaw, 2005.

[12] M. B. Toftegaard, J. Brix, P. A. Jensen, P. Glarborg and A. D. Jensen, "Oxy-fuel combustion of solid fuels," *Progress in Energy and Combustion Science,* vol. 36, pp. 581-625, 2010.

[13] J. Adanez, A. Abad, F. Garcia-Labiano, P. Gayan and L. F. de Diego, "Progress in Chemical-Looping Combustion and Reforming technologies," *Progress in Energy and Combustion Science,* vol. 38, pp. 215-282, 2012.

[14] A. Meshram, A. K. Jaiswal, S. D. Khivsara, J. D. Ortega, C. Ho, R. Bapat and P. Dutta, "Modeling and analysis of a printed circuit heat exchanger for supercritical CO2 power cycle applications," *Applied Thermal Engineering,* vol. 109, pp. 861-870, 2016.

[15] H. Liu, M. Liu, S. Liu, Y. Tang, R. Liu, J. Fei, Y. Zan, R. Zheng and Y. Huang, "Prediction of supercritical CO2 flow and heat transfer behaviors in zigzag-type

printed circuit heat exchangers by improved POD-GABP reduced order model," *Applied Thermal Engineering,* vol. 267, 2025.

[16] W.-x. Chu, X.-h. Li, T. Ma, Y.-t. Chen and Q.-w. Wang, "Experimental investigation on SCO2-water heat transfer characteristics," *International Journal of Heat and Mass Transfer in a printed circuit heat exchanger with straight channels,* vol. 113, pp. 184-194, 2017.

[17] T. H. Kim, J. G. Kwon, S. H. Yoon, H. S. Park, M. H. Kim and J. E. Cha, "Numerical analysis of air-foil shaped fin performance in printed circuit heat exchanger in a supercritical carbon dioxide power cycle," *Nuclear Engineering and Design,* vol. 288, pp. 110-118, 2015.

[18] J. H. Park, J. G. Kwon, T. H. Kim, M. H. Kim, J.-E. Cha and H. Jo, "Experimental study of a straight channel printed circuit heat exchanger on supercritical CO2 near the critical point with water cooling," *International Journal of Heat and Mass Transfer,* vol. 150, 2020.

[19] A. J. Furlong, H. Ge, R. W. Hughes, A. Macchi and J. B. Haelssig, "Dynamic modelling of cross-flow printed circuit heat exchangers for multistage reactor intercooling," *Applied Thermal Engineering,* vol. 239, 2024.

[20] S. J. Mihailov, D. Grobnic, C. Hnatovsky, R. B. Walker, P. Lu, D. Coulas and H. Ding, "Extreme Environment Sensing Using Femtosecond Laser-Inscribed Fiber Bragg Gratings," *Sensors,* vol. 17, 2017.

[21] A. Bejan and A. D. Kraus, Heat transfer handbook, Hoboken, New Jersey: John Wiley & Sons, Inc., 2003.

[22] J. Holladay, J. Hu and K. Y. Wang, "An overview of hydrogen production technologies," *Catalysis Today,* vol. 139, pp. 244-260, 2009.

[23] Y.-F. Y. Yao, "The oxidation of CO and hydrocarbons over noble metal catalysts," *Journal of Catalysis,* vol. 87, no. 1, pp. 152-162, 1984.

[24] Y. Zhang, Y. Xie, Y. Zhu, X. Lu and X. Ji, "Energy consumption analysis for CO2 separation from gas mixtures with liquid absorbents," *Energy Procedia,* vol. 61, p. 2695－2698, 2014.

[25] Linde Engineering, "Hydrogen," Linde Engineering, 2018. [Online]. Available: https://assets.linde.com/-/media/global/engineering/engineering/home/products-and-services/process-plants/h2_1_1_e_12_150dpi_nb.pdf. [Accessed 02 01 2018].

[26] R. Turton and J. A. Shaeiwitz, Chemical Process Equipment Design, Boston, MA: Prentice Hall, 2017.

[27] Z. Anxionnaz, M. Cabassud, C. Gourdon and P. Tochon, "Heat exchanger/reactors (HEX reactors): Concepts, technologies: State-of-the-art," *Chem. Eng. Process.,* vol. 47, no. 12, pp. 2029-2050, 2008.

[28] Heatric, "Heat Exchangers for Chemical Processing Industries," [Online]. Available: https://www.heatric.com/heat-exchangers/industry-applications/chemical-processing-industry/. [Accessed 07 03 2023].

[29] Heatric, "Characteristics of Diffusion-Bonded Heat Exchangers," Heatric, 2021. [Online]. Available: https://www.heatric.com/heat-exchangers/features/characteristics/. [Accessed 01 11 2021].

[30] S. Chung, S. W. Lee, N. Kim, S. M. Shin, M. H. Kim and H. Jo, "Experimental study of printed-circuit heat exchangers with airfoil and straight channels for optimized recuperators in nitrogen Brayton cycle," *Applied Thermal Engineering,* vol. 218, 2023.

[31] Y. Wang and G. Xie, "4E multi-objective optimization of cold electricity co-generation system based on supercritical CO2 Brayton cycle," *Energy Conversion and Management,* vol. 283, 2023.

[32] C. W. Shin and H. C. No, "Experimental study for pressure drop and flow instability of two-phase flow in the PCHE-type steam generator for SMRs," *Nuclear Engineering and Design,* vol. 318, pp. 109-118, 2017.

[33] H. Zhang, L. Shi, W. Xuan, T. Chen, Y. Li, H. Tian and G. Shu, "Analysis of printed circuit heat exchanger (PCHE) potential in exhaust waste heat recovery," *Applied Thermal Engineering,* vol. 204, 2022.

[34] G. Goodwin, R. L. Speth, H. K. Moffatand and B. W. Weber, "Cantera: An Object-oriented Software Toolkit for Chemical Kinetics, Thermodynamics, and Transport Processes," https://www.cantera.org, 2021.

[35] O. Levenspiel, Chemical Reacting Engineering, New York: John Wiley & Sons, 1999.

[36] D. Gunn, "Transfer of heat or mass to particles in fixed and fluidised beds," *Int. J. Heat Mass Transf.,* vol. 21, no. 4, pp. 467-476, 1978.

[37] S. Nasr, N. Semagina and R. E. Hayes, "Kinetic Modelling of Co3O4- and Pd/Co3O4-Catalyzed Wet Lean Methane Combustion," *Emiss. Control. Sci. Technol.,* no. 6, pp. 269-278, 2020.

[38] J. Shen, R. E. Hayes and N. Semagina, "On the contribution of oxygen from Co3O4 to the Pd-catalyzed methane combustion," *Catal. Today,* vol. 360, pp. 435-443, 2021.

[39] The OpenFOAM Foundation, "OpenFOAM | Free CFD Software | The OpenFOAM Foundation," The OpenFOAM Foundation, [Online]. Available: https://openfoam.org/. [Accessed 01 October 2023].

[40] T. L. Bergman, A. S. Lavine, F. P. Incropera and D. P. Dewitt, Fundamentals of Heat and Mass Transfer, Hoboken: John Wiley & Sons, 2011.

[41] V. Gnielinski, "Neue Gleichungen für den Wärme- und den Stoffübergang in turbulent durchströmten Rohren und Kanälen," *Engineering Research,* vol. 41, no. 1, pp. 8-16, 1975.

[42] R. T. Symonds, R. W. Hughes, D. Y. Lu, P. Navarri and O. Ashrafi, "Systems analysis of pressurized chemical looping combustion for SAGD," *International Journal of Greenhouse Gas Cont,* vol. 73, pp. 111-123, 2018.

[43] T. Mattisson, M. Johansson and A. Lyngfelt, "The use of NiO as an oxygen carrier in chemical-looping combustion," *Fuel,* vol. 85, no. 5-6, pp. 736-747, 2006.

[44] P. A. Brownsort, "Briefing on carbon dioxide specifications for transport," EU CCUS PROJECTS NETWORK, Brussels, Belgium, 2019.

[45] A. Aspelund and K. Jordal, "Gas conditioning—The interface between CO2 capture and transport," *International Journal of Greenhouse Gas Control,* vol. 1, no. 3, pp. 343-354, 2007.

[46] K. Goto, S. Kazama, A. Furukawa, M. Serizawa, S. Aramaki and K. Shoji, "Effect of CO2 Purity on Energy Requirement of CO2 Capture Processes," *Energy Procedia,* vol. 37, pp. 806-812, 2013.

[47] A. M. Johnston, W. Levy and S. O. Rumbold, "Application of Printed Circuit Heat Exchanger Technology within Heterogeneous Catalytic Reactors," November 2001. [Online]. Available: https://www.parker.com/content/dam/Parker-com/Literature/heatric-division/whitepapers/Applications-of-PCHE-technology-in-heterogeneous-catalytic-reactors.pdf. [Accessed 30 October 2024].

[48] E. Seris, G. Abramowitz, A. Johnston and B. Haynes, "Scaleable, microstructured plant for steam reforming of methane," *Chemical Engineering Journal,* vol. 135, pp. S9-S16, 2008.

[49] H. Ge, A. J. Furlong, S. Champagne, R. W. Hughes, J. B. Haelssig and A. Macchi, "Modelling and Design of a Novel Integrated Heat Exchange Reactor for Oxy-Fuel Combustion Flue Gas Deoxygenation," *Energies,* vol. 17, no. 6, 2024.

[50] Endress+Hauser, "Proline Promass A 100," Endress+Hauser, [Online]. Available: https://www.ca.endress.com/en/field-instruments-overview/flow-measurement-product-overview/coriolis-flowmeter-promass-a100-8a1b?t.tabId=product-overview. [Accessed 30 10 2024].

[51] Yokogawa, "EJA510E In-Line Mount Absolute Pressure Transmitter," Yokogawa, [Online]. Available: https://www.yokogawa.com/ca/solutions/products-and-services/measurement/field-instruments-products/pressure-transmitters/absolute-pressure/eja510e/. [Accessed 30 10 2024].

[52] R. Winterton, "Where did the Dittus and Boelter equation come from?," *International Journal of Heat and Mass Transfer,* vol. 41, pp. 809-810, 1998.

[53] SALOME, "SALOME Version 9.10.0," SALOME, [Online]. Available: https://www.salome-platform.org/?p=2446. [Accessed 30 10 2024].

[54] A. E. Alain, H. Ge, S. Champagne, J. Haelssig, A. Macchi and R. W. Hughes, "Modelling of an intensified heat exchange reactor for flue gas polishing in a 600 kWth pressurized chemical looping pilot plant," in *7th International Conference on Chemical Looping*, Banff, Aberta, Canada, 2024.

[55] T. E. Marlin, Process Control: Designing Processes and Control Systems for Dynamic Performance, McGraw-Hill, 2015.

[56] Natural Resources Canada, "Energy Innovation Program - Carbon capture, utilization and storage RD&D Call," [Online]. Available: https://natural-resources.canada.ca/funding-partnerships/ccus-rdd-call.. [Accessed 28 April 2025].

[57] A. J. Furlong, N. K. Bond, M. J. Pegg and R. W. Hughes, "Evaluation of dust and gas explosion potential in chemical looping processes," *Journal of Loss Prevention in the Process Industries,* vol. 89, no. 105277, 2024.

[58] IPCS INCHEM, "Methane," Feburary 2000. [Online]. Available: https://www.inchem.org/documents/icsc/icsc/eics0291.htm. [Accessed 28 April 2025].

[59] L. He, Y. Fan, J. Bellettre, J. Yue and L. Luo, "A review on catalytic methane combustion at low temperatures: Catalysts, mechanisms, reaction conditions and

reactor designs," *Renewable and Sustainable Energy Reviews,* vol. 119, no. 109589, 2020.

[60] J. E. Hesselgreaves, R. Law and D. A. Reay, Compact Heat Exchangers: Selection, Design and Operation, Cambridge, MA, US: Butterworth-Heinemann, 2017.

[61] R. Le Pierres, D. Southall and S. Osborne, "Impact of Mechanical Design Issues on Printed Circuit Heat Exchangers," in *Proceedings of SCO2 Power Cycle Symposium*, Boulder, CO, 2011.

[62] NIST, "Material Properties: 316 Stainless," [Online]. Available: https://trc.nist.gov/cryogenics/materials/316Stainless/316Stainless_rev.htm. [Accessed 20 August 2025].

[63] Y. A. Cengel and A. J. Ghajar, Heat and Mass Transfer, New York, NY, US: McGraw-Hill Education, 2015.

7. Appendix A: Dynamic modelling of cross-flow printed circuit heat exchangers for multistage reactor intercooling [1]

Abstract

A reduced-order dynamic model of a cross-flow printed circuit heat exchanger was developed to study both steady-state and transient performance under conditions that would be encountered in multistage catalytic combustion reactors to better understand how they can be used to minimize fluctuations in heat-integrated reactors and intensified processes. Previous transient models for cross-flow heat exchangers rely on an initial steady state and apply only for changes in inlet temperature, but this work presents a model that can be applied to intermediate states or multiple concurrent upstream process changes. Steady-state simulations showed that larger channels reduce volumetric heat transfer performance and effectiveness due to convective resistance. Furthermore, larger channel spacing increases effectiveness but also reduces compactness. Operating temperature was found to have a minimal effect on the overall heat transfer coefficient and effectiveness within the range of conditions studied, and operating pressure was found to have no effect on heat transfer. Transient analyses showed that the response to a unit step in temperature matches closely with an analytical infinite gas velocity model, both for time constants and the overall thermal response, with initial variations in outlet temperatures from ideal-case models below 3.8 % of unit step magnitudes, and average differences below 0.75 %. Transient analyses also show the effects of a finite fluid velocity which is critical in the transient response of large heat exchangers. The presented numerical model can also be more easily extended to complex configurations and can be applied to other changes in

1 This chapter has been published in Applied Thermal Engineering: Furlong, A.J.; Ge, H.; Hughes, R.W.; Haelssig, J.B.; Macchi, A.
https://doi.org/10.1016/j.applthermaleng.2023.122010

inlet conditions such as changing composition and flow rates as are found in combustion applications. A three-fluid thermal management system for a multistage packed-bed microreactor using printed circuit heat exchangers is proposed and modelled to provide a method for temperature regulation and pre-heating of fresh reactor feed.

7.1. Introduction

Printed circuit heat exchangers (PCHEs), with an example of a straight-channel cross-flow configuration shown in Figure 7-1, are increasingly being used for process intensification because they provide efficient heat transfer in a compact and robust design. Their compactness and suitability for operation at elevated temperatures and pressures makes PCHEs ideal for use in supercritical fluid cycles and power cycles [1]. PCHEs can be operated in cross, co-current, or counter-current flow patterns, incorporating a small cross-flow section for process connections [2]. Cross- and counter-current flow patterns are also known to have a very high effectiveness with small channel sizes [3]. PCHEs are adjustable to process demands and can have a variety of channel shapes such as straight, wavy, zigzag, or airfoil patterns, each of which is best suited to reduce pressure drop or maximize heat transfer for a given application [4].

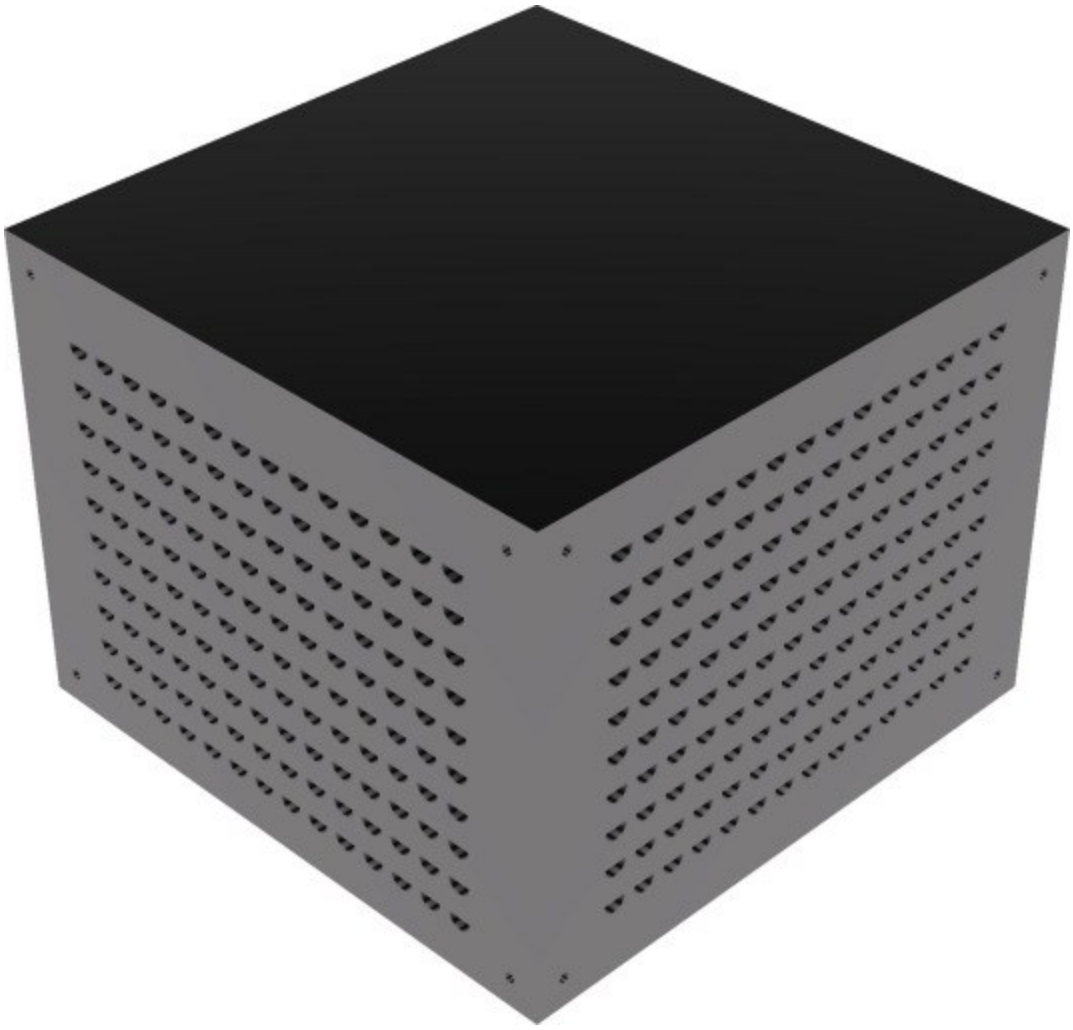

Figure 7-1: Rendering of a cross-flow PCHE showing alternating layers of semi-circular channels.

PCHEs can be directly used for heterogeneous catalytic reactions with the reaction occurring in-channel on a catalytic channel coating [5]. Alternatively, the PCHE assembly can be designed to incorporate alternating reaction beds and heat exchanger sections [6]. The use of a catalyst bed located between heat exchanger sections allows for simpler replacement of catalyst, removing the need to replace the entire unit when the catalyst degrades. The improved thermal management offered by PCHEs incorporated into reactors can also promote product selectivity and improve process safety [7]. Furthermore, multistage designs allow for the addition of new feed streams in each stage to manage

reaction rates, which can be incorporated into the exchanger design to reduce pre-heating requirements, improve safety, and decrease capital costs [8].

Many types of models have been used to study different configurations of PCHEs. For example, counter-current flow was modelled by Baik et al. [9,10] by reducing a pair of channels into a small number of volumes axially and assessing the heat transfer between adjacent volumes. Cross-flow PCHEs have been numerically modelled using several approaches. Yoon et al. [11] and da Silva et al. [12] employed iterative approaches using the NTU for PCHE designs to determine the effectiveness through which outlet temperatures can be determined. This effectiveness-NTU approach used in these works only applies for steady-state conditions. Zhao et al. [13] applied a unit cell-based approach like that of Baik et al. [9,10] for cross-flow with averaged fluid properties based on overall heat transfer coefficients in unit cells, but this approach does not consider the mass of the solid phase and thus can not be used for transient analysis. Kim et al. [3] further examined these unit cells using computational fluid dynamics (CFD) for laminar flow and focused on the conduction of heat through the solid phase to evaluate the overall heat transfer at steady state. The works of Kim et al. [3] and Jeon et al. [14] examined the heat transfer per unit volume and heat exchanger effectiveness with unit cells and demonstrated the impact of design parameters on performance. These models provide a rigorous foundation for modelling cross-flow PCHEs, but none of the models can be used for transient simulations because they do not consider the thermal inertia of the solid phase.

The transient response of a PCHE operating under counter-current conditions was modelled by Marchionni et al. [15] by discretizing the exchanger axially into a small number of volumes for a pair of channels and applying periodic boundaries. This model

was calibrated with manufacturer data and validated with a three-dimensional CFD model. More recently, start-up, shutdown, and a ramp-up have been investigated for counter-current flow [16]. Theologou et al. [17] proposed that a similar approach could be taken to model the transient response of a PCHE in a cross-flow pattern by creating a grid of simplified control volumes at the intersection of fluid channels with the transient modelling tool ATHLET. Evaluation of PCHE performance through such reduced-order grids has recently been shown to offer a significant reduction in computational time [18]. Idealized models have been developed for transient analysis of cross-flow heat exchanger performance, depending on constant properties, fluid velocities, flow distributions, and heat transfer coefficients. Mishra et al. [19] provided a numeric model which uses generalized correlations and a simplified form of the heat equation to predict the performance of cross-flow heat exchangers in response to disturbances in temperature and flow with fixed fluid properties and a dimensionless time, but in PCHEs constant fluid properties may not be applicable. Another model has been described by Spiga and Spiga [20] to examine the effects of changes in inlet temperature which uses an infinite gas velocity assumption and constant heat transfer and property assumptions. Understanding the transient response of PCHEs is valuable given their application to power cycles and microreactors, in addition to their significant thermal inertia. However, according to Chen et al. [21] the transient response of PCHEs has only been examined in a limited capacity, and only under co-current/counter-current conditions.

In this study, a reduced-order dynamic model was developed for two types of cross-flow PCHEs: one conventional geometry exchanging heat between one process stream and one utility stream, and one less common configuration to enable heat exchange between two

process streams and one utility stream. The reduced-order model was developed using a unit cell approach to ensure that simulations can be performed for a wide range of design and operability studies at a reasonable computational cost. Important assumptions in the model were verified using three-dimensional CFD simulations and data from literature. Sensitivity studies were performed to investigate the impact of key geometric dimensions and operating conditions on steady-state PCHE performance. Dynamic simulations were performed to study the transient response of the PCHE, and validation of the transient response was completed through comparison to an idealized model. Since PCHEs are a key process intensification technology, robust models are required to optimize their design and develop new applications. This study contributes valuable information to the understanding of the transient behaviour of PCHEs and expands the tools available for PCHE design and operation, including new designs of heat-integrated microreactors.

7.2. Methodology

7.2.1. Heat exchanger geometry

Most PCHE structures have many evenly spaced channels with equal dimensions. Straight channels with a semi-circular shape minimize pressure drop, best fitting use in a multi-stage reactor [1], [4]. Zigzag channels improve heat transfer performance, especially for the laminar flow regime. However, their fabrication cost is increased, and they have a higher pressure drop [22], [23]. Other channels include S-shaped fins and airfoils, but these geometries tend to have a high fabrication cost and lower level of maturity. Given the intent to use the model for multistage fixed-bed reactors with high gas velocities, only straight channels were modelled in this study due to their minimized frictional effects. A simple one-pass cross-flow configuration was selected as it can be used for interstage thermal

management in reactors and can offer performance close to that of an exchanger operating in counter-current flow [3], [6].

The dimensions describing a one-pass cross-flow PCHE are the diameter of the channels d, the wall thickness s, the plate thickness Δy, and the number of channels for each fluid. The cross-sectional area for flow Acs is for a semi-circle with diameter d. These dimensions, with a small section of three channels, are illustrated in Figure 7-2. The channel diameter is adjusted to balance optimal heat transfer and pressure drop. Wall thickness and plate thickness must be selected to maximize heat transfer performance while also ensuring that the material is not stressed to failure and that there is not crossover due to material degradation, with design guidelines given by Le Pierres et al. [24]. The number of channels is selected to provide the necessary heat transfer area and governs the length of the opposing, perpendicularly-positioned channels when combined with the channel spacing. In this work, the base dimensions of the heat exchanger are a channel diameter of 1.5 mm, a wall thickness of 1.1 mm, and a plate thickness of 2.1 mm. This gives a hydraulic diameter dh of 0.917 mm and a channel spacing Δx and Δz of 2.6 mm, where Δx is the spacing in the direction of flow for the hot fluid and Δz is the spacing in the direction of flow for the cold fluid.

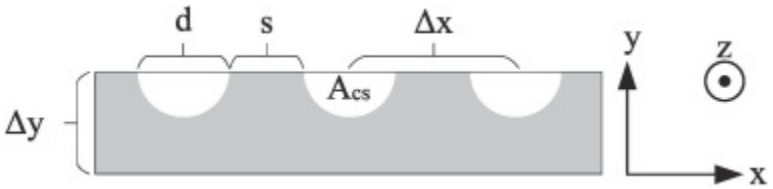

Figure 7-2: Printed circuit heat exchanger plate geometry for a sample of three channels, viewed from the heat exchanger header.

7.2.2. Model description

The velocity, temperature, and pressure profiles within the heat exchanger are governed by the conservation equations for mass, energy, and momentum. To reduce computational demand, the reduced-order model discretizes the PCHE into unit cells, consisting of two fluid volumes in cross-flow for the hot and cold fluids and two solid volumes, representing the repeated nature of the plates in the PCHE. Unit cells are bounded by the midpoint of the walls between channels, extended through both fluid plates. For a given heat exchanger with i hot fluid channels and j cold fluid channels, this provides a total of ij unit cells with 4ij total volumes.

The fluid and solid control volumes are shown with all heat transfer terms considered in Figure 7-3. A fluid volume is connected to both solid volumes in the unit cell through convection and to the adjacent fluid volumes in the same channel through advection, but axial conduction within the fluid is ignored as shown in Eq. 7.1:

$$\frac{\partial T_f}{\partial t} = u_x \frac{\partial T_f}{\partial x} + \frac{\dot{Q}_{conv}}{\rho_f V_f c_{p,f}} \tag{7.1}$$

where Tf is the temperature of the fluid, t is time, ux is the axial fluid velocity, Q̇conv is the total heat transfer by convection in an element, ρf is the fluid density, Vf is the fluid volume, and cp,f is the fluid specific heat capacity. Inlet mass flow rates, temperatures, and pressures are set as boundary conditions. Fluid properties are calculated based on local conditions within each unit cell but held constant for each time step.

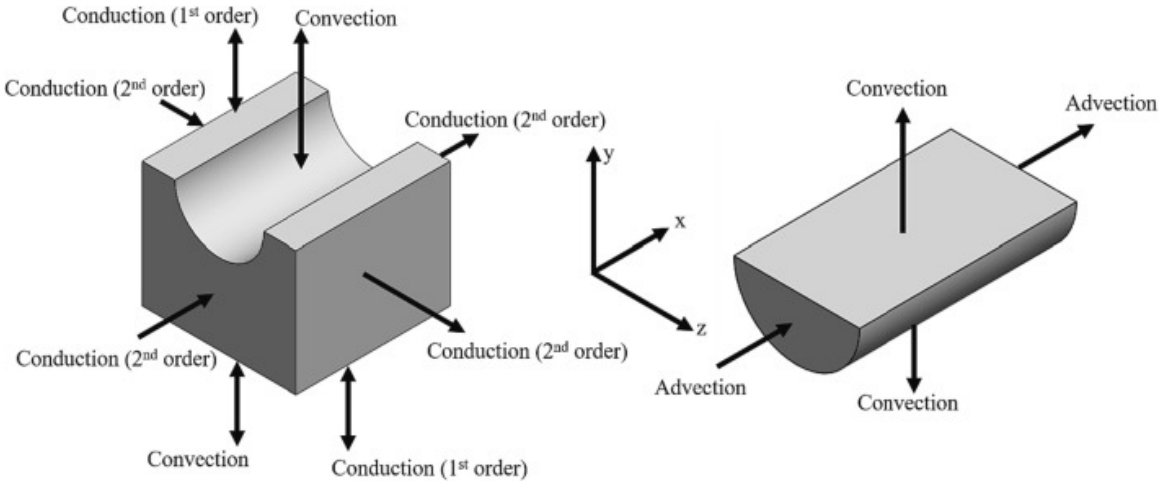

Figure 7-3: Solid (left) and fluid (right) control volumes with all heat transfer terms considered.

Conduction within solid volumes is modelled using the heat equation given in Eq. 7.2. Conduction between fluid plates was approximated using a first-order difference, and a shape factor S. Conduction perpendicular to flow neglects the resistance imparted by the fluid channel due to its minimal area.

$$\frac{\partial T_s}{\partial t} = \frac{1}{\rho_s c_{p,s}}\left(k_s\left(\frac{\partial^2 T_s}{\partial x^2} + \frac{\partial^2 T_s}{\partial z^2} + \frac{1}{S}\frac{\partial T_s}{\partial y}\right) + \frac{\dot{Q}_{conv}}{V_s}\right) \tag{7.2}$$

The solid phase was modelled as stainless steel and assumed to have a constant density ρs of 8000 kg m^{-3}, a temperature-dependent thermal conductivity k_s based on the data of Mills [25], and a temperature-dependent specific heat capacity $c_{p,s}$ based on Pichler et al. [26]. Properties should be selected specific to the materials of construction and the operating conditions of the heat exchanger. The temperature gradients used for lateral conduction were approximated using a second-order central difference scheme.

The pressure drop in the heat exchanger is assessed assuming incompressible flow by summing the pressure drop across each element:

$$\frac{dP}{dx} = \frac{2f\rho_F u_x^2}{d_h} \tag{7.3}$$

where f is the local Fanning friction factor.

The Fanning friction factor is required to calculate the pressure drop and a convective heat transfer coefficient is required to estimate the convective heat transfer rate. Many correlations have been developed for friction factors and heat transfer in microchannels. Muzychka and Yovanovich [27], [28] produced correlations for laminar flow in the entry region of non-circular ducts. Kim and NO [29] used an experimental approach and CFD studies to examine laminar flow characteristics of zigzag microchannels as are often used in PCHEs, showing a strong agreement between the experimental and numerical work. Berbish et al. [30] developed correlations from experimental data for turbulent flow in straight semi-circular channels, but these correlations embedded and focused on entrance effects for the specific experimental setup. Arslan [31] evaluated friction factors and Nusselt numbers in straight semi-circular channels as a function of position using CFD, fitting curves of the form $f = aRe^b$ and $Nu = cRe^d$, where *b* and *d* were kept consistent with the work of Berbish et al. [30]. Arslan's [31] work includes entrance effects in the overall correlation although to a lesser extent, being averaged across the length of the channel using equal spacing rather than weighted on the entrance. Generalized correlations for turbulent flow, such as those developed by Gnielinski [32], have been employed by groups investigating transient PCHE operation [15], [17].

Considering that there is only partial agreement in the literature, the Fanning friction factor is evaluated with the Petukhov correlation [33] for turbulent flow when Re > 2300:

$$f = \frac{1}{4}\left(0.79\, ln\left(Re_{d_h}\right)\right)^{-2} \tag{7.4}$$

The Nusselt number, which is used to evaluate the convective heat transfer coefficient *h*, is calculated using the correlation of Gnielinski [32]:

$$Nu_{d_h} = \frac{(f/2)(Re_{d_h} - 1000)Pr}{1 + 12.7\left(\frac{f}{2}\right)^{\frac{1}{2}}\left(Pr^{\frac{2}{3}} - 1\right)} = \frac{hd_h}{k_f} \tag{7.5}$$

Gnielinski's correlation is intended for use when Re > 3000, but to provide a broad range of modelling conditions it was assumed to apply for transitional flow cases where Re > 2300 with the poorly defined transitional flow regime. None of the cases examined in this work operated in the transitional flow regime 2300 < Re < 3000. Convective heat transfer rate $\dot{Q}_{conv}$ is evaluated using Eq. 7.6, with heat transfer areas given by Eq. 7.7 for a flat surface r and Eq. 7.8 for a curved surface c. Temperature differences are determined based on the bulk fluid temperature in a control volume and the bulk solid temperature in the adjacent solid control volume.

$$\dot{Q}_{conv} = h\left[A_{hx,r}\left(T_f - T_{s,r}\right) + A_{hx,c}\left(T_f - T_{s,c}\right)\right] \tag{7.6}$$

$$A_{hx,r} = d\Delta x \tag{7.7}$$

$$A_{hx,c} = \frac{\pi d}{2}\Delta x \tag{7.8}$$

Fluid density was calculated using the ideal gas equation of state. Specific heat capacities were calculated by polynomial regression using data from GRI 3.0 [34]. The viscosity of the gases was determined with the semi-empirical model given by Wilke [35] for a multi-component mixture with pure-species viscosity evaluated through CHEMKIN procedures

[36] using data from GRI 3.0 [34]. The thermal conductivity of the gases was evaluated using the model developed by Warnatz [37] for polyatomic gases.

For each unit cell, a periodic boundary was applied in the y-direction to model the repeated structure of the heat exchanger. The walls between unit cells were treated as conductive and an insulated boundary was applied at the edges of each plate. Fluid inlet temperatures, mass flow rates, and pressures were supplied for the cold inlet and hot inlet boundary conditions. These boundary conditions are illustrated in Figure 7-4. The integrated heat exchanger discretized into multiple unit cells with conduction, convection, and advection considered is shown in Figure 7-5.

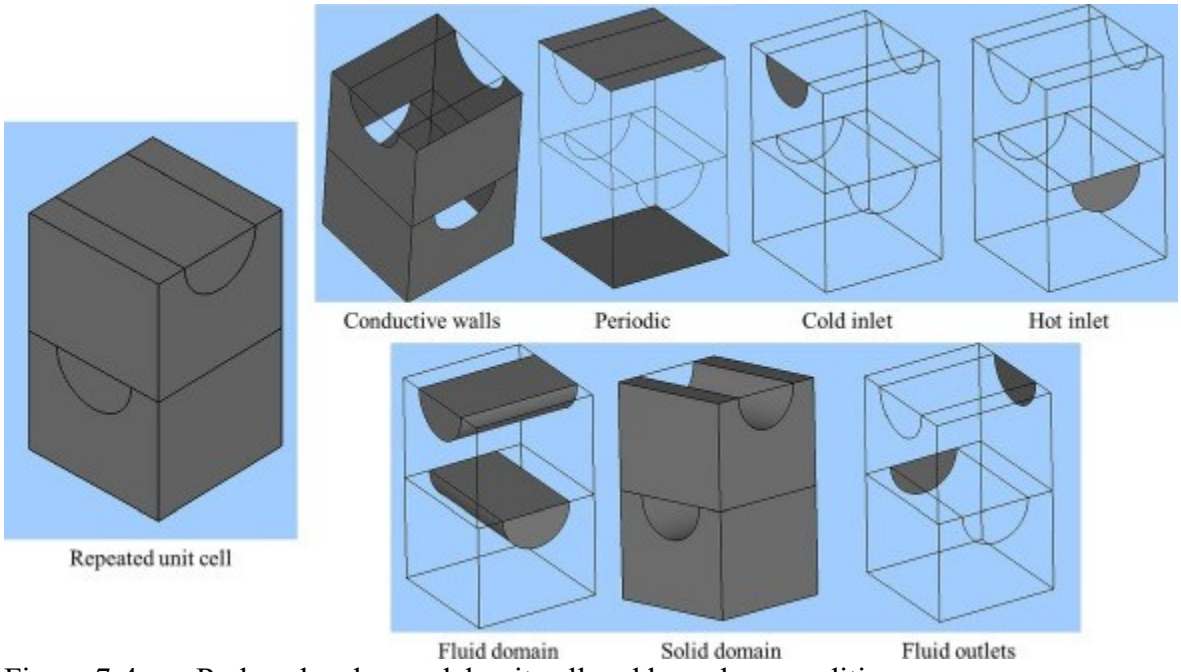

Figure 7-4: Reduced-order model unit cell and boundary conditions.

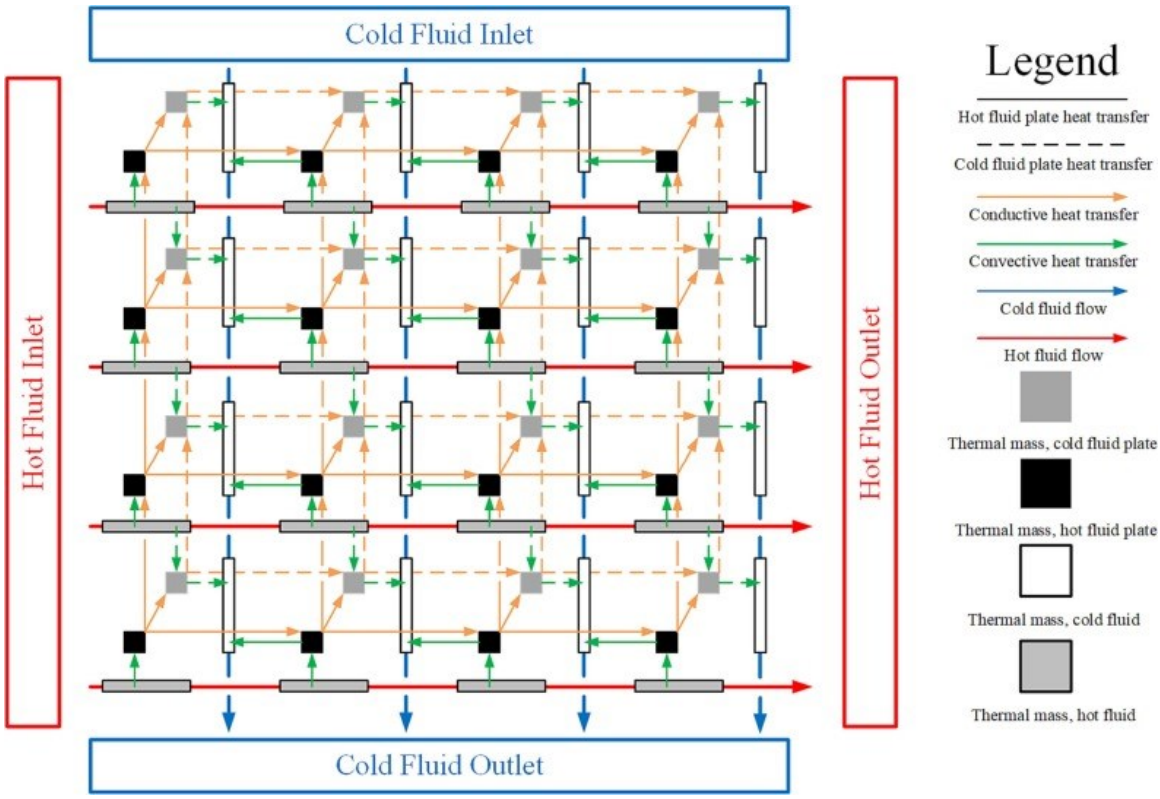

Figure 7-5: Visual representation of the unit cell approach used to discretize the governing equations. The illustration shows discretization into a 4 × 4 system of unit cells.

7.2.3. Numerical implementation

The reduced-order model was implemented as a system of ordinary differential equations for the transient temperature response of the fluid and solid domains in the heat exchanger and solved with a backward-differentiation formula implicit initial value solver. An initial temperature profile is required; however, a uniform profile can be applied, and the model can be integrated to an initial steady state. At every time point, the fluid properties and correlations were updated and used to assess the net heat transfer in each control volume. Net heat transfer rate was used to assess the transient temperature profile of the exchanger under isobaric conditions, and at the end time the pressure profile was updated. Using the updated pressure profile, the thermal profile is reassessed, and the process is repeated until the target differential pressure tolerance is met. Updates to boundary conditions are applied

at predetermined times to model changes in upstream process conditions. The implemented solution algorithm is summarized in Figure 7-6.

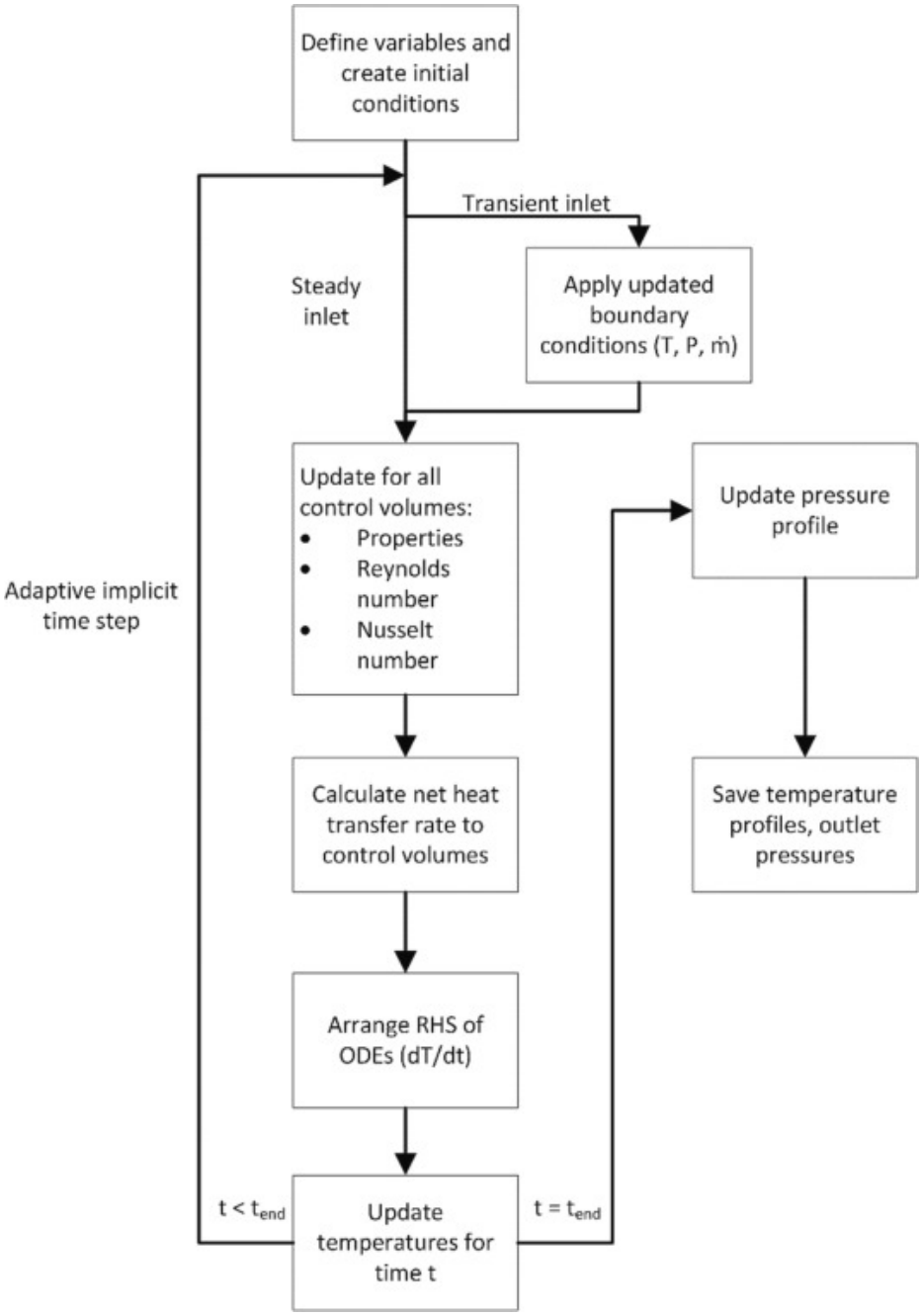

Figure 7-6: Algorithm flow chart for the implemented reduced-order model.

7.2.4. Summary of sensitivity studies

The base heat exchanger model uses the dimensions given in Table 1 with 25 channels for hot fluid and 40 channels for cold fluid, giving effective channel lengths L of 104 mm and 65 mm. Plate thickness was held constant at 2.1 mm. The impact of the channel diameter was examined by increasing the diameter of the channels by 50 % to 2.25 mm while retaining the channel spacing, giving effective channel lengths of 134 mm for the hot fluid and 83.75 mm for the cold fluid (case 2). The impact of channel spacing was examined by increasing the spacing by 50 % compared to the base case to 1.65 mm, giving channel lengths of 126 mm for the hot fluid and 78.75 mm for the cold fluid (case 3). Two additional cases were examined to understand the impact of temperature (case 4) and pressure (case 5) on exchanger performance with the base case geometry. In all cases, the cold fluid inlet temperature is 800 K at a pressure of 10 bar and mass flux of 558.9 kg m−2 s−1, giving a Reynolds number of 15,000. Additionally, the mass flux of the hot fluid was adjusted to maintain a Reynolds number of 15,000. These conditions were selected to model conditions present in the flue gas catalytic deoxidation stage following oxy-fuel combustion [38] and are summarized in Table 7-1. Both fluids were modelled as 100 % CO_2 for this study. Outlet temperatures are treated as the arithmetic mean of the temperatures at the end of each channel, assuming flow is evenly distributed between channels.

Table 7-1: Summary of investigated operating conditions and geometries. All cases have 25 channels for hot fluid and 40 channels for cold fluid. The cold fluid inlet temperature is 800 K at an inlet pressure of 10 bar and a mass flux of 558.9 kg m−2 s−1. In case 6 the mass flux for the cold fluid is varied. Deviations from base case are bold-faced.

Case number	**Case**	**Geometry**		**Hot fluid inlet temperature (K)**	**Hot fluid inlet pressure (bar)**	**Hot fluid mass flux (kg $m^{-2}s^{-1}$)**	**Time considered**
		Channel diameter *d* (mm)	Channel spacing *s* (mm)				
1	Base case	1.5	1.1	900	15	610.5	Steady-state
2	Large channels	2.25	1.1	900	15	406.7	Steady-state
3	Increased spacing	1.5	1.65	900	15	610.5	Steady-state
4	Impact of temperature	1.5	1.1	950	15	610.5	Steady-state
5	Impact of pressure	1.5	1.1	900	25	610.5	Steady-state
6a	Step change in temperature (warm-up)	1.5	1.1	800 (initial) 900 ($t \geq 0$ s)	15	610.5	Transient, 25 s total
6b						814.0	
6c						1221	
7	Temperature ramp	1.5	1.1	900 ($t < 0$ s) 900 + 2 t (0 s $\leq t \leq$ 25 s) 950 ($t >$ 25 s)	15	610.5	Transient, 50 s total
8a	Step change in mass flow	1.5	1.1	900	15	610.5 ($t < 0$ s) 671.6 ($t \geq 0$ s)	Transient, 25 s total

Case number	Case	Geometry		Hot fluid inlet temperature (K)	Hot fluid inlet pressure (bar)	Hot fluid mass flux (kg $m^{-2}s^{-1}$)	Time considered
		Channel diameter *d* (mm)	Channel spacing *s* (mm)				
8b						610.5 ($t < 0$ s) 814.0 ($t \geq 0$ s)	
8c						610.5 ($t < 0$ s) 1221 ($t \geq 0$ s)	

To understand the transient response of the heat exchanger, three transient cases were simulated. The first of these cases (case 6) shows the warm-up time from an initial temperature of T = 800 K with a step increase in fluid temperature to T = 900 K for the hot fluid. An initial temperature of 800 K was selected for both fluids to model the step from pre-heating using an external heating source before switching to a process fluid. This case was examined with Reynolds numbers of 15,000 (case 6a), 20,000 (case 6b), and 30,000 (case 6c) for both fluids to understand the impact of convective heat transfer coefficients on the time constant of the heat exchanger. The second transient case (case 7) shows the response of the system to a ramp in temperature, modelling a shift in upstream process operation for the hot fluid from T = 900 K to T = 950 K at a rate of 2 K s^{-1} with a constant mass flow rate. The third case examines the response of the unit to a step change in mass flux of hot fluid from 610.5 kg m^{-2} $s^{-1}$to 671.6 kg m^{-2} s^{-1} (case 8a), 814.0 kg m^{-2} s^{-1} (case 8b), and 1221 kg m^{-2} s^{-1} (case 8c; Reynolds numbers 15,000 stepped to 16,500, 20,000, and 30,000).

7.3. Model verification

7.3.1. Friction factor

As noted in the previous section, several correlations exist to estimate the friction factor in small channels. To investigate the correlation used for the friction factor for fully-developed flow in a semi-circular channel, the pressure drop along a semi-circular channel with a diameter of 1.5 mm and a length of 65 mm was evaluated using CFD with the mesh shown in Figure 7-7. The coarse mesh had 201,600 cells, the medium mesh had 777,600 cells, and the fine mesh had 3,110,400 cells, each with 300 cells axially with a focus on the entry region. The steady-state solution was computed using the simpleFoam solver in

OpenFOAM [39] and the k-ω SST model [40] with a second-order accurate, upwind-weighted discretization scheme for Reynolds numbers of 1938, 4845, 9689, 14,534, and 19,378. This gives average velocities of 10, 25, 50, 75, and 100 m s^{-1} with CO_2 as the process fluid and examines conditions from laminar flow to turbulent flow with a high maximum gas velocity for heat transfer while maintaining the Mach number Ma less than 0.3 at elevated temperatures. The k-ω SST model was selected for its near-wall performance with low y+ values, as were present in the simulations, and for its capacity to provide reasonable predictions under laminar flow conditions.

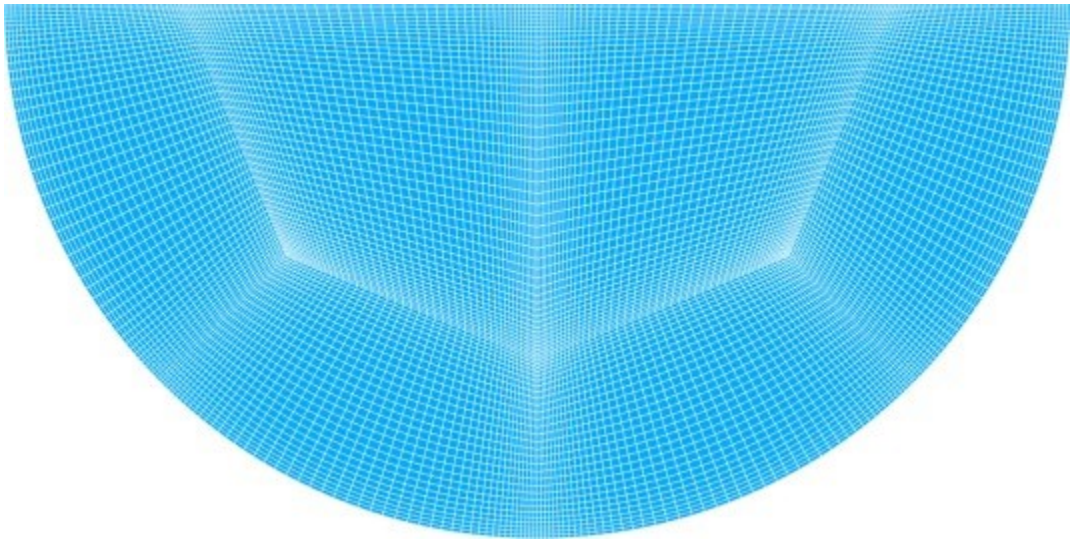

Figure 7-7: Cross-section of the fine mesh used for the friction factor studies showing the focus on near-wall behaviour and corner effects.

The results of the simulations for fully-developed flow are presented in Figure 7-8. They show that the fine mesh results were required to obtain a stable and accurate solution and that the predictions agree well with the correlation produced by Arslan [31] for a k-ω SST model developed for Reynolds numbers beyond 10,000. However, the Petukhov correlation [33] was selected for use in the reduced-order model because it satisfactorily provides reasonable predictions over a broad range of Reynolds numbers. Entry effects

were not considered in this study for turbulent flow since the work of Berbish et al. [30] shows that the turbulent flow entry region is approximately 15 pipe diameters in semicircular channels for the range of Reynolds numbers investigated. This corresponds to 13–21 % of the channel length used in the base case geometries. The results of this modelling exercise also show that a very fine mesh is required to accurately evaluate the frictional effects of semi-circular channels and that CFD results agree relatively well with established correlations for friction factor in smooth tubes.

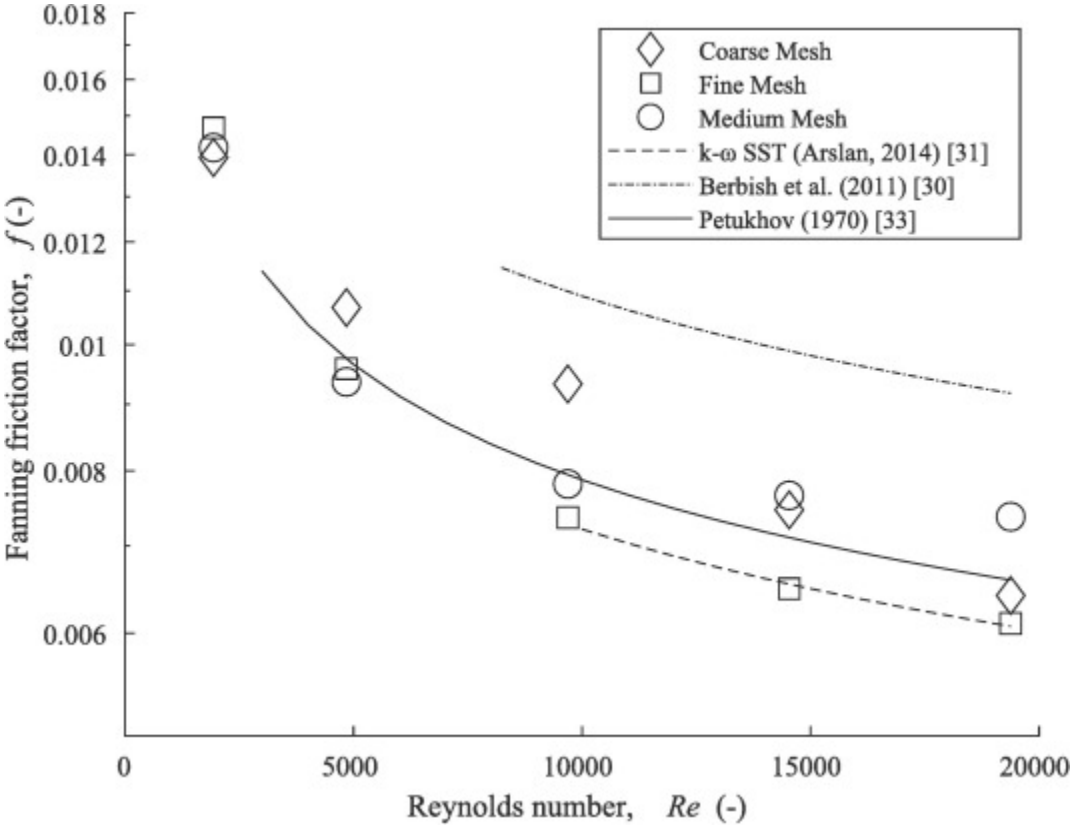

Figure 7-8: Comparison of friction factor predictions with correlations for semi-circular channels.

7.3.2. Convective heat transfer

Convective heat transfer was evaluated using the correlations of Berbish et al. [30], Arslan [31], and Gnielinski using Petukhov's correlation [32], [33], using an idealized constant value of Pr = 0.7 for gases. The correlation produced by Berbish et al. [30] averages the

Nusselt number across both the entrance and fully-developed regions. Data from the work of Berbish et al. [30] was extracted and re-fit for fully-developed flow alone. Figure 7-9 shows that the Gnielinski [32] correlation and the data collected by Berbish et al. [30] for fully-developed flow fall in the middle of the range between numerical work and experimental work. However, the Gnielinski [32] correlation was selected as it extends across a broader range of Reynolds numbers making it more suitable for the lower flow rates seen in many PCHE applications. The correlation can be also extended to a minimum Reynolds number of 2300 to account for transitional flow, which is poorly defined, but analysis was not conducted in the transition regime in this work. The variability in the Nusselt number with these correlations shows the relative impact of entrance regions and surface roughness; modelling of a specific unit should use generated experimental data when possible.

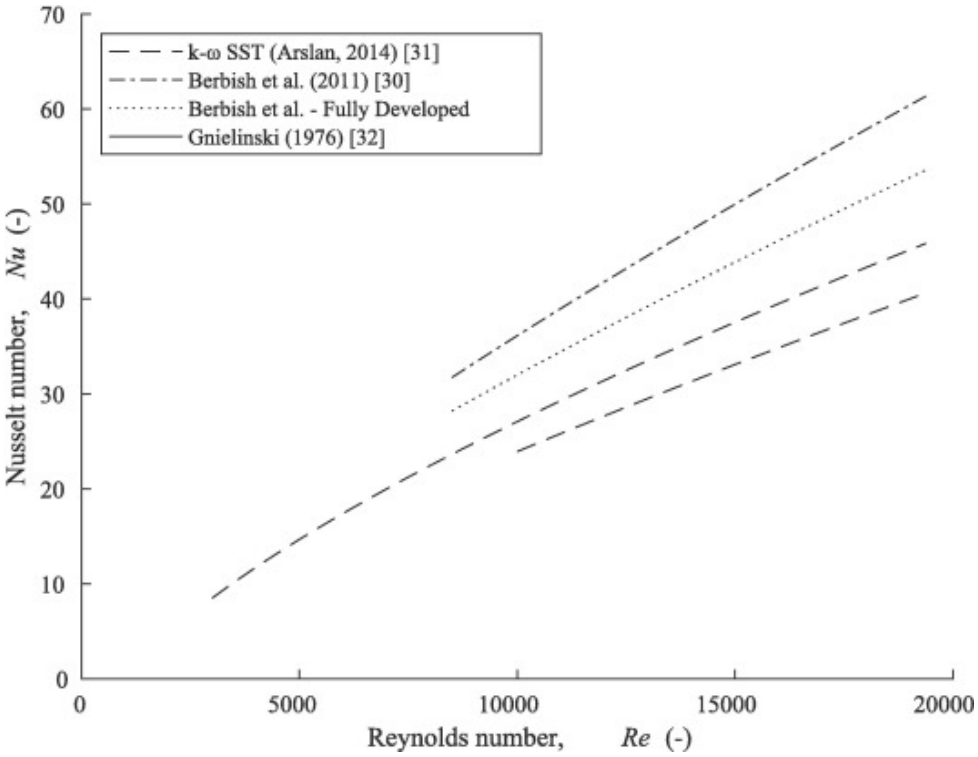

Figure 7-9: Comparison of Nusselt number correlations for flow in semi-circular channels with Pr = 0.7.

7.3.3. Multidimensional conduction effects

The multidimensional effects of the channels on heat conduction in the solid plates has previously been evaluated by Kim et al. [3] for both co-current and cross-flow configurations of PCHEs as a function of geometric parameters. The approach of Kim et al. [3] uses fluid volumes centered in solid volumes, whereas the present work uses the contact of each fluid with two solid elements. For the geometry used in the present study, extending the Kim et al. [3] correlation yields a conductive heat transfer rate through a plate between the hot and cold side channels (y-direction in Figure 7-2) that is 88 % compared to a constant area assumption. Given this minor change and that the Kim et al. model [3] is not directly suitable for the geometry used in this work, the constant area assumption was retained.

For heat conduction within a plate perpendicular to the direction of fluid flow (x-direction in Figure 7-2), a constant area assumption was also employed. For the geometry primarily investigated in this study and as per Figure 7-3, the fluid channels have a depth of 35.7 % of the plate thickness. However, with the semi-circular channel shape, the impact of the channels for conductive heat transfer is expected to be significantly reduced and was thus neglected in the model. For heat conduction within a plate parallel to the direction of fluid flow (z-direction in Figure 7-2), there are no channels impacting heat transfer. Of course, these one-dimensional approximations would become less accurate as surface temperature changes across control volumes become larger.

7.4. Results and discussion

7.4.1. Impact of geometry on steady-state performance

Increasing the diameter of the channels and thus their length from the cross-flow pattern resulted in a decrease in the overall heat transfer coefficient, a significant decrease of 20.5 % in heat transfer per unit volume, and a decreased effectiveness, which are reported in Table 7-2. This effect is due to the increase in resistance to heat transfer by convection. Previously, Kim et al. [3] have shown that the increase in resistance to convection can increase by more than a factor of two under such a change with fixed aspect ratios, but with the laminar flow conditions in that work the results are not directly comparable with fixed unit cell sizes. Kim et al. [3] also report a notable decrease in effectiveness under such a change, as was observed here. However, there was an overall increase in heat transfer rate due to the 50 % greater mass flow rates and 57 % increase in heat transfer area. Additionally, there was a significant reduction in pressure drop through the heat exchanger from 0.66 bar to 0.25 bar, despite the increase in mass flow rate and channel length. This demonstrates the value of design parameters on performance, allowing channel dimensions to be modified to meet heat transfer and/or pressure loss demands. In case 3, the increase in the spacing between channels led to an increase in overall heat transfer due to an increase in heat transfer area from the channel length, but the exchanger became significantly less compact. In this case, a 21 % increase in heat transfer area resulted in a 27 % increase in heat exchanger volume. Additionally, the increase in the overall channel lengths resulted in an increase in the pressure drop through the heat exchanger, making it less optimal for compact systems or reactor integration. These two cases demonstrate the desire for small channels with minimized spacing, but these considerations must be carefully weighed depending on the application and acceptable material stress limits.

Table 7-2: Summary of results for steady-state cases. Case numbers refer to the cases given in Table 7-1.

Case number	Case	Outlet temperature (K)		Hot fluid outlet pressure (bar)	Total heat transfer (W)	LMTD (K)	LMTD correction factor (-) [41]	Overall heat transfer coefficient, hot fluid ($W\ m^{-2}\ K^{-1}$)	Heat transfer per volume ($MW\ m^{-3}$)	Effectiveness (-)
		Hot fluid	Cold fluid							
1	Base case	856.1	830.5	14.34	707.3	54.6	0.96	1345	24.9	0.44
2	Larger channels (50 % increase in *d*)	861.4	826.8	14.75	933.4	61.6	0.95	822.6	19.8	0.39
3	Increased spacing (50 % increase in *s*)	840.2	835.2	14.20	817.7	43.7	0.94	1637	19.6	0.51
4	Impact of temperature (50 K increase in hot fluid inlet temperature)	884.3	846.0	14.30	1070.4	81.8	0.97	1345	37.7	0.44
5	Impact of pressure (10 bar increase in hot fluid inlet pressure)	856.1	830.5	24.61	707.3	54.6	0.96	1345	24.9	0.44

7.4.2. Impact of operating conditions on steady-state performance

Comparing the results of cases 1 and 4 in Table 7-2 shows that the performance of the heat exchanger is minimally affected for a constant Reynolds number with a change in temperature. This study found that the overall heat transfer coefficient had a minimal change between cases, owing only to the increase in the thermal conductivities with the rise in temperature. Additionally, the 50 % increase in the difference in inlet temperatures resulted in a 51.4 % difference in effective mean temperature difference and 49.7 % increase in volumetric heat transfer, showing that operating temperature does not significantly impact performance within the range of conditions studied external to the LMTD. However, this increase in temperature did result in a 6.1 % increase in pressure drop through the exchanger due to the increased viscosity and velocity of the gas.

Cases 1 and 5 show that the only impact on the performance of the heat exchanger at a constant Reynolds number with a change in pressure is that an increase in inlet pressure results in a lower pressure drop through the exchanger due to the reduced gas velocity. In this case, differences in the thermal performance of the heat exchanger were negligible, with identical overall heat transfer coefficients and volumetric heat transfer rate.

7.4.3. Transient response

The transient response of the heat exchanger to a 100 K step change in the inlet temperature of the hot fluid is shown in Figure 7-10. These results indicate time constants τ, presented in Table 7-3, close to those expected by $\tau_{theoretical} = m_s c_{p,s}/(hA)$ when evaluated at the final conditions. The zero capacitance (ZC) model for heat exchangers in cross-flow subject to a step change in temperature given by Ataer et al. [42] shows poor agreement in the evaluation of the time constant of the heat exchanger. However, it does demonstrate the

relationship between the fluid space time and the time constant, with a higher velocity yielding a shorter time constant. Other models, such as that of Boot et al. [43] are not suitable at high Reynolds numbers and provide results similar to the Ataer et al. ZC model [42]. The model developed by Spiga and Spiga [20] and further expanded by Romie [44], [45] for the infinite fluid velocity case using averaged fluid properties and conditions in the final case are in excellent agreement with the predicted transient response, both in the initial step response seen in the outlet of the stepped fluid and in the longer transient response. This agreement is especially good given the large magnitude of the step which provides a more significant instant change in fluid properties than a small step in a real system, with the error in the initial response being less than 4 % of the total step when evaluated using the final state heat transfer coefficient and properties. When modelled here with a finite gas velocity, the initial step in outlet temperature takes place at the time $t = L/u$ showing that the model is applicable beyond the infinite velocity case. The infinite velocity model, however, can not be as easily applied to cyclic or non-ideal changes in temperature such as decaying exponential changes, as they depend on an initial steady state, nor do they apply to a change in mass flow rate or composition. The model presented here can have boundary condition changes occur while in an unsteady state, as we show in case 7, with a transition from a ramp inlet temperature to constant inlet temperature. Knowledge of the heat transfer coefficient, time constant, overall performance, and approximations of functions are also required for Spiga and Spiga's model [20] with Romie's additions [44], making it less suitable for development of systems than the work presented here.

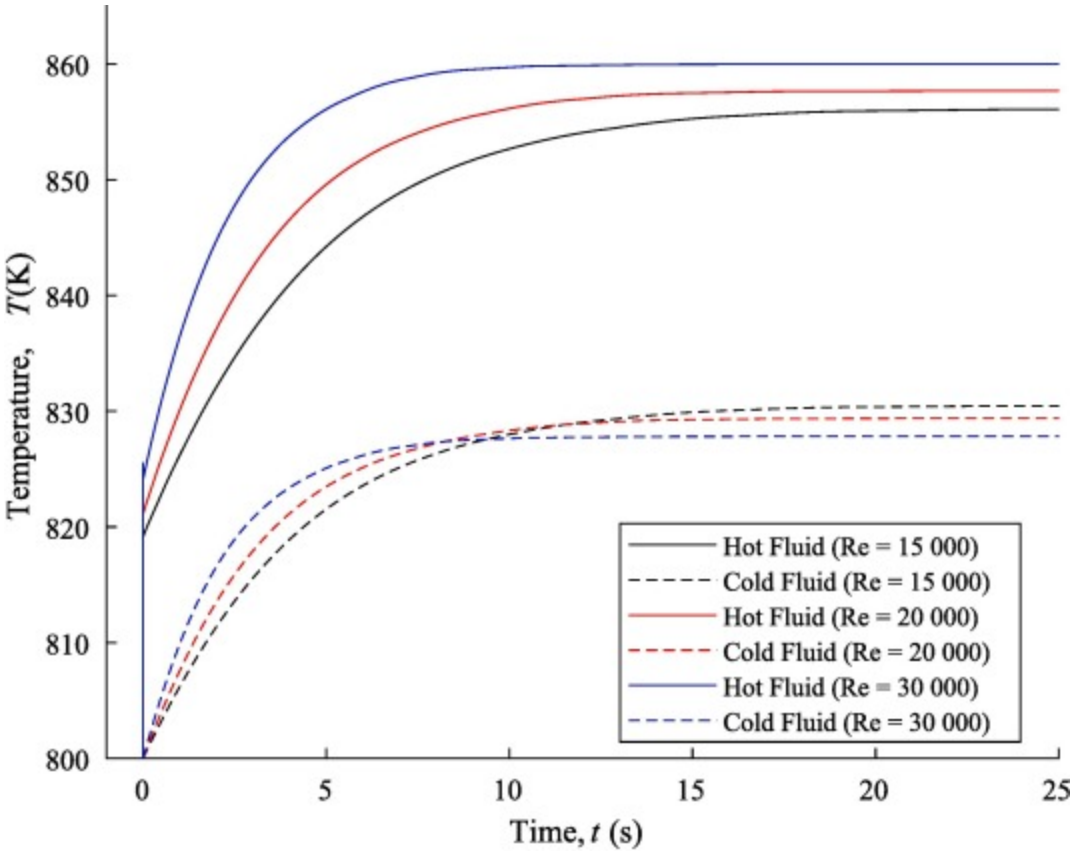

Figure 7-10: Transient response of fluid outlet temperatures of a PCHE to a 100 K step increase in hot fluid inlet temperature; case 6 in Table 7-1.

Table 7-3: Effective first-order time constants τ and initial response in hot fluid outlet temperatures for the transient cases evaluated in this study. Case numbers refer to the cases given in Table 7-1.

Case	τ_{hot} (s)		τ_{cold} (s)	$\tau_{theoretic}$ (s)	Magnitude of initial response, hot fluid (K)		Average absolute error, model vs. infinite velocity model (K)	
	ZC	Model	Model		Model	Infinite velocity	Hot fluid	Cold fluid
6a	2.60	4.44	4.12	4.06	19.19	22.96	0.50	0.40
6b	2.05	3.39	3.18	3.18	21.08	20.44	0.25	0.75
6c	1.35	2.32	2.20	2.20	25.50	23.36	0.27	0.45
7	2.61	2.58	4.40	4.06	–	–	–	–
8a	2.43	4.91	4.92	3.81	0.34	–	–	–
8b	2.07	3.56	3.47	3.27	1.19	–	–	–
8c	1.46	2.83	2.73	2.38	3.05	–	–	–

The transient response of the heat exchanger to a ramp in temperature demonstrates the expected ramp response with a scale factor, as is shown in Figure 7-11. This ramped response, r(t), is given by the following expression:

$$r(t) = K\tau\left(t - \tau + \tau\, exp\left(-\frac{t}{\tau}\right)\right) \tag{7.9}$$

where K is a scaling parameter and τ is the time constant of the response. At the end of the ramp the process returns to the response expected from a unit increase before rapid stabilization. In this case, the model of Spiga and Spiga [20] is suitable, however that of Romie [44] is not. The model of Spiga and Spiga [20] still depends on the use of constant properties and heat transfer coefficients which may not be applicable in all cases, such as if the temperature significantly varies in the system and affects heat capacities and viscosities. The time constant of the unramped fluid is also comparable to the theoretical time constant of the system, further supporting the validity of this modelling approach.

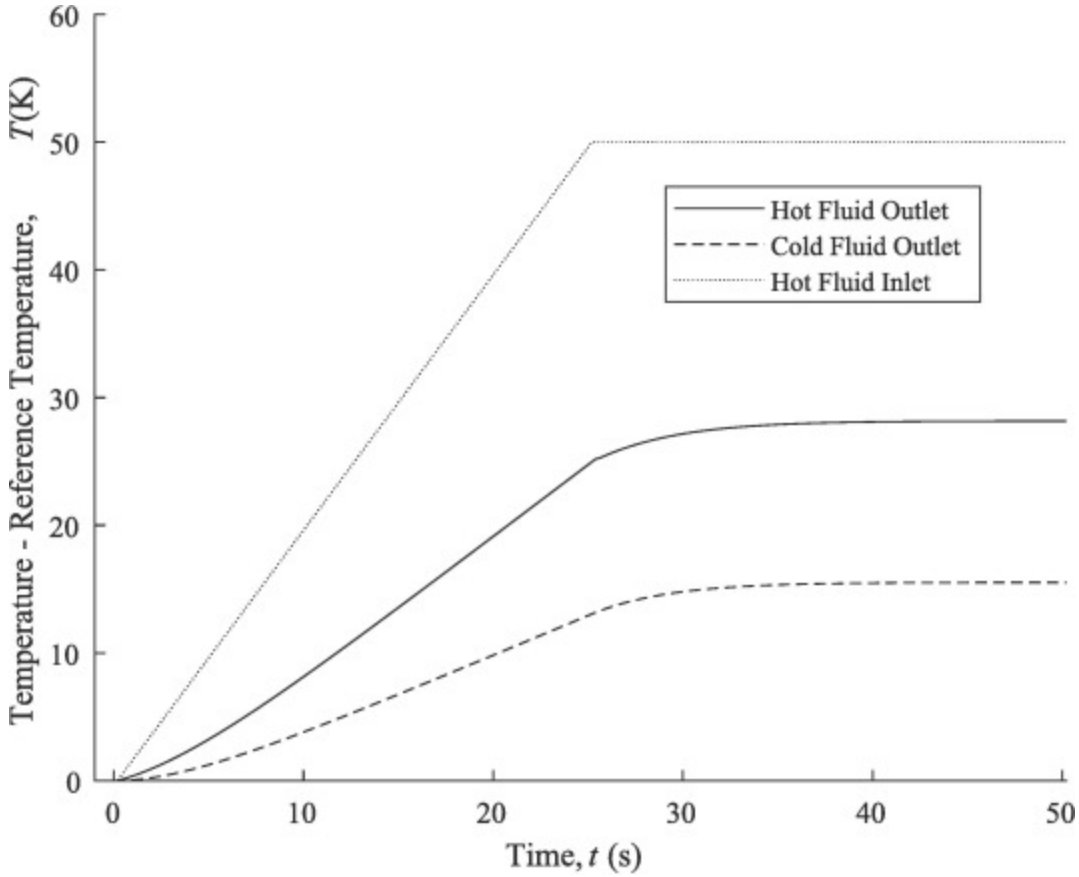

Figure 7-11: Response of a PCHE to a 2 K/s ramp in hot fluid inlet temperature (T_{ref} hot fluid outlet: 856.0 K; T_{ref} cold fluid outlet: 830.6 K; T_{ref} hot fluid inlet: 900 K); case 7 in Table 7-1.

In response to a step change in mass flow, the outlet temperatures shown in Figure 7-12 exhibit the same behaviour as for a step change in inlet temperature, but the time constants in each case were larger than expected from theory. These cases also exhibit an immediate step change in outlet temperature for the stepped fluid, but this can not be compared to the models from the other works referenced because they only apply in the case of a change in inlet temperature.

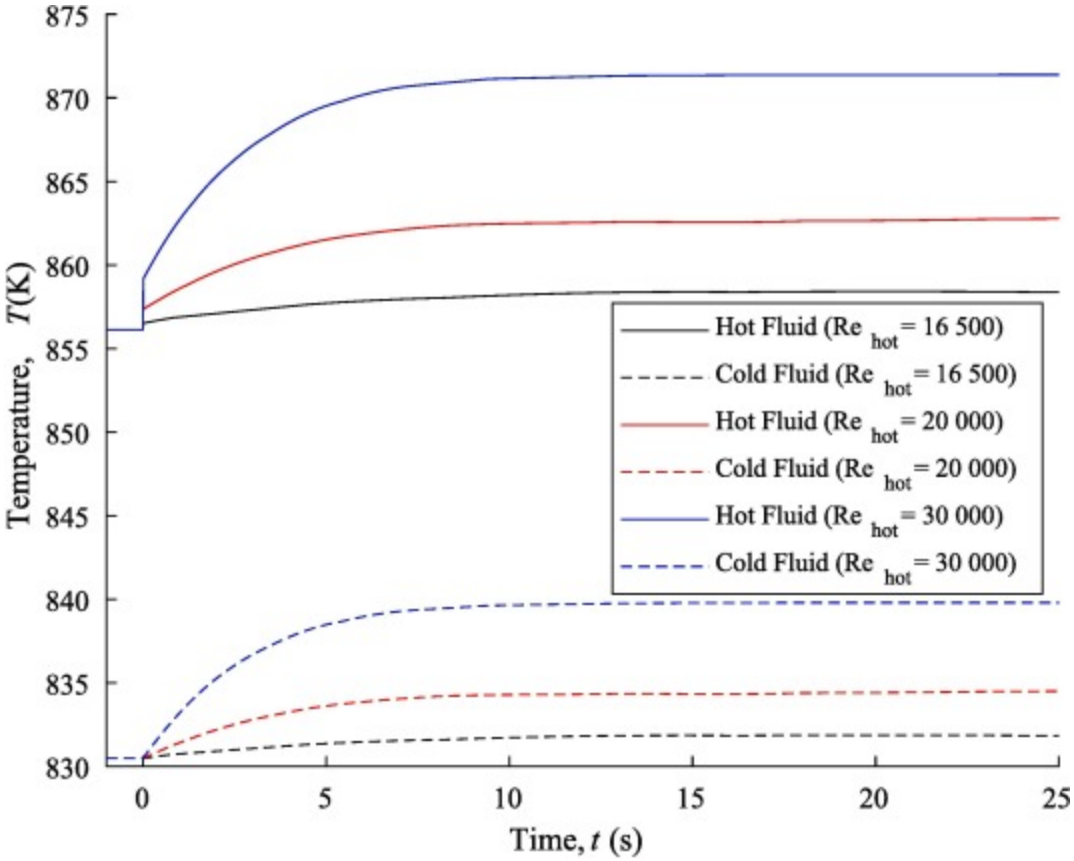

Figure 7-12: Transient response of a PCHE to step increases in mass flow for the hot fluid; case 8 in Table 7-1.

The results of this work demonstrate that the transient responses produced by the model fit well with the theoretical infinite velocity case; however, they can be extended to the non-infinite fluid velocity case and cases other than a step change in temperature. In reactive systems, variations in temperature may be accompanied by simultaneous changes in flow rate or composition, requiring adjustments to multiple boundary conditions concurrently, which can be performed by the numerical model proposed in this study.

7.4.4. Microreactor-integrated heat exchanger

To integrate a PCHE into a microreactor without feed pre-heating, the exchanger can be layered in a five-plate repeating unit between reactor sections [6], as shown in Figure 7-13. This structure uses the hot fluid stream to pre-heat additional reactants, while also offering

integrated thermal management. To model this system, the new reactant feed plate is treated as a duplicate of the hot fluid plates, placed between the two existing hot fluid plates. This design creates additional challenges in manifolding, but the new reactant stream can be preheated to be near the same temperature as the hot fluid between reaction stages, and it can even exceed the outlet temperature of the hot fluid depending on the cooling provided by the utility stream. In the y-direction, boundaries were modelled as periodic, while in the x/z directions boundaries were treated as insulated.

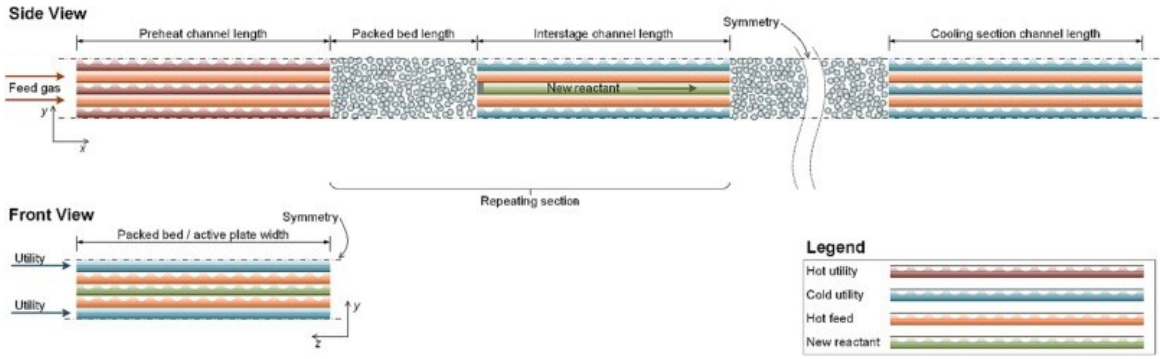

Figure 7-13: Five-plate PCHE structure incorporating feed pre-heating for interstage thermal management.

In this reactor-PCHE integrated system, the geometry investigated used a channel diameter of 1.5 mm, with spacing of 1.1 mm and plate thickness of 2.1 mm. 25 channels were used for the hot fluid and new reactant feed, with 40 channels for the cold fluid. The cold fluid was modelled as 100 % CO_2, with a temperature of 800 K, a pressure of 10 bar, and a mass flux of 558.9 kg m^{-2} s^{-1}. The hot fluid was modelled as 95 % CO_2 and 5 % O_2, at 900 K and 15 bar, with a mass flux of 610.5 kg m^{-2} s^{-1}. The new reactant feed was modelled as 100 % CH_4 at a temperature of 400 K and a pressure of 15 bar, with a mass flux of 6.1 kg m−2 s^{-1} (0.5 % of the total mass flow rate of the hot gas stream). The friction factors and Nusselt numbers for the new reactant feed (CH_4) were evaluated with the correlations of Muzychka and Yovanovich [27], [28] because they are valid in the developing region for

laminar flow as is applicable here. The microreactor-integrated heat exchanger was modelled as isobaric as the results in the previous sections demonstrated that the operating pressure of the heat exchanger does not impact performance significantly.

Results for the steady-state performance of the integrated system are summarized in Table 7-4. In the integrated system, there is a small difference in heat transfer across the new reactant feed plate due to the asymmetry of the plate geometry, where the facing of the hot fluid channels (seen in Figure 7-13) is the main contributor of this difference. There is effectively 57 % more heat transfer area between the lower-middle plate and bottom plate than between the top plate and upper-middle plate; however, the top and bottom plates are in contact in a repeated structure and provide an averaging effect. In the case examined here, the difference between the two reactant plates was only 1.9 W (0.20 %) of a total of 969.0 W.

Table 7-4: Summary of operating conditions and results for reactor-integrated PCHE.

Plate	**Mass flux (kg m^{-2} s^{-1})**	**Composition (mass %)**	**Temperature (K)**		**Net heat transfer (W)[1]**
			Inlet	**Outlet**	
Top (cold fluid)	558.9	CO_2: 100	800	819.5	451.5
Upper-middle (hot fluid)	610.5	CO_2: 95 O_2: 5	900	869.8	−485.5
Middle (new reactant feed)	6.1	CH_4: 100	400	871.4	87.4
Lower-middle (hot fluid)	610.5	CO_2: 95 O_2: 5	900	869.9	−483.5
Bottom (cold fluid)	558.9	CO_2: 100	800	819.2	444.1

[1] Net heat transfer in fluids is cyclic about 0 due to the reduced-order discretization.

7.5. Conclusions

This study developed and assessed a reduced-order model for the transient analysis of a printed circuit heat exchanger operating in cross-flow in response to deviations such as changes in fluid temperature and mass flow rate. This cross-flow pattern was modelled for two plates, and for a series of five plates to incorporate the PCHE into a microreactor. The model was developed using a unit cell approach, allowing for simulations to be carried out for a wide range of designs and conditions with a reasonable computational demand.

To validate the model, three-dimensional fluid flow studies were carried out and confirmed the suitability of the selection of friction factor for flow in straight semi-circular microchannels. Previous work from literature was analyzed to select models for the Nusselt number and the conduction through the system.

Sensitivity studies were carried out on the model of the heat exchanger and showed that the thermal performance of the PCHE in cross-flow is independent of the operating pressure of the heat exchanger. The fluid inlet temperature primarily changed the LMTD of the heat exchanger, allowing the use of an approximately constant overall heat transfer coefficient with different temperatures. An increase in the size of a channel results in a reduced heat transfer coefficient and a significant reduction in heat transfer per volume of the heat exchanger. Increasing the spacing between channels increases the overall heat transfer coefficient of the heat exchanger but significantly decreases the heat transfer per volume.

Transient analyses were completed to study the impact of a step change in temperature for the heat exchanger warm up period, a ramp increase in temperature, and a step increase in the mass flow rate through the exchanger. Time constants were approximately equal to

those expected from theory, and initial increases in temperature matched with an infinite velocity model. However, the results also demonstrated the effects of a finite velocity. Furthermore, the model presented in this work can be applied to variable boundary conditions such as changing mass flow rates, and it does not require an initial steady-state condition for modelling. Additionally, multiple varied boundary conditions, as are present in reactive systems, can be modelled. These analyses showed the significant thermal inertia of PCHEs and the need to consider transient analyses in design.

The model described in this work can be extended to a reactor-integrated system and used to model pre-heating of additional feed while managing the temperature of reactants between stages. The model shows a slight geometrical asymmetry between fluid plates due to the non-circular nature of the channels, but the overall effect is negligible.

References

[1] C. Huang, W. Cai, Y. Wang, Y. Liu, Q. Li, and B. Li, "Review on the characteristics of flow and heat transfer in printed circuit heat exchangers," Applied Thermal Engineering, vol.153, pp. 190-205, 2019.

[2] M. Pieve, "A Calculation method for the optimized thermal-fluid dynamic sizing of heat exchangers," Heat Transfer Engineering, vol. 29, pp. 556-564, 2008.

[3] W. Kim, Y.J. Baik, S. Jeon, D. Jeon, and C. Byon, "A mathematical correlation for predicting the thermal performance of cross, parallel, and counterflow PCHEs," International Journal of Heat and Mass Transfer, vol. 106, pp. 1294-1302, 2017.

[4] J.K. Cooper Heat Exchangers: Characteristics, Types and Emerging Applications, Hauppauge, NY: Nova Science Publishers, 2016

[5] Z. Anxionnaz, M. Cabassud, C. Gourdon, and P. Tochon, "Heat exchanger/reactors (HEX reactors): concepts, technologies: state-of-the-art," Chemical Engineering and Processing Process Intensification, vol. 47, pp. 2029-2050, 2008.

[6] B. S. Haynes and A. M. Johnston, "Process design and performance of a microstructured convective steam-methane reformer," Catal. Today, pp. 34-41, 2011.

[7] A. M. Johnston, W. Levy and S. O. Rumbold, "Application of Printed Circuit Heat Exchanger Technology within Heterogeneous Catalytic Reactors," in AIChE Annual Meeting, 2001

[8] E. Seris, G. Abramowitz, A. Johnston and B. Haynes, "Scaleable, microstructured plant for steam reforming of methane," Chemical Engineering Journal, vol. 135, pp. S9-S16, 2008.

[9] S. Baik, S.G. Kim, J. Lee, and J.I. Lee, "Validation of printed circuit heat exchanger design code KAIST_HXD, " in Transactions of the Korean Nuclear Society Spring Meeting, 2015

[10] S. Baik, S.G. Kim, J. Lee, and J.I. Lee, "Study on CO2 – water printed circuit heat exchanger performance operating under various CO_2 phases for S-CO_2 power cycle application," Applied Thermal Engineering, vol. 113, pp. 1536-1546, 2017.

[11] S.J. Yoon, P. Sabharwall, and E.S. Kim, "Numerical study on crossflow printed circuit heat exchanger for advanced small modular reactors," International Journal of Heat and Mass Transfer, vol. 70, pp. 250-263, 2014.

[12] R.P.P. da Silva, M.V.V. Mortean, K.V. de Paiva, L.E. Beckedorff, J.L.G. Oliveira, F.G. Brandão, A.S. Monteiro, C.S. Carvalho, H.R. Oliveira, D.G. Borges, and V.L. "Chastinet Thermal and hydrodynamic analysis of a compact heat exchanger produced by additive manufacturing," Applied Thermal Engineering, vol. 193, p. 116973, 2021.

[13] Z. Zhao, X. Chen, S. Li, S. Yang, and L. Huang, "Methodology of design and analysis on the thermal hydraulic performance of the cross-flow printed circuit heat exchanger," International Journal of Heat and Mass Transfer, vol. 156, Article 119756, 2020.

[14] S. Jeon, Y.J. Baik, C. Byon, and W. Kim, "Thermal performance of heterogeneous PCHE for supercritical CO2 energy cycle," International Journal of Heat and Mass Transfer, vol. 102, pp. 867-876, 2016.

[15] M. Marchionni, L. Chai, G. Bianchi, and S.A. Tassou, "Numerical modelling and transient analysis of a printed circuit heat exchanger used as recuperator for supercritical CO2 heat to power conversion systems," Applied Thermal Engineering, vol. 161, Article 114190, 2019.

[16] X. Sui, H. Russell, H. Gurgenci, S. Lee, Z. Guan, and P. Dong, "A one-dimensional modelling methodology of printed circuit heat exchangers for steady, off-design and transient feasibility in a supercritical CO2 power block," International Journal of Heat and Mass Transfer, vol. 193, Article 122938, 2022.

[17] K. Theologou, M. Hofer, R. Mertz, M. Buck, E. Laurien, and J. Starflinger, "Experimental investigation and modelling of steam-heated supercritical CO2 compact cross-flow heat exchangers," Applied Thermal Engineering, vol. 190, Article 116352, 2021.

[18] X. Li, D. Zhang, X. Li, W. Tian, S. Qiu, and G.H. Su, "Study on iterative algorithm of full plate cross-flow and counter-flow printed circuit heat exchanger for fluoride-salt-cooled high-temperature advanced reactor," International Journal of Advanced Nuclear Reactor Design Technology, vol. 5, pp. 86-96, 2023.

[19] M. Mishra, P.K. Das, and S. Sarangi, "Transient behaviour of crossflow heat exchangers due to perturbations in temperature and flow," International Journal of Heat and Mass Transfer, vol. 49, pp. 1083-1089, 2006.

[20] G. Spiga, and M. Spiga, "Two-dimensional transient solutions for crossflow heat exchangers with neither gas mixed," Journal of Heat Transfer, vol. 109, pp. 281-286, 1987.

[21] M. Chen, X. Sun, R.N. Christensen, I. Skavdahl, V. Utgikar, and P. Sabharwall, "Dynamic behavior of a high-temperature printed circuit heat exchanger: Numerical modeling and experimental investigation," Applied Thermal Engineering, vol. 135, pp. 246-256, 2018.

[22] M. Chen, X. Sun, R.N. Christensen, I. Skavdahl, V. Utgikar, and P. Sabharwall, "Pressure drop and heat transfer characteristics of a high-temperature printed circuit heat exchanger," Applied Thermal Engineering, vol. 108, pp. 1409-1417, 2016.

[23] G. Liu, Y. Huang, J. Wang, and R. Liu, "A review on the thermal-hydraulic performance and optimization of printed circuit heat exchangers for supercritical CO2 in advanced nuclear power systems," Renewable and Sustainable Energy Reviews, vol. 133, Article 110290, 2020.

[24] R. Le Pierres, D. Southall, and S. Osborne, "Impact of mechanical design issues on printed circuit heat exchangers," in: Proceedings of SCO2 Power Cycle Symposium 2011, Boulder, CO, 2011.

[25] K.C. Mills, "Recommended Values of Thermophysical Properties for Selected Commercial Alloys," Cambridge, UK: Woodhead Publishing Limited, 2002.

[26] P. Pichler, B.J. Simonds, J.W. Sowards, and G. Pottlacher, "Measurements of thermophysical properties of solid and liquid NIST SRM 316L stainless steel," Journal of Materials Science, vol. 55, pp. 4081-4093, 2020.

[27] Y.S. Muzychka, and M.M. Yovanovich, "Laminar forced convection heat transfer in the combined entry region of non-circular ducts," Journal of Heat Transfer, vol. 126, pp. 54-61, 2004.

[28] Y.S. Muzychka, and M.M. Yovanovich, "Pressure drop in laminar developing flow in noncircular ducts: a scaling and modeling approach," Journal of Fluids Engineering, vol. 131, 2009.

[29] I.H. Kim, and H.C. NO, "Thermal-hydraulic physical models for a Printed Circuit Heat Exchanger covering He, He-CO2 mixture, and water fluids using experimental data and CFD," Experimental Thermal and Fluid Science, vol. 48, pp. 213-221, 2013.

[30] N.S. Berbish, M. Moawed, M. Ammar, and R.I. Afifi, "Heat transfer and friction factor of turbulent flow through a horizontal semi-circular duct," Heat and Mass Transfer, vol. 47, pp. 377-384, 2011.

[31] K. Arslan, "Three-dimensional numerical investigation of turbulent flow and heat transfer inside a horizontal semi-circular cross-sectioned duct", Thermal Science, vol. 18, pp. 1145-1158, 2014.

[32] V. Gnielinski, "New equations for heat and mass transfer in turbulent pipe and channel flow," International Journal of Chemical Engineering, vol. 16, pp. 359-368, 1976.

[33] B.S. Petukhov, "Heat transfer and friction in turbulent pipe flow with variable physical properties," Advances in Heat Tranfer, vol. 6, pp. 503-564, 1970.

[34] G.P. Smith, D.M. Golden, M. Frenklach, N.W. Moriarty, B. Eiteneer, M. Goldenberg, C.T. Bowman, R.K. Hanson, S. Song, W.C. Gardiner Jr., V.V. Lissianski, and Z. Qin, "GRI-MECH 3.0," (n.d.). [online]. Available: http://combustion.berkeley.edu.proxy.bib.uottawa.ca/gri-mech/ [accessed October 31, 2020].

[35] C.R. Wilke, "A viscosity equation for gas mixtures," The Journal of Chemical Physics, vol. 18, no. 4, pp. 517-519, 1950.

[36] R.J. Kee, G. Dixon-Lewis, J. Warnatz, M.E. Coltrin, J.A. Miller, and H.K. Moffat, "A FORTRAN computer code package for the evaluation of has-phase, multicomponent transport properties [CHEMKIN]," 1998.

[37] J. Warnatz, Numerical Methods in Laminar Flame Propagation, Wiesbaden: Vieweg+Teubner Verlag, 1982.

[38] R.T. Symonds, R.W. Hughes, M.D. Las O. Loscertales, "Oxy-pressurized fluidized bed combustion: configuration and options analysis," Applied Energy, vol. 262, 2020.

[39] OpenFOAM Foundation, "OpenFOAM, " (n.d.), [Online]. Available: https://openfoam.org/ [accessed July 6, 2023].

[40] F.R. Menter, M. Kuntz, and R. Langtry, "Ten Years of Industrial Experience with the SST Turbulence Model," in Proceedings of the Fourth International Symposium on Turbulence, Heat and Mass Transfer, Begell House, Antalya, Turkey, pp. 625–632, 2003.

[41] T.L. Bergman, A.S. Lavine, F.P. Incropera, and D.P. DeWitt, Fundamentals of Heat and Mass Transferd, Hoboken, New Jersey: John Wiley & Sons, 2003.

[42] Ö.E. Ataer, A. Ileri, and Y. Göğüş, "Transient behaviour of finned-tube cross-flow heat exchangers" International Journal of Refrigeration, vol. 18, pp. 153-160, 1995.

[43] J.L. Boot, J.T. Pearson, and R.G. Leonard, "An improved dynamic response model for finned serpentine cross-flow heat exchangers," in ASHRAE Transactions, American Society of Heating, Refrigerating and Air-Conditioning Engineers Inc., pp. 218–239, 1977.

[44] F.E. Romie, Discussion: "Two-Dimensional Transient Solutions for Crossflow Heat Exchangers with Neither Gas Mixed" (Spiga, G., and Spiga, M., ASME Journal of Heat Transfer, vol. 109, pp. 281–286, 1987.) and "Transient Temperature Fields in Crossflow Heat Exchangers With Finite Wall Capacitance" (Spiga, M., and Spiga, G., ASME Journal of Heat Transfer, vol. 110, pp. 49-53, 1988.), Journal of Heat Transfer. Vol. 115, pp. 1082-1082, 1993.

[45] F.E. Romie, "Two functions used in the analysis of crossflow exchangers, regenerators, and related equipment," Journal of Heat Transfer, vol. 109, pp. 518-521, 1987.